Nanostructured Electrospun Fibers:
from Superhydrophobicity to Block Copolymer Self-assembly

by

Minglin Ma

Bachelor of Science in Chemical Engineering
Tsinghua University, Beijing China
(July, 2003)

SUBMITTED TO THE DEPARTMENT OF CHEMICAL ENGINEERING IN PARTIAL FULFILLMENT OF THE REQUIREMENTS FOR THE DEGREE OF

DOCTOR OF PHILOSOPHY

AT THE

MASSACHUSETTS INSTITIUTE OF TECHNOLOGY
(September, 2008)

Signature of Author_____
Minglin Ma
Department of Chemical Engineering
July 30, 2008

Certified by_____
Gregory C. Rutledge
Lammot du Pont Professor of Chemical Engineering
Department Executive Officer
Thesis Supervisor

Accepted by_____
William M. Deen
Carbon P. Dubbs Professor of Chemical Engineering
Chairman, Committee for Graduate Students

Nanostructured Electrospun Fibers:
from Superhydrophobicity to Block Copolymer Self-assembly

by

Minglin Ma

Submitted to the Department of Chemical Engineering on July 30, 2008 in Partial Fulfillment of the Requirements for the Degree of Doctor of Philosophy

Abstract

Electrospinning has emerged in recent years as a relatively easy, efficient and robust method to make ultrafine continuous fibers with diameter on the order of ~100 nm from a variety of materials. As a result, numerous applications for electrospun fibers have already been demonstrated including the commercialized ones in the areas of filtration and tissue engineering. However, in most cases, the nanofibers are homogeneous; the development of external and internal nanostructures could significantly expand the applications of these fibers. The goal of this dissertation is therefore to develop controllable nanostructures for electrospun fibers with an emphasis on the understanding of structure formation and explore their unique applications.

Specifically, this dissertation can be divided into two areas. The first part is related to superhydrophobic or "self-cleaning" surfaces. This has been a hot research area due to the wide applications of such materials. Electrospun fibers were first discovered in this dissertation to have sufficient surface roughness for superhydrophobic effect. In contrast to many conventional superhydrophobic surfaces, those composed of electrospun fibers are flexible, breathable and free-standing. It has been demonstrated that superhydrophobic fabrics can be made by either electrospinning a hydrophobic material or applying post-treatment to electrospun mats (e.g. through initiated chemical vapor deposition). Based on an understanding of the role of fibrous structure to create a surface of suitable topology, different strategies have been invented to enhance the superhydrophobic property and its robustness by carefully designing the external nanostructures of individual fibers using various methods such as layer-by-layer assembly. Other functionalities such as transparency and fluorescence were successfully incorporated into superhydrophobic surfaces. In particular, superhydrophobic fibrous membranes with structural colors as those displayed by some beautiful butterfly wings were produced.

Besides making superhydrophobic materials from the externally nanostructured fibers, internally nanostructured electrospun fibers were also developed through the microphase separation of cylindrically confined block copolymer systems. This is the

second part of this dissertation. Continuous nanofibers with long range order internal structure were obtained by two-fluid coaxial electrospinning in which the desired block copolymer is encapsulated as the core component within a polymer shell having a high glass transition temperature (Tg), followed by proper thermal annealing of the fibers. Various interesting, unusual and sometimes unprecedented self-assembly structures of block copolymers under cylindrical confinement have been observed. Based on quantitative analyses, the confinement was found to affect both phase type and fundamental domain sizes of the block copolymer. These internally nanostructured fibers have both practical and fundamental intellectual importance. For example, these nanofibers have unique potential for applications in optics, photonics, drug delivery, and other uses because of their small diameter, unique internal structure, and continuous filamentary nature.

Thesis Supervisor: Gregory C. Rutledge

Title: Lammot du Pont Professor and Executive Officer of Chemical Engineering

Acknowledgements

I find it hard to use such a limited space to express my thanks for the help, support and encouragement I received during the past 5 years at MIT. I am deeply indebted to a number of people without whom this 5-year long and sometimes tough time can not be so enjoyable for me.

The first person I want to thank is my advisor Prof. Gregory C. Rutledge. I feel extremely lucky to have had not only the guidance on my research from one of the best scientists at MIT, but also the help on my professional growth from a true mentor. The first time I talked to him was during advisor-selecting process. At that time, when I read his early papers on electrospinning, I was amazed on both the breadth and depth of those papers. His group started constructing operating diagrams and analyzing all kinds of instabilities occurring during electrospinning, while many others in this area still considered incorrectly the jet splitting instead of whipping to form fine fibers. Over the course of my Ph.D., I benefited a lot from such a high standard he puts on research. He is always enthusiastic and excited about new ideas and results, which motivates me tremendously. The first part of this thesis, superhydrophobic properties of electrospun materials, was actually not my thesis topic but an unexpected discovery at that time. Without the support, encouragement and the freedom he gave me, I would not have gone so far and published a number of papers in this area. There are many other examples, but in one word, I want to sincerely thank him for not only the success in my thesis but also the time I have been fully enjoying at MIT.

I owe a particular debt of gratitude to my committee members, Prof. Robert Cohen, Dr. Randal Hill, Prof. Anne Mayes and Prof. Edwin Thomas. All their comments and suggestions have helped me a lot. Especially, I was fortunate to have two papers with Prof. Cohen, three papers with Dr. Hill, all in the area of superhydrophobicity, and two papers with Prof. Thomas in the area of confined block copolymers. I still remember how valuable and critical their comments were in the process of publishing these papers. I want to thank Prof. Mayes in particular for her encouragement on the idea of encapsulating block copolymers using chemical vapor deposition. (Based on the same principle, I did the encapsulation by core-shell electrospinning later.)

Prof. Karen Gleason, although not in my committee, helped very much. I want to express my sincere thanks to her in particular for her expertise on chemical vapor deposition and numerous insightful comments during our collaborations. In addition, I thank Prof. Gareth McKinley and Prof. Michael Rubner for the collaborations.

I enjoyed several fruitful collaborations with many different students and postdocs. In particular, I want to thank Dr. Malancha Gupta and Dr. Jessie Mao for their kind help on chemical vapor deposition, Dr. Lei Zhai, Dr. Zhi Li and Dr. Xiaoxia Sheng for their expertise on layer-by-layer deposition, Dr. Vahik Krikorian for his help on cryo-microtomy at the beginning of the block copolymer project. In addition, I thank

Dr. Anish Tuteja for collaborating with me.

I appreciate all the interactions and friendship with my fellow group members: especially Mr. Kirill Titievsky, Dr. Jian Yu, Mr. Joseph Lowery, Dr. Jung Ah Lee, Dr. Sergey Fridrikh, Dr. Mao Wang, Dr. Pradipto Bhattacharjee, Ms. Chia-ling Pai, Mr. Yuxi Zhang who have been working side-by-side with me on related projects. In addition, I thank Dr. Alex Hsieh and all the staff in Institute for Soldier Nanotechnologies (ISN) for help during my research. My research is supported in part by the U.S. Army through the ISN, under Contract DAAD-19-02-D-0002 with the U.S. Army Research Office. The content does not necessarily reflect the position of the Government, and no official endorsement should be inferred.

I also want to thank many other people in particular those in the Church in Cambridge for their caring and support during these years. Because of this church life, Friday nights and Sunday mornings become the most joyful time not only for me but also for my family.

Last but certainly not least, I thank my parents, my parents-in-law and particularly my wife, Fang Zhou. Without her, this Ph.D. degree is impossible. I value a lot her caring, encouragement and support. I was moved deeply numerous times when I came back late from the lab and saw delicious dinner, already prepared and still warm, on the table, and when I realized she spent whole night taking care of our baby without waking me up. Fang, thank you.

Table of Contents

Abstract.....2

Acknowledgement.....4

Table of Contents.....6

List of Figures.....9

List of Tables.....15

Chapter 1 Introduction.....16

1.1 Background in Electrospinning and Electrospun fibers.....16

1.2 Thesis Overview.....19

PART I. SUPERHYDROPHOBIC PROPERTY OF ELECTROSPUN MATERIALS

Chapter 2 Introduction to Superhydrophobicity.....23

2.1 Wetting Phenomena, Contact Angles and Hysteresis.....23

2.2 Roughness-induced Superhydrophobicity.....24

2.3 Characterization of Superhydrophobic Surfaces.....28

Chapter 3 Experimental Methods.....30

3.1 Fabrication.....30

3.2 Characterization.....34

3.3 Chemicals.....36

Chapter 4 Making Superhydrophobic Mats by Electrospinning.....37

4.1 Electrospinning Hydrophobic Materials into Fibers.....37

4.2 Applying Hydrophobic Coating to Electrospun Fibers.....43

Chapter 5 The Effect of Fiber Morphology on Superhydrophobic Property of Electrospun Fiber Mats.....53

5.1 Experimental Results.....53

5.2 Modeling Results.....59

Chapter 6 Introducing Hierarchical Roughness to Electrospun Mat to Enhance the Robustness of Its Superhydrophobic Property.....65

6.1 Introduction 65
6.2 Introducing Nanopore Structures to Electrospun Fibers 67
6.3 Introducing Nanoparticles to Electrospun Fibers 72

Chapter 7 Conclusions and Recommendations 78
7.1 Conclusions 78
7.2 Recommendations for Future Work 79

PART II. BLOCK COPOLYMERS IN ELECTROSPUN FIBERS

Chapter 8 Introduction to Block Copolymers 84
8.1 Block Copolymers in Bulk 84
8.2 Block Copolymer Thin Films 87
8.3 Block Copolymers under Curved Confinement 89
8.4 Electrospinning of Block Copolymers 90

Chapter 9 Experimental Methods 93
9.1 Fabrication of Electrospun Block Copolymer Fibers 93
9.2 Block Copolymers, Solution Compositions and Operating Parameters 94
9.3 Characterization of Block Copolymer Fibers 96

Chapter 10 Block Copolymer Electrospun Fibers 99
10.1 Block Copolymer Fibers by Single-Fluid Electrospinning 99
10.2 Encapsulating Block Copolymers Using Co-axial Electrospinning 102

Chapter 11 Lamella-forming Block Copolymers under Cylindrical Confinement 106
11.1 PS-PI-PS Triblock Copolymer 106
11.2 PS-PDMS Diblock Copolymer 111
11.3 The Effect of Cylindrical Confinement on the Lamellar Domain Structure 114
11.4 Long Range Order of Concentric Lamellar Morphology 121

Chapter 12 Other Types of Block Copolymers under Cylindrical Confinement 125

12.1 Sphere-forming Block Copolymers 125
12.2 Cylinder-forming Block Copolymers 129
12.3 Gyroid-forming Block Copolymers 132

Chapter 13 Conclusions and Recommendations 141
13.1 Conclusions 141
13.2 Recommendations for Future Work 143

Appendix I Electrospun Mats Decorated with Functional Nanoparticles 148
AI.1 Antimicrobial Electrospun Mats 148
AI.2 Photo-catalytic Electrospun Mats 150

Appendix II Multifunctional Superhydrophobic Surfaces 153
AII.1 Superhydrophobic Surface with Anisotropic Property 153
AII.2 Superhydrophobic Surface with Structural Color 155
AII.3 Superhydrophobic Surfaces with Optical Functionalities 159

Notations and Abbreviations 164
References 166

List of Figures

Figure 1-1 Electrospinning setup and properties of electrospun materials.....19

Figure 1-2 A schematic overview of this dissertation.....21

Figure 2-1 Static, advancing and receding contact angles.....24

Figure 2-2 Water droplet on smooth and rough surfaces.....27

Figure 2-3 Droplet of different states on superhydrophobic surfaces.....29

Figure 3-1 Reaction mechanism for PPFEMA iCVD with tert-butyl peroxide as an initiator.....33

Figure 4-1 Superhydrophobic/superoleophilic property of electrospun PS fiber mats.....39

Figure 4-2 Superhydrophobic property of electrospun PS-PDMS/PS fiber mat..41

Figure 4-3 Tunable hydrophobic property of electrospun PMMA/fluoroPOSS fiber mats.....43

Figure 4-4 Superhydrophobic mat made by dip-coating method.....44

Figure 4-5 Molecular structure and hydrophobic property of PPFEMA.....45

Figure 4-6 Conformal iCVD and "beaded" iCVD.....47

Figure 4-7 Properties of conformal iCVD coating.....48

Figure 4-8 Superhydrophobic property of 70 nm PPFEMA coated electrospun fiber mats.....49

Figure 4-9 Repellent to water vapor and surfactant solution.....51

Figure 4-10 Repellent to oils (alkanes).....52

Figure 5-1 Typical SEM images of the PCL electrospun mats used for the study of fiber morphology effect.....55

Figure 5-2 The water contact angles for the as-spun PCL mats.....57

Figure 5-3 Contact angles for PPFEMA-coated PCL mats.....58

Figure 5-4 Threshold sliding angles for the PPFEMA-coated PCL mats.....59

Figure 5-5 Modeling of superhydrophobic property of electrospun fiber mats....62

Figure 5-6 Schematic representations of water droplet sitting on fibers. 64

Figure 5-7 A robust superhydrophobic mat requires both high intrinsic contact angle and high density of small fibers. 64

Figure 6-1 Schematic representations of water droplet sitting on smooth fibers and rough fibers, and corresponding robustness parameters.. 66

Figure 6-2 SEM images of fibers with nanopore structures made from different materials. 68

Figure 6-3 Electrospun mat with nanopore structure exhibiting enhanced superhydrophobic property. 70

Figure 6-4 SEM images of polymer/nanoparticles composite fibers and porous fibers made by removing the nanoparticles. 71

Figure 6-5 Comparison of surface structure of smooth and nanoparticle-decorated electrospun Nylon fibers. 74

Figure 6-6 Comparison of surface chemistry of as-spun Nylon fibers and treated fibers. 75

Figure 6-7 Electrospun mat decorated with nanoparticles exhibiting enhanced superhydrophobic property. 76

Figure 6-8 Another example of nanoparticle-decorated electrospun mat exhibiting enhanced superhydrophobic property. 77

Figure 7-1 SEM images of poly(*N*-isopropylacrylamide) electrospun fiber mat..81

Figure 8-1 A introduction to block copolymer in bulk. 85

Figure 8-2 Composition profiles for weakly segregated and strongly segregated block copolymers in bulk. 86

Figure 8-3 A Schematic illustration for different applications of block copolymers in nanotechnologies. 87

Figure 8-4 A schematic illustration for thin films of symmetric block copolymers

supported on one substrate or confined between two substrates. 88

Figure 9-1 Schematic for the two-fluid core-shell electrospinning spinneret by which block copolymer is encapsulated into core-shell fibers. 94

Figure 9-2 Characterization of electrospun block copolymer fibers: core-shell structures and block copolymer microphase separated structures. 97

Figure 10-1 PS-PDMS/PS electrospun fibers. 99

Figure 10-2 DSC curves for the microphase separated PS-PDMS/PS fibers. 100

Figure 10-3 Internal nanostructures of electrospun PS-PDMS/PS fibers. 101

Figure 10-4 Internal nanostructures of electrospun PS-PI fibers. 101

Figure 10-5 Advantages of co-axial electrospinning to make block copolymer fibers. 104

Figure 10-6 SEM images of annealed PMMA/V4111 core-shell fibers. 105

Figure 10-7 Cross sectional AFM images of the PMMA/V4111 core-shell fibers that have been annealed at 115 °C for 6 days. 105

Figure 11-1 A TEM image of the V4411 PS-PI-PS triblock copolymer in bulk. 106

Figure 11-2 Two-fluid co-axial electrospinning of the V4411 PS-PI-PS triblock copolymer. 107

Figure 11-3 TEM images of the V4411 PS-PI-PS core in the as-spun fibers showing the non-equilibrium microphase separation. 108

Figure 11-4 TEM images of the V4411 PS-PI-PS block copolymer in the fiber cores of different diameters after annealing, showing the concentric lamellar structure formed by the block copolymer. 111

Figure 11-5 A multi-scale view of an electrospun PS-PDMS-L1 block copolymer fiber mat. 113

Figure 11-6 Axial views of the concentric lamellar morphology formed by the PS-PDMS-L1 confined in electrospun fibers with different sizes. 114

Figure 11-7 Axial views of the concentric lamellar morphology formed by PS-PDMS-L1 with 4 bilayers.. 115

Figure 11-8 Axial views of the concentric lamellar morphology formed by PS-PDMS-L1 with 5 bilayers.. 116

Figure 11-9 Axial views of the concentric lamellar morphology formed by PS-PDMS-L1 with 6 bilayers. 116

Figure 11-10 The effect of cylindrical confinement on the domain size of lamellar morphology.. 117

Figure 11-11 Schematics for curved block copolymer interfaces..... 121

Figure 11-12 Longitudinal views of the concentric lamellar structure near dislocation point..... 123

Figure 11-13 Longitudinal TEM images of the PS-PDMS-L1 block copolymer confined in core-shell electrospun fibers with nearly uniform core diameters. 123

Figure 11-14 TEM images of PS-PDMS-L2 (L_0=42 nm) confined in electrospun fibers. 124

Figure 12-1 Co-axial electrospinning of the PS-PI-S1 block copolymer. 125

Figure 12-2 TEM images of the P(MMA-*r*-MAA)/PS-PI-S1 fibers. 126

Figure 12-3 TEM images of the PS-PI-S1 block copolymer in the cores of annealed fibers with relatively large diameters..... 127

Figure 12-4 TEM images of the PS-PI-S1 block copolymer in the cores of annealed fibers with relatively small diameters..... 128

Figure 12-5 TEM images of the PS-PI-S2 block copolymer in the cores of annealed fibers. 129

Figure 12-6 Co-axial electrospinning of the V4211 PS-PI-PS triblock copolymer. 130

Figure 12-7 TEM images of the V4211 cylinder-forming block copolymer confined in relatively large electrospun fibers..... 131

Figure 12-8 TEM images of the V4211 cylinder-forming block copolymer confined in relatively small electrospun fibers. 132

Figure 12-9 Co-axial electrospinning of the PS-PDMS-G1 block copolymer. .. 133

Figure 12-10 TEM images of the PMAA/PS-PDMS-G1 fibers. 134

Figure 12-11 TEM images of PS-PDMS-G1 thin film. 134

Figure 12-12 Cross-sectional TEM images of the PS-PDMS-G1 block copolymer under cylindrical confinement, showing the concentric lamellar morphology. 135

Figure 12-13 Cross-sectional TEM images of the PS-PDMS-G1 block copolymer confined in electrospun fibers, showing a structure schematically illustrated in the inset of (a). 137

Figure 12-14 Cross-sectional TEM images of the PS-PDMS-G1 block copolymer confined in electrospun fibers, showing a structure schematically illustrated in the inset of (a). 137

Figure 12-15 Cross-sectional TEM images of the PS-PDMS-G1 block copolymer confined in electrospun fibers, showing other unusual morphologies..... 138

12-16 Simulation results of a gyroid-forming block copolymer (A_4B_8) confined in cylindrical pores with different diameters and lengths. 138

Figure 12-17 Cross-sectional TEM images of the PS-PDMS-G2 block copolymer under cylindrical confinement, showing the concentric lamellar morphology (a-e) and the unusual morphologies (f-i).. 139

Figure 13-1 Cylindrically confined block copolymer/homo-polymer blend..... 144

Figure 13-2 Incorporating nanoparticles into block copolymer fibers. 145

Figure 13-3 TEM images of PEO electrospun fibers containing functionalized multi-wall carbon nanotubes..... 146

Figure AI-1 Antimicrobial property of Ag nanoparticle coated P(MMA-*r*-MAA) random copolymer fibers.. 150

Figure AI-2 Photo-catalytic property of TiO_2 nanoparticle coated electrospun fibers. 152

Figure AII-1 Anisotropic surface based on electrospun fibers..... 155

Figure AII-2 Superhydrophobic surface exhibiting structural color. 157

Figure AII-3 Electrospun fibers with different fiber sizes exhibiting different

colors.....158

Figure AII-4 Calculated scattering spectra based on normal illumination on an infinitely long cylinder.....159

Figure AII-5 Superhydrophobicity and transparency are two competing material properties.....160

Figure AII-6 A transparent superhydrophobic surface made by electrospraying and iCVD.....161

Figure AII-7 SEM images with different magnifications of PPE electrosprayed microparticles.....162

Figure AII-8 A fluorescent superhydrophobic surface made by electrospraying in one single step.....163

Figure AII-9 Enhancing mechanical integrity of the PPE particle surface by thermal annealing.....163

List of Tables

Table 5-1 Solution concentrations, operating parameters and average fiber diameter and bead size of PCL electrospun mats. Sample labels starting with "F" are bead-free fibers while those starting with "B" are beaded fibers.....54

Table 9-1 Different block copolymers used in this study.....95

Table 9-2 Solution concentrations and operating parameters for the single-fluid electrospinning of different block copolymers.....95

Table 9-3 Solution concentrations and operating parameters for the two-fluid electrospinning of different block copolymers.....96

Chapter 1 Introduction

1.1 Background in Electrospinning and Electrospun fibers

Electrospinning, as the name suggests, uses electrostatic forces to produce polymer fibers. Compared to the fibers made by other spinning methods, electrospun fibers have much smaller diameters, typically in the micrometer, sub-micrometer and nanometer (<100 nm) range. Electrospinning first appeared in the early 20th century,[1,2] and recently received tremendous attention from both industry and academia as a scientifically interesting process and a practically useful tool to make micro/nano fibers.[3] The process itself is similar to the better known electrospraying.[4] In electrospraying, a fluid drop at the orifice of the piping under the influence of the external electrical field first forms a cone known as the Taylor Cone[5] and then, as the electrical field increases, a jet shoots off from the tip of the cone and breaks into droplets as a result of the Rayleigh instability[6] driven by the surface tension. In electrospinning, the polymer fluid does not breakup into droplets but instead forms a slender, continuous liquid filament because of the suppression of the Rayleigh instability due to the viscoelastic property the jet. After emitting from the tip of the cone, the electrified liquid jet is accelerated downfield, thinning as it goes, and may encounter electrohydrodynamic instabilities[7,8] such as "whipping" that further stretches the liquid stream. Upon evaporation of solvent from the increased surface area of the stretched jet, solid fibers are collected at the counter-electrode. The balance between surface tension and repulsion among charges at the jet surface has been used to explain the ultimate diameter of the fibers.[9] In addition, bead-on string

morphologies may arise if the droplet breakup instability is not completely suppressed but arrested by strain hardening of the viscoelastic fluid as it drains from the jet to growing droplets.[10] Although the mechanism of the electrospinning is complicated, the experimental setup is extremely simple, as shown in Figure 1-1. It consists of basically a high voltage power supply, a polymeric fluid supply, one high potential electrode and one collector electrode.[11] Because of the ease of implementation in the laboratory scale, electrospinning has become a popular choice for making continuous micro/nano fibers. Using this technique, more than 100 different types of polymeric materials have been processed into fibers.[12] Due to their small fiber sizes, high surface area and fine pores structures, electrospun fiber mats have found various applications including micro/nanofibers-reinforced composites, ceramic fibers, filtration and protective clothing, scaffolds for tissue engineering, supports or carriers for drugs, enzymes and catalysts, materials for electronic and optical devices, sensing technology and sacrificial templates for 1D nanostructures. Electrospinning now has been scaled up industrially and some of the applications mentioned above for electrospun fibers have been commercialized. For example, the Nanospider™ developed by Elmarco Ltd. and Technical University of Liberec is one of the equipments that enable mass production of electrospun fibers. (http://www.elmarco.com). The Donaldson Company, Inc. (http://www.donaldson.com) and the Freudenberg Nonwovens Group (http://www.nonwovens-group.com/) are using electrospun fibers as high-quality filtering media.

Despite of the many applications mentioned above, electrospun fibers in most cases are homogeneous. The development of surface or internal nanostructures for electrospun fibers could significantly improve their properties and expand their applications. For example, fibers with surface pore structures have been made by using highly volatile solvents.[13] As will be demonstrated in this dissertation, these fibers as well as those decorated with nanoparticles have enhanced surface activities such as superhydrophobicity. Improved thermal and mechanical properties have been reported for aluminosilicate- and carbon nanotube-filled composite fibers, respectively.[14,15] Additional properties such as magnetic and reactive properties can also be incorporated into electrospun fibers by introducing functional nanoparticles.[16,17] Besides incorporating nano-fillers, the development of internal structures in electrospun fibers has also been achieved via crystallization of homopolymer,[18] macrophase separation of a polymer blend[19] during the drying and solidification of the fibers or post-spin treatment of the fibers.[20] As will be described in this dissertation, internal nanostructures with long range order can be developed for electrospun fibers by a combination of electrospinning and block copolymer self-assembly. Important potential applications of these internally structured fibers include phase selective chemistry, sustained drug release, photonic fibers and multifunctional textiles.

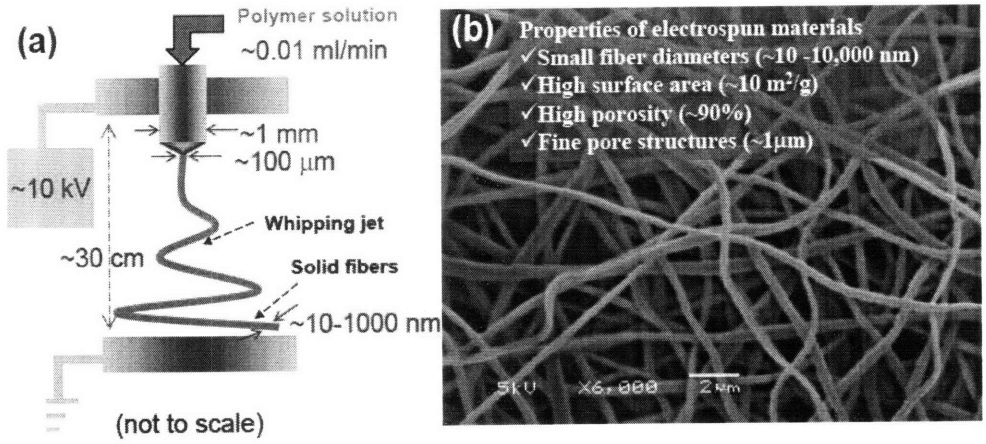

Figure 1-1 Electrospinning setup and properties of electrospun materials. (a) A schematic illustration of electrospinning setup with typical parameters and length scales labeled. (b) A microscopic view of a typical electrospun fiber mat. Some useful material properties are listed in the figure.

1.2 Thesis Overview

This dissertation describes the author's works in two major areas of research in nanostructured electrospun fibers: the first part of the dissertation which is on the superhydrophobic property of electrospun fibers deals with external nanostructures of these fibers, while the second part which describes the study on self-assembly of cylindrically confined block copolymers is related to internal nanostructures of the fibers.

Chapter 2 provides a short review on the fundamentals of wetting phenomena and superhydrophobic surfaces in general. Chapter 3 is a description of experimental methods to fabricate and characterize the superhydrophobic electrospun materials. Chapter 4 describes superhydrophobic properties of electrospun materials and different strategies to make them. The effect of fiber morphology on superhydrophobic behavior is explored and a theoretical model is presented to explain

the effect in Chapter 5. Chapter 6 introduces the concept of hierarchical structure for electrospun fibers. Based on this concept as well as the understanding developed in Chapter 5, electrospun fibers with surface nanostructures were made to enhance the superhydrophobic property and its robustness. Chapter 7 summarizes the first part of this dissertation and provides recommendations for the future work. The second part of this dissertation starts from Chapter 8. The motivation is presented in this chapter after an introduction to block copolymers in bulk and under confinement. Chapter 9 presents experimental methods including fabrication of block copolymer fibers and characterization of the internal nanostructures of these fibers. Chapter 10 describes the non-equilibrium structures in the block copolymer fibers and a novel strategy to get near equilibrium structures - encapsulating block copolymers in core-shell electrospun fibers. Chapter 11 is the study on the self-assembly of lamella-forming block copolymers under cylindrical confinement. Chapter 12 presents some preliminary data on sphere-forming, cylinder-forming and gyroid-forming block copolymers confined in electrospun fibers. This thesis ends in Chapter 13 which lists the main conclusions of the second part and a number of recommendations for future work on block copolymer fibers as well as nanostructured electrospun fibers in general. There are two appendices: one on functional nanoparticle coatings and the other one on multifunctional superhydrophobic surfaces made by electrospinning or electrospraying. The following figure (Figure 1-2) provides an overview of this dissertation.

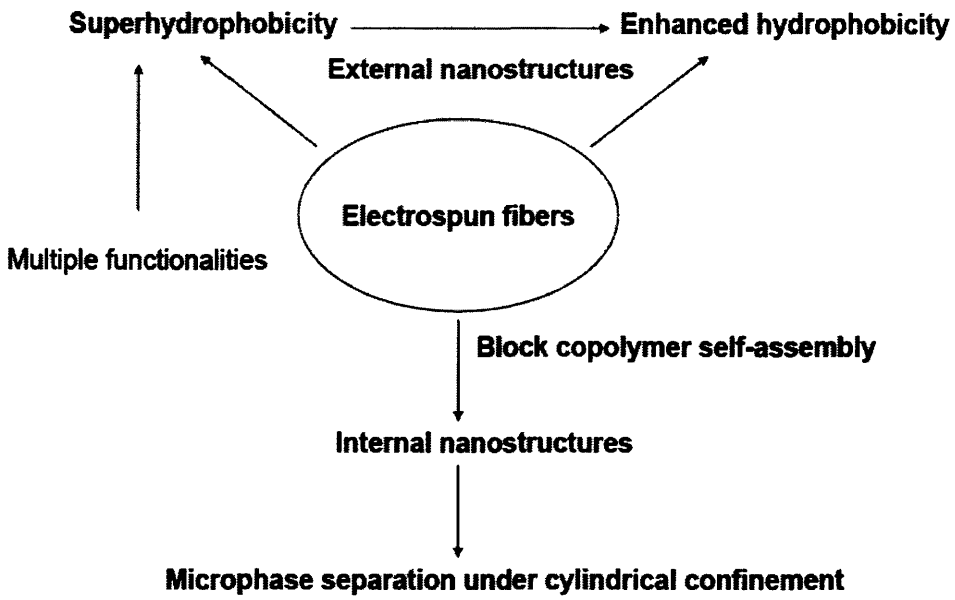

Figure 1-2 A schematic overview of this dissertation. The external and internal nanostructures of electrospun fibers serve as a thread for the thesis.

Part I

Superhydrophobic Property of Electrospun Materials

Chapter 2 Introduction to Superhydrophobicity

2.1 Wetting Phenomena, Contact Angles and Hysteresis

When a small liquid droplet is put in contact with a chemically homogeneous and physically smooth solid surface, two different equilibrium states may exist, depending on the relative values of the solid-liquid, solid-gas and liquid-gas interfacial tensions (γ_{SL}, γ_{SG}, and γ_{LG}, respectively). If the spreading coefficient $S = \gamma_{SG}-\gamma_{SL}-\gamma_{LG}>0$, the droplet spreads out and completely wets the surface, otherwise the droplet assumes a finite contact angle (θ) at the three-phase contact line.[21] The magnitude of this contact angle is described by Young's Equation, $cos(\theta_Y) = (\gamma_{SG}-\gamma_{SL})/\gamma_{LG}$. However, in real situations, many solid surfaces are not perfectly smooth or homogeneous, and as a result, the contact line is pinned not only for $\theta = \theta_Y$ but whenever θ lies within a range around θ_Y, $\theta_r < \theta < \theta_a$. Figure 2-1 shows the three possible contact angles on a surface. The difference between the advancing contact angle, θ_a, and the receding contact angle, θ_r, defines the contact angle hysteresis, $\Delta\theta = \theta_a-\theta_r$. To describe hysteresis quantitatively, different shapes of the contact lines at the defect or the details of the defect itself need to be known. In general, the hysteresis results when the contact line can assume multiple equilibrium shapes under the two competing forces, the force exerted by the defect and the elastic restoring force that tends to bring the distorted contact line back to the unperturbed position.

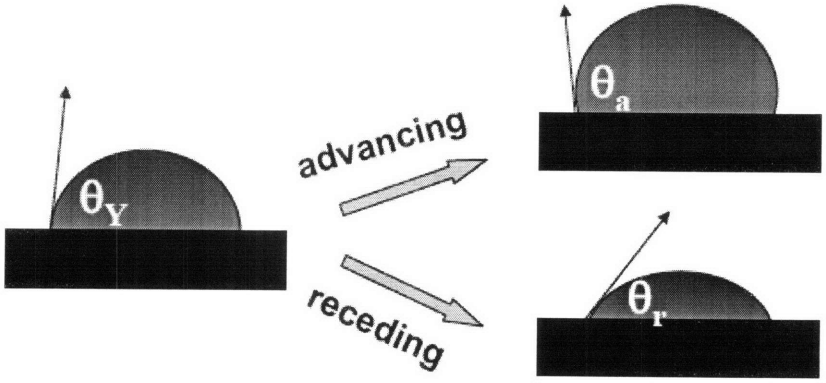

Figure 2-1 Static, advancing and receding contact angles.

2.2 Roughness-induced Superhydrophobicity

Controlling the wetting of surfaces is an important problem relevant to many areas of technology.[22] One extreme case is a surface that is not wetted by water at all. The interest in such a surface is due to its water-repellent and self-cleaning properties which are extremely useful for satellite dishes, solar energy panels, photovoltaics, exterior architectural glass, green-houses, and heat transfer surfaces in air conditioning equipment. This kind of surface is called superhydrophobic surface. It exhibits extraordinarily high water contact angle, by convention greater than 150°, and extraordinarily low contact angle hysteresis, values less than 5-10° being typical. Generally, the hydrophobicity of a solid surface can be increased by decreasing its surface energy. However, due to the limitations of surface energy, surface chemistry alone is insufficient to achieve superhydrophobicity as defined above; the largest known contact angle for a small droplet of water, on a smooth, homogeneous surface is that of a surface composed of well-aligned hexagonally packed $-CF_3$ groups (γ_S =

5.6 ~ 7.8 mN/m), with a value of 119°.[23]

Besides a relatively low surface energy, a superhydrophobic surface requires in addition a certain surface roughness. (Figure 2-2) The effect of surface roughness on the apparent contact angle θ^* was studied by many scientists since decades ago.[24] Some classic examples include those by Wenzel,[25,26] Cassie and Baxter[27,28,29] and Johnson and Dettre.[30] In the Wenzel hydrophobic state, the water droplet penetrates into the surface cavities and remains pinned to the surface, which magnifies the wetting property of the surface and leads to a high hysteresis or a high threshold sliding angle. The droplet is stable and sticks to the surface. In the Wenzel state, the surface roughness r, defined as the ratio of the actual contact area to the apparent surface area, is used to relate θ^* and θ, as $\cos(\theta^*) = r \cos(\theta)$. In the Cassie-Baxter state, the liquid does not follow the surface contours but instead bridges across the surface protrusions and sits upon a composite surface composed of both solid and air patches; in this case, the apparent liquid contact angle is described by $\cos(\theta^*) = \phi_s \cos(\theta) - \phi_v$, where ϕ_s and ϕ_v are the solid-liquid and gas-liquid contact area per unit projected surface area, respectively. The Cassie-Baxter state also has a low hysteresis and threshold sliding angle because the water can slide or roll easily when it sits partly on air; therefore, in real applications, the stable Cassie-Baxter state is generally more desirable for applications where water needs to be shed. Note that both Wenzel and Cassie Equations apply only to uniformly rough surfaces (i.e. r, ϕ_s and ϕ_v are constants) as they were initially derived. For heterogeneously rough surface, the parameters in those two equations must be local ones near the contact lines.[31,32] As

demonstrated by Johnson and Dettre, given the same surface chemistry, the Wenzel state is more stable when the roughness is low, while the Cassie state is energetically favored when the roughness is high. Quere[33,34] recently generalized the transition between these two states by comparing their corresponding energies or equivalently the two contact angle equations. A critical contact angle θ_c was obtained: $\cos(\theta_c) = -(1-\phi_s)/(r-\phi_v)$. The Cassie state has lower energy and is favored when $\theta > \theta_c$, where θ_c is larger than 90° and decreases as the roughness r increases. However, it is often observed a droplet assumes a Cassie state instead of a Wenzel one of smaller energy even when $\theta < 90°$.[35] This is because of the presence of multiple local free energy minima leading to so-called metastable Cassie states. [36,37,38] In order for these metastable states to transform to the Wenzel state of minimum energy, an energy barrier must be overcome. When this energy barrier is sufficiently high, larger than the thermal fluctuation energy which can be achieved through proper design of surface structure, it is possible to make superhydrophobic or superoleophobic surfaces from hydrophilic or oleophilic materials with $\theta < 90°$, respectively. [39,40] One of the structure designs is the "re-entrant" structure.[41] As will be described later in this dissertation, cylindrical objects like electrospun fibers arranged with their axes within the plane of the surface, are examples of re-entrant structures.

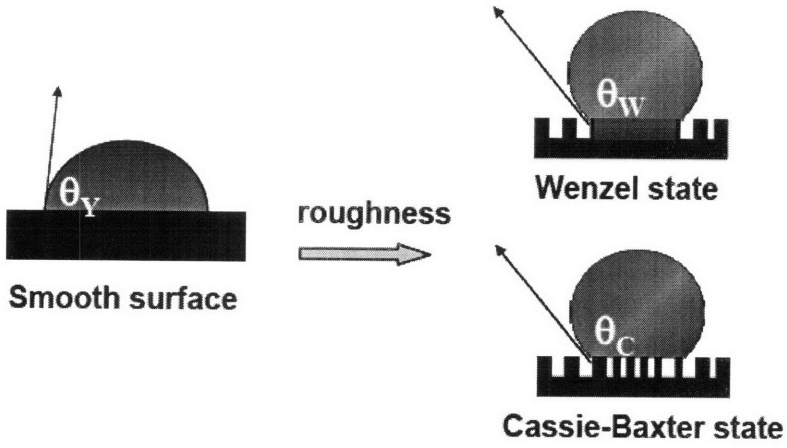

Figure 2-2 Water droplet on smooth and rough surfaces.

The stability of a water droplet on a rough surface can be analyzed using the concept of contact area and surface energy as described above, but it can also be viewed from the perspective of contact line and surface tension.[42,43,44,45] The contact line concept is particularly useful in understanding the hysteresis and the kinetics of the droplet motion. For example, in order for a droplet to move, the contact lines in the front part must advance and the contact lines in the rear part must recede, and they do so only when the advancing and receding contact angles are reached respectively through the deformation of the droplet. Both the advancing and receding events here require activation energy which is related to the greatest possible mean work of adhesion along the contact lines.

Nevertheless, surface roughness with a length scale on the order of micrometer or nanometer plays a key role in superhydrophobic surfaces. Numerous methods up to date have been reported to make rough and superhydrophobic surfaces. All the methods belong to one of the two categories: processing a relatively low surface

energy material into a rough surface or coating a rough surface with a relatively low surface energy material. Methods to make rough surfaces include mechanical stretching, laser/plasma/chemical etching, lithography, sol-gel processing and solution casting, layer-by-layer and colloidal assembling, electrical/chemical reaction and deposition, electrospinning and chemical vapor deposition. There are also several methods commonly used to modify the chemistry of a surface. For example, covalent bonds can be formed between gold and alkyl thiols. Silanes are often used to decrease the surface energy. Physical binding, adsorption and coating can also change the surface chemistry. Distinct from all the superhydrophobic surfaces made previously, the surfaces made by electrospinning described in this dissertation are in the form of free-standing, flexible and breathable micro/nano fiber mat.

2.3 Characterization of Superhydrophobic Surfaces

There are many methods to characterize superhydrophobic surfaces. Important parameters to characterize hydrophobic properties are static contact angles, advancing and receding contact angles (or hyteresis). For static contact angle, a droplet is deposited on the surface gently, and then the shape of the droplet is taken and fitted by software to get angle readings. Normally the measurement should be performed for at least 5 different drops to get a mean value. For advancing contact angle, water is gradually added to the droplet until the contact lines start to advance with a constant contact angle which is recorded as the advancing angle. Receding angle is measured in a similar way with water drawn gradually from the droplet. Sometimes, threshold

sliding angle, which is usually determined as the angle at which a droplet of given size starts sliding as the surface is tilted to increasingly large angles, is also used to characterize superhydrophobic surfaces. Figure 2-3 summarizes the four methods to characterize a superhydrophobic surface. There are a few other characterization methods. For example, Gao and McCarthy[46] proposed a way that can distinguish surfaces with a slight affinity for water and those with no affinity at all; they lowed the surface onto a supported droplet and saw if there was any attachment between the droplet and the surface during contact.

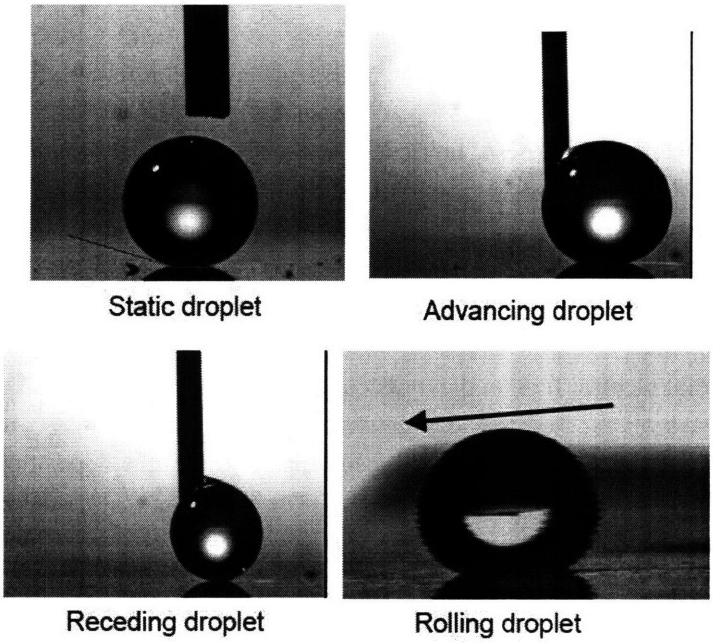

Figure 2-3 Droplet of different states on superhydrophobic surfaces.

Chapter 3 Experimental Methods

3.1 Fabrication

All the fiber mats were produced on a custom-built device that is based on Shin's and Yu's designs. The electrospinning device mainly consists of a high voltage supply, two electrodes, a syringe pump and a solution tube. The power supply (Gamma High Voltage Research ES-40P) provides up to 40 kV of direct current to the upper electrode. As a safety feature, an amperage cut-off is installed in the voltage generator to prevent electrocution. The two electrodes are two aluminum disks (12 cm in diameter and 1 cm in thickness, fabricated at the MIT Central Machine Shop) at an adjustable separation up to 50 cm. A rigid plastic lab-stand suspends the upper electrode (disk) above the lower disk. The parallel-disk arrangement provides a uniform external electric field and avoids corona discharge which can cause explosion if the fluid is volatile and flammable. It also helps to direct the deposition of the fiber onto the lower disk (collector). A 1/16 inch (1.5875 mm) hole was drilled through the upper disk at the center. From the hole, a stainless steel capillary (Upchurch® # U-138) protrudes 7 mm out. The capillary is 10 cm in length and has an inner diameter of 0.04 inch (1.016 mm) and an outer diameter of 1/16 inch (1.5875 mm). A syringe pump (Harvard Apparatus PHD 2000) delivers the fluid from the syringe to the capillary via a Teflon® tube, which serves as an electrical insulting device. A 1/8"-to-1/16" stainless steel reducing union (Ohio Valley # SS-200-6-1) connects the Teflon® tube to the capillary. The Teflon® tube (Upchurch® # 1640) has an inner

diameter of 0.062 inch (1.55 mm) and an outer diameter of 1/8 inch (3.175 mm). Its length is about 20 cm. A Luer-lock type quick-connector assembly (Upchurch® # P-628; P-345X) attaches to the other end of the Teflon® tube. The assembly provides a tie fitting to the Luer-lock syringe at the syringe pump. The entire electrospinning device is housed in a plastic enclosure with dimensions of 1 m by 0.75 m by 0.75 m. A ventilation tube attaches to the top panel of enclosure box. The tube takes all the solvent vapors in the enclosure to a solvent scrubber. In a typical operation, after the setup of the system, including filling the syringe with the solution, attaching the syringe to the Teflon® tube and placing it in the syringe pump, the flow rate is first set to a desired value, and then the strength of the electric field (voltage) is adjusted to obtain steady state jetting, such that the pulling rate is not too fast or too slow to cause interruption of the jetting, and the whipping instability persists. Sometimes, the flow rate and voltage need to be adjusted simultaneously to get stable spinning. The lower disk is positioned at a sufficient distance (35-50 cm) from upper disk, such that the fiber dries out by the time it hits the collector. To collect fibers, the collector is covered by an aluminum foil (Reynolds Wrap® ReleaseTM Non-Stick Foil) on which silicon wafers or glass slides might be placed as well to get samples for additional treatment or characterization.

The initiated chemical vapor deposition (iCVD) was conducted in a custom-built cylindrical reactor (240 mm diameter, 33 mm height) by Dr. Malancha Gupta and Dr. Jessie Mao in Prof. Karen Gleason Group. The iCVD polymerization is a relatively low energy vapor deposition process (0.01 W/cm^2) that produces polymeric thin films

in one step from vapor phase. This all-dry process has environmental benefits because no solvents are used. It also avoids the surface tension problems associated with liquids and thus can be used to conformally coat complex geometries with nanoscale film thicknesses such as electrospun fibers in this thesis work. The mechanism of iCVD involves the classical free radical polymerization of vinyl monomers. In a typical process, monomer and initiator gases are fed into a vacuum chamber where the initiator gas is thermally decomposed into free radicals by the resistively heated wires. The free radicals and monomer gas diffuse and adsorb onto the substrate whose temperature is kept cool to promote the adsorption. The polymeric thin film is formed after the initiation, propagation, and termination that occur on the substrate. In this thesis work, perfluoroalkyl ethyl methacrylate (PFEMA, $CH_2=C(CH_3)COOCH_2CH_2(CF_2)_nCF_3$ where n = 5-13, n_{avg} = 8, Zonyl®) was used as the monomer and tert-butyl peroxide (98%, Aldrich) was used as the initiator. The PFEMA monomer was heated to 90 °C and fed into the chamber at a flow rate of 0.8 sccm through a heated mass flow controller (Model 1152C, MKS) and the initiator tert-butyl peroxide was kept at room temperature and fed into the chamber at a flow rate of 0.1 sccm through another mass flow controller (Model 1479A, MKS). The reactor pressure was kept constant at 300 mTorr. Nichrome filaments (80% Ni/20% Cr) were resistively heated to 250 °C. The distance between the filaments and the substrate was kept at 29 mm. The electrospun fiber mats were placed onto a stage that was backside cooled to a constant temperature of 44 °C using water from a re-circulating chiller. The film thickness was measured on a reference silicon wafer

using profilometry (Tencor P10). The reaction mechanism for PPFEMA iCVD is shown in Figure 3-1.

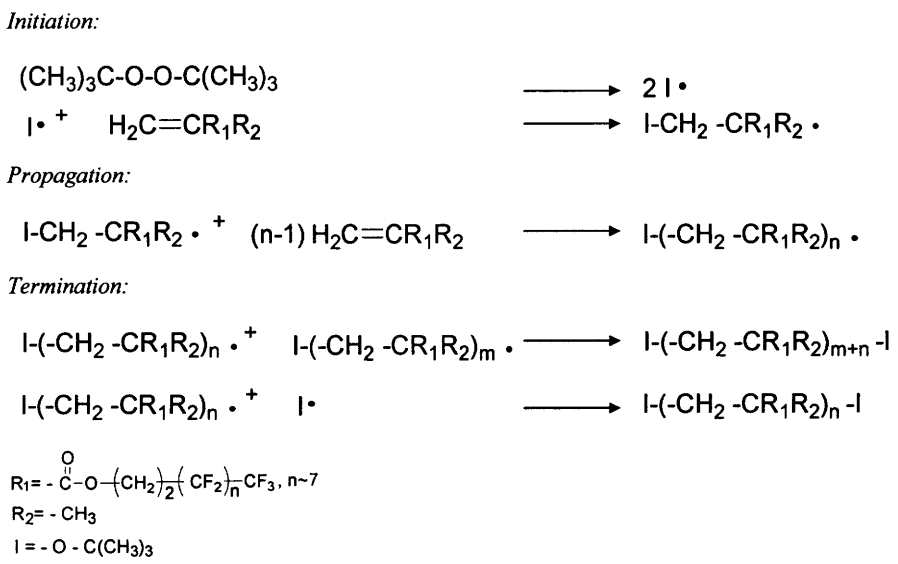

Figure 3-1 Reaction mechanism for PPFEMA iCVD with tert-butyl peroxide as an initiator.

The layer-by-layer (LBL) deposition used in this thesis work was conducted by collaborators in Prof. Robert Cohen Group and Prof. Michael Rubner Group. The LbL assembly is another versatile way to create conformal thin film coatings with molecular level control over film chemistry and thickness. It involves the sequential adsorption of two materials that interact with each other through different types of intermolecular interactions such as electrostatic attraction and hydrogen bonding. In a typical process, a substrate is alternately exposed to solutions containing complementary materials, such as positively and negatively charged species or polymers with hydrogen-bond donor and acceptor groups. Here in this thesis work, the LBL deposition was used to create hierarchically roughened fibers by decorating

electrospun fibers with nanoparticles. The SiO_2 nanoparticles (Polysciences) with an average diameter of 50 nm according to the manufacturer were decorated onto the electrospun fiber surfaces via the alternating deposition of a polycation, poly(allylamine hydrochloride) (PAH, Mw = 70 kDa) from aqueous solutions (pH 8.5, 0.01 M by repeat unit, 15 min immersion, 5 min water rinse) and the negatively charged nanoparticles from a 0.06 wt% aqueous colloidal dispersion (15 min immersion, 5 min water rinse).

3.2 Characterization

The surface structure of electrospun fiber mat was generally observed by using scanning electron microscope (SEM) and atomic force microscope (AFM). For SEM, a small piece of the fiber mat was taped onto a double-sized copper tape and then sputter-coated with a 2-3 nm layer of gold for imaging using a Desk II cold sputter/etch unit (Denton Vacuum LLC, NJ). A JEOL-6060SEM (JEOL Ltd, Japan) SEM was used to get low resolution images of the fibers. The high-resolution SEM images for the fibers were obtained by a JEOL 6320FV Field-Emission High-resolution SEM. The fiber diameters were determined using AnalySIS image processing software (Soft Imaging System Corp., Lakewood, USA). For AFM, the fibers were deposited on a flat and hard substrate such as a glass slide. A Nanoscope IV, Dimension 3100 AFM (Digital Instruments, Santa Barbara, CA), in tapping mode, was used to image the surface structures. Sometimes, it is relatively easy to image single fibers instead of fiber mats using AFM due to the fluffy nature of the mats.

The surface chemistry of the fibers was characterized using a Kratos Axis Ultra X-ray photoelectron spectrometer (XPS) (Kratos Analytical, Manchester) with a monochromatized Al Kα X-ray source. The take-off angle relative to the sample substrate for the measurements was normally located at 90°. However, for a fiber sample, the local take-off angle comprises a distribution including all angles between the normal and glancing angles. This means that the effective sampling depth for a randomly oriented fiber sample will be less than the approximately 6 nm value expected for a flat solid surface. Since we only seek a qualitative determination of surface chemistry in this thesis work, no attempt was made to obtain a better estimate of the actual sampling depth. A low resolution scan was deemed adequate for this purpose.

The contact angle on the electrospun mat was measured using a Contact Angle Meter G10 (Kruss, Germany) or a VCA2000 (AST Inc.) goniometer. The contact angles were determined by fitting the profile of at least 5 droplets; the typical standard deviation in contact angle was approximately ±1.5°. The initial contact angles were recorded within 30s after placing droplets of about 2-5 μL on the fiber mats. Advancing and receding contact angles (or hysteresis) were obtained by adding or removing water from the droplet. In some cases where the receding contact angles were too high to measure by removing water (The droplet detached the surface directly), an evaporation method was used. In this method, as the droplet on the mat evaporated under ambient condition for about 25 minutes, the contact angle changed to a receding value. The threshold sliding angles were determined by first placing a 20

mg droplet gently on a level surface (Tilt stage, THORLABS) and then slowly tilting the surface until the droplet started moving.

3.3 Chemicals

The polymers used in this part of research, unless otherwise specified, were mainly purchased from Scientific Polymer Products, Inc. and Aldrich Chemical Co. Most of the solvents were purchased from Aldrich Chemical Co. All the chemicals were used as received without further purification.

Chapter 4 Making Superhydrophobic Mats by Electrospinning

As introduced above, surface structure or roughness with a length on the micrometer or nanometer scale plays a key role in the realization of superhydrophobic surfaces. Among the various types of surface structures and roughness, the case of fibrous structure is of particular importance in many practical applications. This class of materials may have appropriate surface roughness for superhydrophobicity when the diameters of individual fibers fall in the range of micron (1-100 μm), submicron (0.1-1 μm) and nanometer (<100 nm) sizes. A significant contribution of this thesis is the discovery of electrospun fiber mats having the right surface roughness for superhydrophobicity. Two different strategies, either electrospinning hydrophobic materials directly or modifying pre-made electrospun mats with low surface energy materials, have been demonstrated to make superhydrophobic fabrics.

4.1 Electrospinning Hydrophobic Materials into Fibers

Polystyrene (PS) is a simple and relatively cheap material. The pure hydrocarbon structure renders PS a hydrophobic property with water contact angle of about 90° for a smooth film. Simply processing PS into uniform electrospun fibers with diameter in the range of 200 nm to a few micrometers improves the hydrophobic property, with contact angle up to 140°. However, by introducing into PS fibers the beaded structures, the role of which in making superhydrophobic fabrics will be discussed in detail in next chapter, superhydrophobic mats were easily produced. (See Figure 4-1) The

beaded PS fiber mats were made by electrospinning from a 20 wt% PS (Mw = 280 kDa) solution in *N,N*-dimethylformamide (DMF) using the device described in the experimental part with operating parameters, voltage V = 20 kV, flow rate Q = 0.02 ml/min and disk-to-disk distance Z = 40 cm. The size of the beads is about 8 μm, while the strings between beads have diameters of 150 nm to 600 nm. The water contact angle on the beaded fiber mat is 150° with hysteresis about 20°. Due to the intrinsic oleophilic property of PS, this mat is also superoleophilic. One application of such material is the separation of water and oil. To demonstrate this, PS beaded fibers were deposited on a copper mesh (0.5 mm diameter) with an areal density of 0.01 g/cm^2 and a mixture of water (dyed green with food dye) and octane (dyed red with Oil Red O) was used as a model system. As the four successive photos (Figure 4-1 c-f) taken from the separation process shows, the water stays on the mat while the oil penetrates it, and at the end, the water can be fully recovered. A second application of such a mat is to selectively absorb the spilled oil (e.g. octane), as shown in Figure 4-1 (g)-(i).

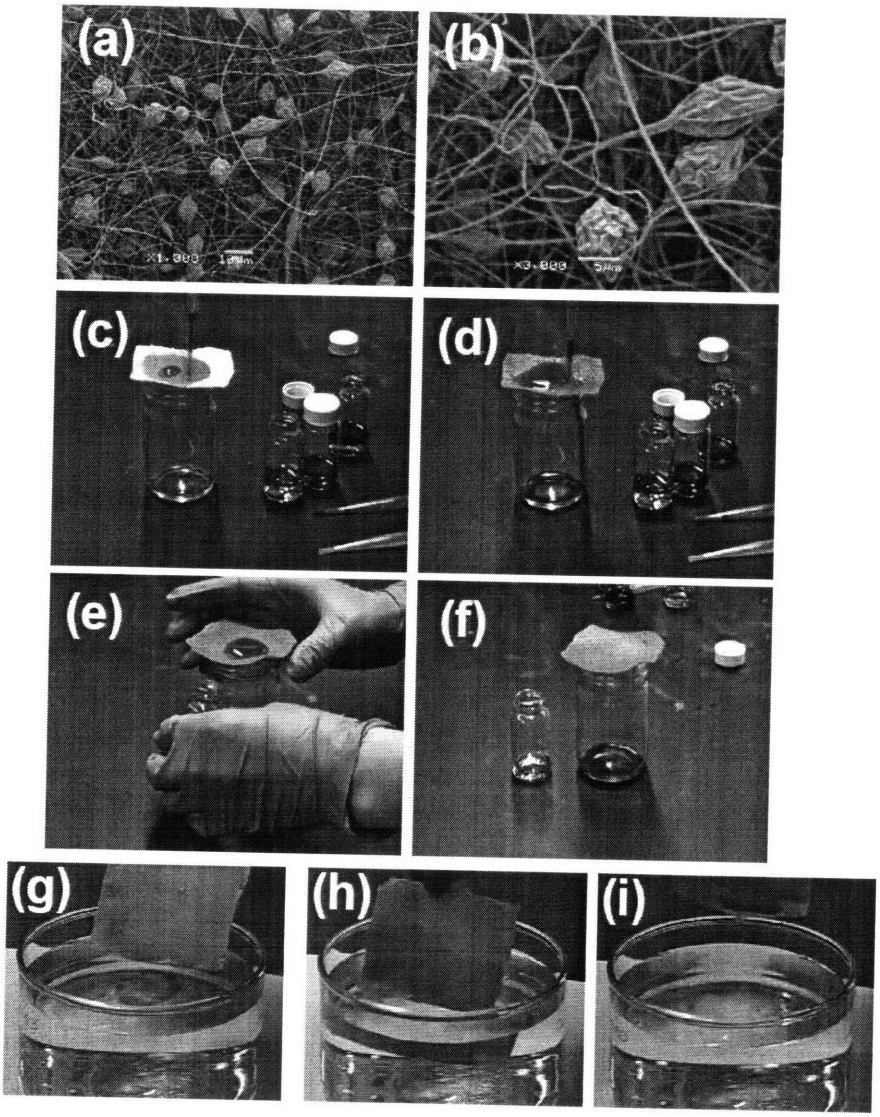

Figure 4-1 Superhydrophobic/superoleophilic property of electrospun PS fiber mats. (a) and (b), SEM images of the beaded PS fiber mat; (c)-(f), water/octane separation process using the PS fiber mat. (g)-(i), pickup of the spilled oil using the PS fiber mat.

Polydimethylsiloxane (PDMS) is a well-known hydrophobic polymer with better repellency for water than PS; crosslinked silicone elastomers ($\theta = 112°$ for a smooth film) are commonly used for fabricating microfluidic devices. However, forming solid fibers comprised solely of linear PDMS is not possible, due to its low glass transition temperature. Instead of using linear homopolymer PDMS, a

poly(styrene-*b*-dimethylsiloxane) block copolymer blended with 23.4 wt% homopolymer polystyrene (PS-PDMS/PS, provided by Dow Corning Corporation) was used to make fibers. [47] The copolymer has a molecular weight Mn = 238 kDa, polydispersity index PDI = 1.12 and PS volume fraction f = 0.45. The homoplomer PS has a molecular weight of 114 kDa. A mixture of tetrahydrofuran (THF) and DMF (3:1 by volume) was used as the solvent. The resultant fiber mat shown in Figure 4-2, with fiber diameters in the range of 150 nm to 400 nm, was obtained from a 21 wt% solution under the operating condition of V = 30 kV, Q = 0.05 ml/min and Z = 50 cm. The mat exhibited a contact angle of 163° and a hysteresis of 15°. An illustration of water droplets beaded up on such a mat is provided in Figure 4-2 (c). This is the first demonstration of a superhydrophobic mat composed of electrospun fibers without any beaded structures. A PS mat of similar fiber diameter and porosity (pore sizes ranging from 0.2 to 1.5 μm , as determined by Hg porosimetry, Quantachrome Instruments Poremaster 33) did not have superhydrophobic property as mentioned above; it exhibited a contact angle of only 138°. The difference was attributed to the lower surface tension of PDMS (19.9 mN/m compared to 40.7 mN/m of PS), combined with its spontaneous segregation to the fiber surface. X-ray photoelectron spectroscopy (XPS) results confirmed that the fiber surface was enriched with PDMS relative to the bulk composition. From the bulk material composition, the atomic ratio of silicon to carbon is about 1: 10.6. According to the XPS data shown in Figure 4-2 (d), the surface layer within a few nanometers of the fiber surface has this ratio of 1: 5.5, indicative of surface enrichment with the PDMS component. Adventitious carbon

would increase this ratio, which means the actual PDMS surface enrichment could be slightly better than the XPS data suggests. A similar enrichment with PDMS was reported for the films of PS-PDMS/PS blends.[48]

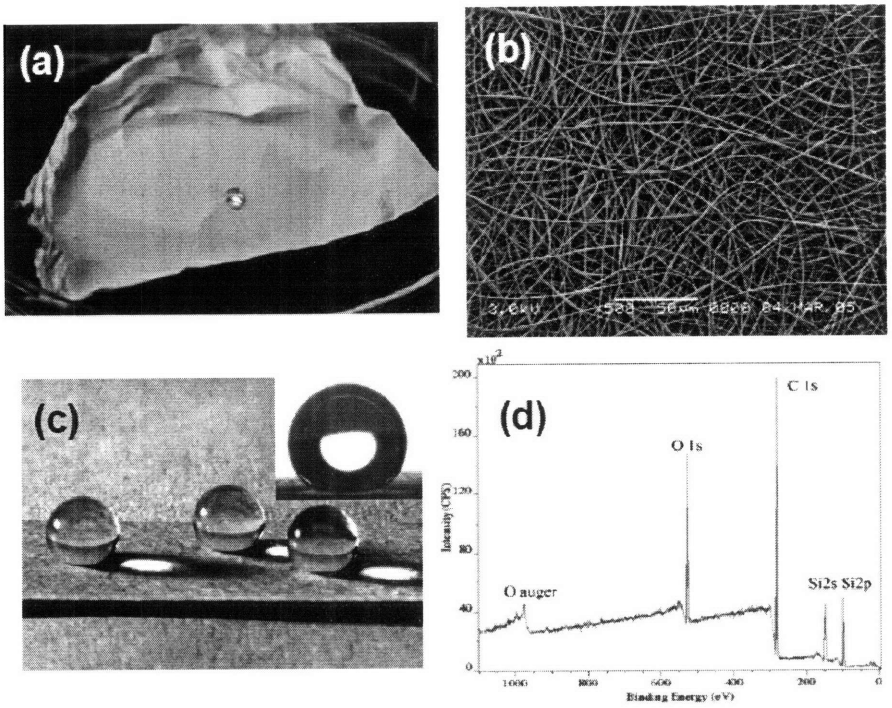

Figure 4-2 Superhydrophobic property of electrospun PS-PDMS/PS fiber mat. (a) and (b), Digital photo and SEM image of the fiber mat; (c), Three water droplets (~20 μL) on the mat; the inset is the contact angle measurement; (d), XPS data for the fiber mat.

Fluorinated polymers are another class of low surface energy materials. However, most common fluorinated polymers such as Teflon® are not soluble or electrospinnable. To take advantage of the low surface energy property of fluorinated materials and make superhydrophobic surfaces from them using electrospinning, one way is to blend them with an electrospinnable polymer. To prove this concept, in the collaboration with Prof. Gareth McKinley Group and Prof. Robert Cohen Group, we blended poly(methyl methacrylate) (PMMA, Mw = 540 kDa) with a class of

hydrophobic polyhedral oligomeric silsesquioxane (POSS) molecules in which the rigid silsesquioxane cage is surrounded by perfluoro-alkyl groups (fluoroPOSS). The high surface concentration and surface mobility of $-CF_2$ and $-CF_3$ groups, together with the relatively high ratio of $-CF_3$ groups with respect to $-CF_2$ groups, results in a very hydrophobic material with low surface energy. A film of fluoroPOSS, spin-coated on a Si wafer, has an advancing and receding contact angle of 124.5° ± 1.2°, with a root mean square (RMS) roughness of 3.5 nm. For electrospinning, both the PMMA polymer and fluoroPOSS were dissolved in Asahiklin AK-225 at a ~ 5 wt% PMMA concentration and different concentrations of fluoroPOSS. The solution was then electrospun with the flow rate, plate-to-plate distance and voltage set to 0.05 ml/min, 25 cm and 20 kV, respectively. In Figure 4-3 (a), we show the advancing and receding contact angles with water for the various electrospun fluoroPOSS–PMMA surfaces. The inset shows the "beads on string" morphology of a representative fiber mat. There is no observable change in the micrometer scale structure with increasing mass fraction of POSS as viewed from SEM images. The result of XPS analysis (Figure 4-3b) indicates substantial surface migration of the fluoroPOSS molecules during electrospinning due to their low surface energy property, as in the case of PS-PDMS/PS described above. Although PMMA itself is not hydrophobic ($\theta = 69°$), the surfaces become superhydrophobic ($\theta^* = 160°$, $\Delta\theta \sim 0°$) for all POSS mass fractions above ~10 wt % in the electrospun fibers.

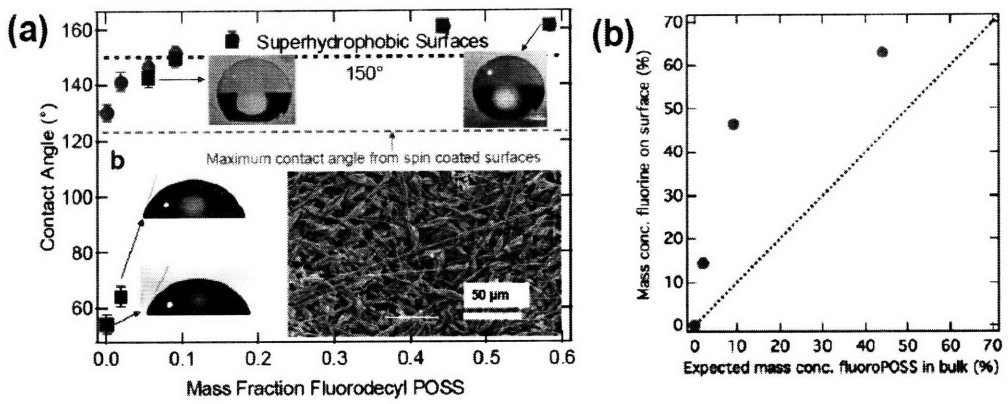

Figure 4-3 Tunable hydrophobic property of electrospun PMMA/fluoroPOSS fiber mats. (a), Advancing (dots) and receding (squares) contact angles as a function of the mass fraction of fluoroPOSS; (b) XPS data showing the mass concentration of fluorine on the surface of the fibers as a function of the expected mass concentration of the fluoroPOSS in bulk.

4.2 Applying Hydrophobic Coating to Electrospun Fibers

Electrospinning hydrophobic materials as described in 4.1 represents a method to make a superhydrophobic surface in fibrous form in a single process step, but this method is generally applicable to only a few types of relatively low surface energy materials that are readily spun into fibers. An alternative way to make superhydrophobic micro- and nanofibrous surfaces is to apply a conformal, nanometers-thick hydrophobic coating on a pre-formed electrospun fiber mat. This two-step process takes advantage of the intrinsic roughness of electrospun fiber mat and relieves the requirement of low surface energy for the fiber composition, since this is now provided by the low surface energy hydrophobic coating. The selection of materials for the electrospun fiber substrate can therefore be based on other performance criteria, such as toughness or thermal stability.

The first method for the post-spin hydrophobic coating is a dip-coating. This method is extremely simple and does not require sophisticated equipments. In a typical coating process, an electrospun fiber mat is gently put into a solution containing low surface energy species. The mat is then dried after it is completely wetted by the solution. Figure 4-4 shows SEM images and corresponding water repellency of an electrospun Nylon fiber mat before and after dip-coating in a 0.1 wt% silicone-resin solution in toluene. The Nylon-6 (polycaprolactam, Dupont, Zytel Nylon Type 101) fibers were made by electrospinning a 10 wt% solution in 1,1,1,3,3,3-hexafluoro-2-propanol (HFIP), with the flow rate, plate-to-plate distance and voltage set to 0.04 ml/min, 45 cm and 25 kV, respectively. The silicone-resin (provided by Dow Corning Corporation) has a POSS-like structure with eight hydrophobic groups (-$OSi(CH_3)_3$) surrounded, as shown in the inset of Figure 4-4 (b). This simple dip-coating transformed a moderate hydrophobic mat into a superhydrophobic one without significantly changing its fibrous structure.

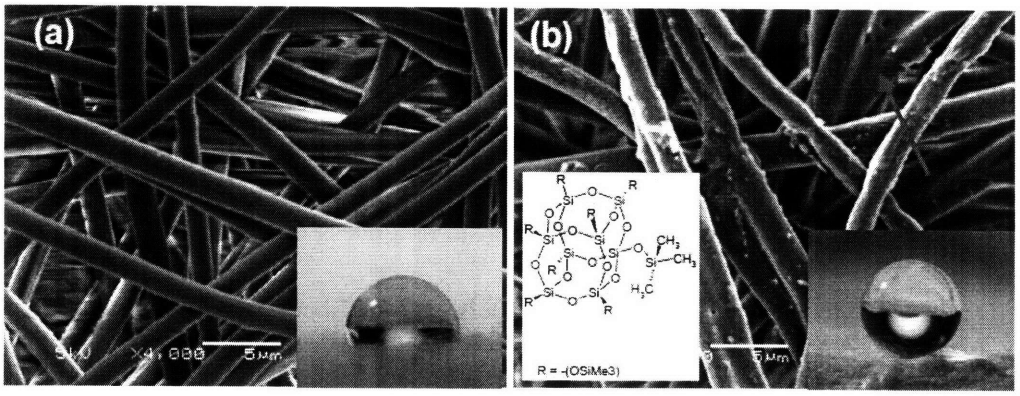

Figure 4-4 Superhydrophobic mat made by dip-coating method. (a), SEM image of the as-spun Nylon mat. (b), SEM image of the coated one. The insets show images of water droplet on the corresponding mat and the molecular structure of the silicone-resin. Note that the dip-coating is not conformal in some locations such as the one indicated by the arrow.

The dip coating method is simple but has a number of limitations. For example, the coating is not uniformly conformal and the solvent used in the coating may dissolve the fiber material. A more versatile and robust method for post-spin hydrophobic coating is to use a chemical vapor deposition.[49] Any electrospinnable material, including those that may dissolve or decompose upon exposure to certain solvents or high temperatures, can be used to make superhydrophobic fiber mats by this route. Fluoropolymer coatings are well known for their low surface energies. The initiated chemical vapor deposition (iCVD) technique has been successfully applied in polymerizing perfluoroalkyl ethyl methacrylate (PFEMA, $CH_2=C(CH_3)COOCH_2CH_2(CF_2)_nCF_3$ where n=5-13, n_{avg}=8, Zonyl®) using tert-butyl peroxide as an initiator.[50] The dispersive surface energy of the resulting poly(PFEMA) (PPFEMA, see Figure 4-5 (a) for the structure) coating is 9.3 mN/m. The water contact angle on a PPFEMA coated smooth surface (silicon wafer) is about 119°, as shown in Figure 4-5 (b).

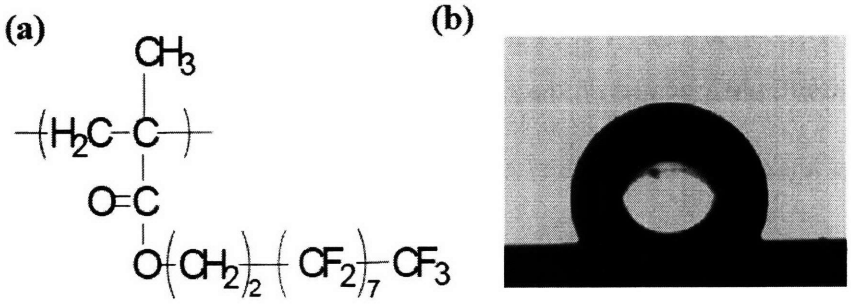

Figure 4-5 Molecular structure and hydrophobic property of PPFEMA. (a), Molecular structure of the PPFEMA; (b), Contact angle measurement on a PPFEMA coated silicon wafer.

To decrease the surface energy while maintaining the inherent surface roughness of the electrospun mats, the iCVD coating must be thin and conformal. In order to find an optimal coating thickness, we coated 3 different (sample a, b and c) poly(caprolactone) (PCL, Mw = 80 kDa) fibers with 4 different (sample 1, 2, 3 and 4) coating thickness. Figure 4-6 shows SEM images of all the coated mats. From left to right (sample 1 to 4), the thickness of the PPFEMA coating is 120, 300, 350, 800 nm, respectively. Note that the coating thickness here was obtained from a reference silicon wafer placed besides the mat in the CVD chamber. It is difficult to determine the actual coating thickness on the fibers that is anticipated to be smaller due to the high surface area of these fibers. From these SEM images, we see that as the coating thickness increases, small beaded structures appear especially on the fibers with small diameters. The beading phenomenon is an evidence of the surface-tension driven Rayleigh instability, as sometimes occurs on the polymeric liquid jet in electrospinning. Since surface tension effect is inversely proportional to the fiber size, smaller fibers tend to have these beaded structures from the coating more easily. In addition, thicker coatings generally lead to more beading. This is because for thick coatings the PPFEMA coated on the fibers at an earlier stage decreases the surface energy and make the fibers hard to coat conformally later on. Contact angle measurements on these coated samples indicate that as the coating thickness increases, the hydrophobicity also decreases. From these observations, we conclude that for electrospun fibers, thin (~100 nm or thinner) coatings are better to get conformal coating and superhydrophobic mats.

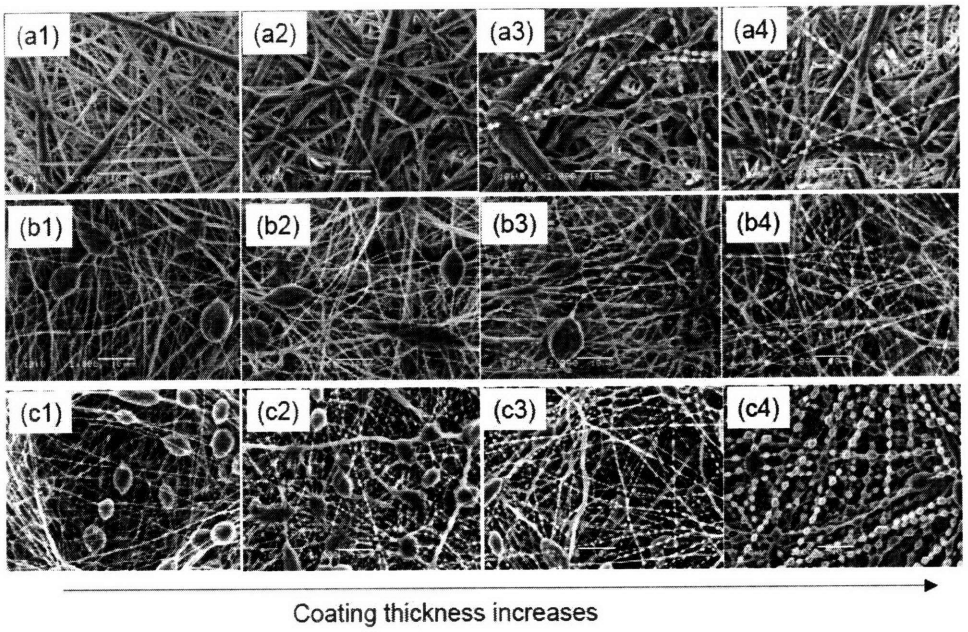

Figure 4-6 Conformal iCVD and "beaded" iCVD. SEM images of 3 different (a, b and c) PCL electrospun fiber mats coated with PPFEMA of 4 different thickness (1-4 with increasing coating thickness). For the fibers with beaded structures, the small beads are from iCVD coating and large beads are from electrospinning.

Indeed, a thin coating is more conformal and effective in obtaining superhydrophobic mats. Figure 4-7 (a) and (b) show representative SEM images of a PCL mat before and after 70 nm coating. The conformal nature of this thin iCVD coating results in little overall change in the hierarchical nature of the mat morphology, the only visually observable change being the slight increase in fiber diameter. XPS scans were used to verify further the presence of PPFEMA on the coated mats. Figure 4-7 (c) and (d) show the XPS scans of an as-spun PCL mat and the same mat coated with PPFEMA. Figure 4-7 (d) shows that the PPFEMA-coated mat contains a strong peak in the 690-700 eV region. This peak is characteristic of fluorine 1s and indicates the presence of PPFEMA on these substrates. The XPS scan

of the uncoated mat in Figure 4-7 (c) confirms that it does not contain any characteristic fluorine peaks, as expected.

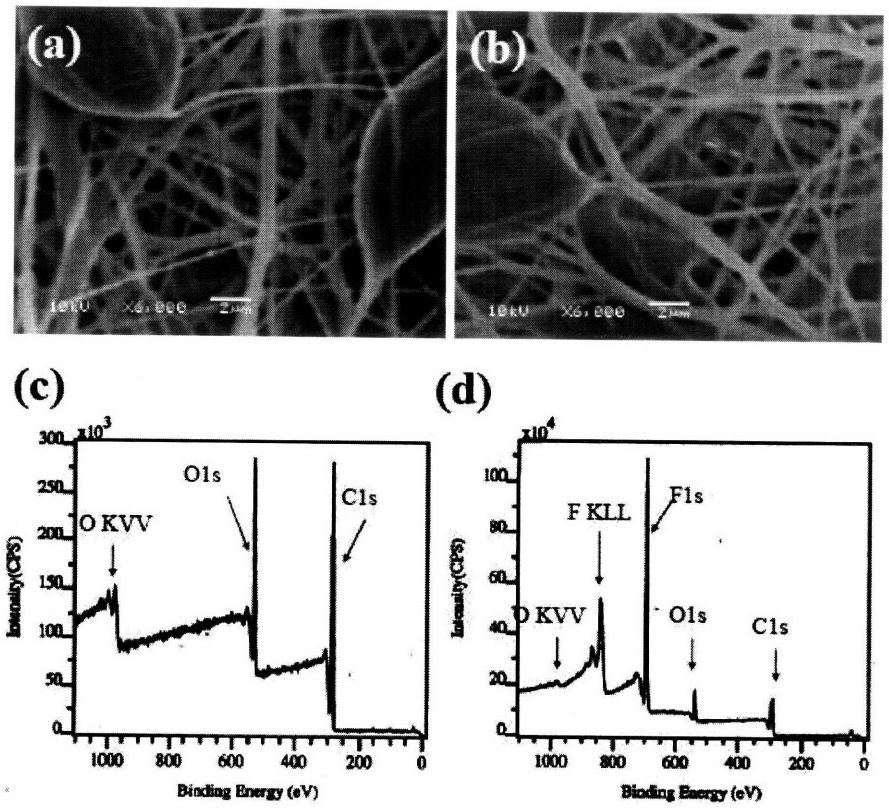

Figure 4-7 Properties of conformal iCVD coating. (a) and (b), SEM images of an PCL electrospun fiber mat (a) before and (b) after 70 nm iCVD coating showing the conformal nature of this thin coating; (c) and (d) are corresponding XPS data for (a) and (b), respectively.

The electrospun fiber mat after this 70 nm conformal coatings exhibits extreme hydrophobicity. Figure 4-8 (a)-(d) show larger scale SEM images and the superhydrophobic property of the coated mat. The contact angle is over 170° with a threshold sliding angle of a couple of degrees. As mentioned at the beginning of this section, the iCVD method can be applied to virtually any electrospun fiber mats. To demonstrate this concept, a second example where a Nylon fiber mat was used as the

substrate is shown in Figure 4-8 (e)-(f).

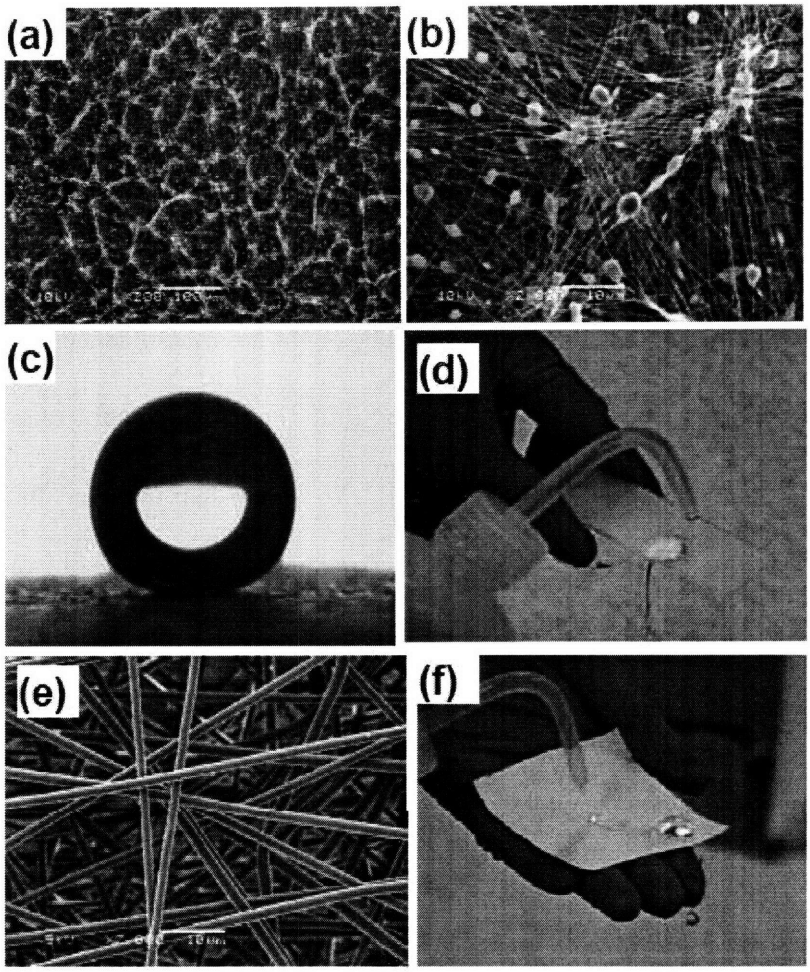

Figure 4-8 Superhydrophobic property of 70 nm PPFEMA coated electrospun fiber mats. (a) and (b), SEM images of a PCL fiber mat, showing the hierarchical surface roughness; (c) A water droplet on the coated PCL mat; (d) A snapshot of a movie demonstrating the roll-off of water on such a mat; (e) and (f), SEM image of a coated Nylon fiber mat and its superhydrophobic property. Note that water droplets roll off the mat instantaneously.

The superhydrophobic property of the PPFEMA-coated electrospun mats were further characterized by water condensation experiment and test of surfactant solution. Figure 4-9 (a) and (b) show SEM images taken from an environmental SEM (Philips/FEI XL30 FEG ESEM) with a water vapor pressure of 5 Torr in the chamber

and sample stage temperature of 3 °C. Micrometer sized water droplets with nearly spherical shape suspended on individual fibers (a) or on the mat surface (b) are clearly seen. These droplets evaporated as the vapor pressure was decreased and condensed again when the vapor pressure was increased. Repeated cycles of evaporation and condensation had no effect on the structures of the fiber mat and were essentially reversible. Figure 4-9 (c) and (d) are digital photos for droplets of aqueous surfactant solution containing quantum dots (provided by Prof. Moungi Bawendi Group at MIT) on the fiber mat under ambient light and UV light, respectively. Although the surfactant decreased the surface tension of water, the droplets maintained high contact angles on the mat. The photoluminescence of the quantum dots makes the droplet shining under UV light. In principle, if the droplet is small enough (diameter < 100 μm), it may become an optical microcavity.[51]

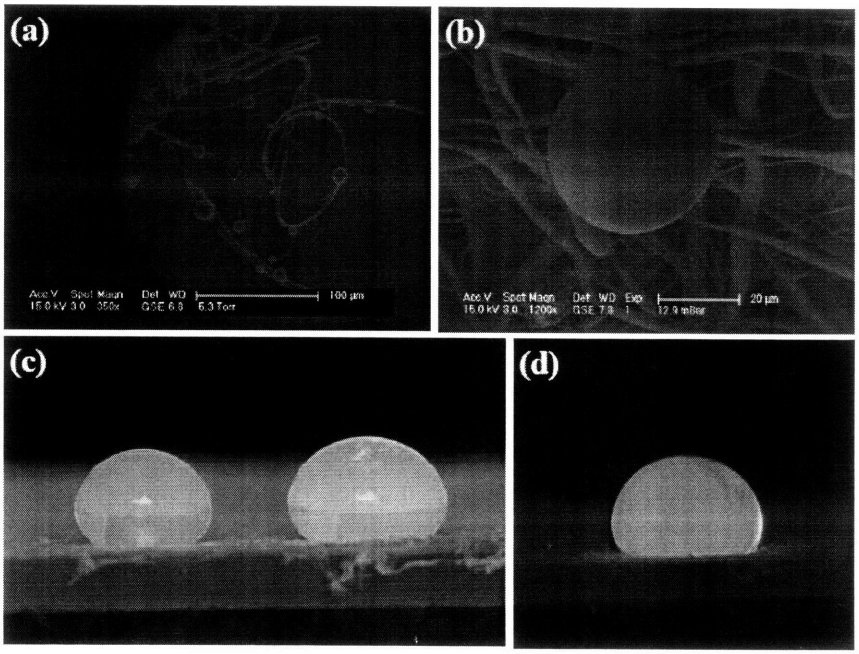

Figure 4-9 Repellent to water vapor and surfactant solution. (a) and (b), ESEM images water droplets condensed on the PPFEMA-coated electrospun fibers; (c) and (d), Droplets of quantum dots solution on the mat.

These PPFEMA-coated electrospun mats also showed a respectable oleophobicity. Oleophobicity has received much less attention,[52] but is often more desirable than simple superhydrophobicity and is generally more difficult to achieve. Oleophobicity together with superhydrophobicity can significantly enhance the self-cleaning ability of a surface, especially the resistance to organic contamination. Oleophobicity of the PPFEMA-modified PCL mats was measured using AATCC (American Association of Textile Chemists and Colorists) test method 118-1997, [53] in which the material is challenged with a series of test liquids, including n-decane, n-octane and n-heptane. The contact angles (See Figure 4-10) of these three alkanes on the PPFEMA-coated fiber mat are 118°, 109°,and 92°, respectively, which are much larger than those on the PPFEMA-coated Si wafer (53°, 45°, 32°, respectively), indicating at least a Grade-8 (n-heptane-phobic) oil repellency. Since the intrinsic contact angle for n-heptane on the a smooth PPFEMA film is less than 90°, the apparent contact angles on a rough PPFEMA surface should be even lower, according to the Wenzel equation. From this, we conclude that the alkane droplets are in metastable Cassie-Baxter state, similar to the case for water on as-spun PCL mats as will be discussed in more details in next chapter. The 5μL droplets of n-decane, n-octane and n-heptane at ambient temperature in stagnant air exhibit contact angles lower than 90° in periods of about 39, 6 and 1 minutes, respectively. We anticipate that these times would also depend on the alkane evaporation rate, which includes factors such as temperature, air velocity,

and droplet size.

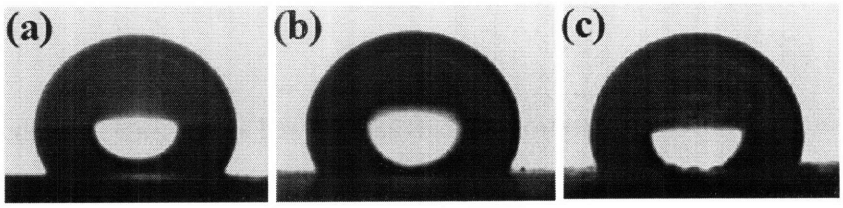

Figure 4-10 Repellent to oils (alkanes). (a) n-decane, (b) n-octane, and (c) n-heptane droplets on the PPFEMA-coated fiber mat. The contact angles are 118°, 109°, and 92°, respectively.

Chapter 5 The Effect of Fiber Morphology on Superhydrophobic Property of Electrospun Fiber Mats

The conformal nature of the 70 nm iCVD coating and its nanometer-scale thickness as described above not only provides the desired surface chemistry but also ensures that the surface structure remains unchanged after coating. Taking advantage of this decoupling of surface chemistry from surface structure, one can investigate the effect of fiber size and morphology on superhydrophobicity with greater control.

5.1 Experimental Results

PCL is selected for the substrate material here because of the ease with which fibers can be formed over a range of diameters, which in turn permits a more detailed study of the role of fiber morphology on hydrophobicity. The morphology of PCL fibers can be simply tailored by varying the concentration and operating parameters during electrospinning. A series of PCL solutions of different concentrations were made with a mixture of chloroform and methanol (3/1 by weight) as the solvent. The concentrations and operating parameters are summarized in Table 5-1. PCL mats with different fiber morphologies, including beaded fibers and bead-free fibers as well as variations in fiber diameter, were obtained by varying the concentrations and operating parameters during electrospinning (See Table 5-1). Selected SEM images are shown in Figure 5-1. As the label index increases, the average fiber diameter decreases for both the bead-free and beaded fibers as quantified in Table 5-1. For

beaded fibers, the average diameter refers to the diameter of the threads between the beads. Additionally, the bead size decreases and the bead density increases with increasing label index of the beaded samples. The areal bead density can be defined as the number of beads per unit area, while a linear bead density can be defined as the number of beads per unit length of fiber. However, both of these are difficult to quantify in a meaningful way, since the areal bead density depends also on the thickness of the mat and the density of fibers therein, while the linear bead density requires an analysis of the total linear length of fibers as well as a count of the number of beads present in a sample of material. Here we characterize the bead density only in a qualitative sense (i.e. through visualization) under the assumption that mat thickness and fiber density are qualitatively similar for all mats. The transition here from bead-free fibers to beaded fibers is believed to be a result of the late onset of nonlinear viscoelastic effects during growth of a Rayleigh instability in the whipping portion of the jet.

Sample index	Concentration (wt%)	Flow rate (ml/min)	Voltage (KV)	Plate-to –plate distance (cm)	Fiber morphology	
					Average fiber diameter (nm)	Average bead size (nm)
F1	11.5	0.05	37.6	27	2200	no bead
F2	10.0	0.05	35.0	27	2000	no bead
F3	9.2	0.025	32.5	27	1900	no bead
F4	7.6	0.025	18.6	40	1400	no bead
F5	7.1	0.025	25.9	40	620	no bead
F6	7.1	0.025	35.0	27	580	no bead
B1	6.4	0.05	33.0	27	590	7350
B2	6.7	0.025	23.1	40	320	6760
B3	5.2	0.025	22.5	40	210	5880
B4	4.0	0.05	25.4	45	180	3530
B5	2.0	0.05	25.4	45	110	2650

Table 5-1 Solution concentrations, operating parameters and average fiber diameter and bead size of PCL electrospun mats. . Sample labels starting with "F" are bead-free

fibers while those starting with "B" are beaded fibers.

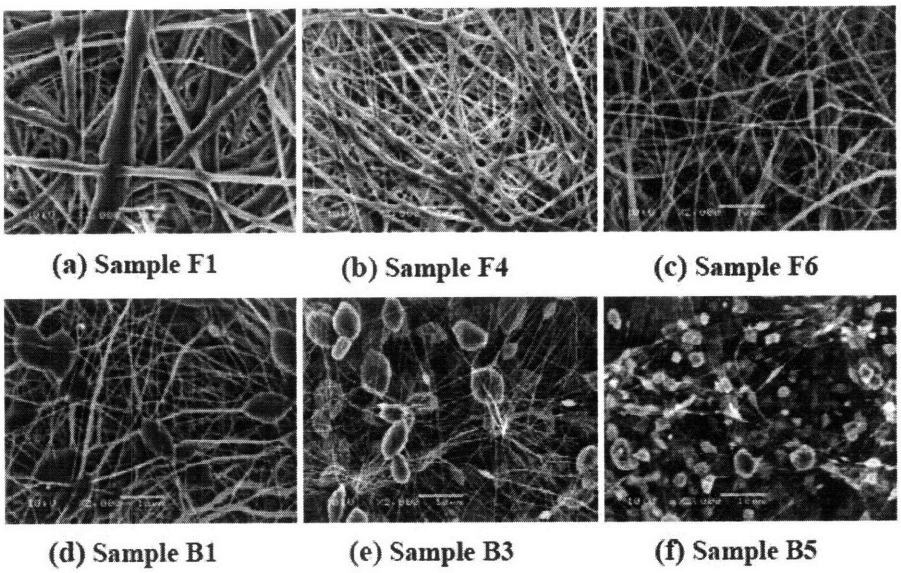

Figure 5-1 Typical SEM images of the PCL electrospun mats used for the study of fiber morphology effect. Scale bars=10μm.

We first studied the hydrophobicity of the as-spun PCL mats. Figure 5-2 shows how the initial contact angle (measured within 1 min of placement of the drop on the mat) varies with average fiber diameter. Selected droplet images are shown in the inset. An important observation from Figure 5-2 is that all the contact angles (θ^*) on the as-spun PCL mats are much larger than 90°, even though the PCL is not a hydrophobic material (PCL solution cast film shows a contact angle θ of 60°). This is surprising, because for $\theta < 90°$ the rough surfaces are expected to be in the Wenzel state, and Wenzel's equation predicts a lower apparent contact angle for a rough surface (i.e. $\theta^* < \theta$) if the material is not hydrophobic ($\theta < 90°$). This unusual effect is indicative of being in the Cassie-Baxter state. However, this Cassie-Baxter state for

the as-spun mats is metastable: the contact angle decreases gradually with time over a period of about 20 minutes under ambient conditions. The origin of this decrease in contact angle is believed to be due to two effects. The first is the evaporation of water from the droplet, which changes the contact angle from advancing to receding. The second is conversion of the contact zone from an initial Cassie-Baxter state to a final Wenzel state as the water droplet sinks into the interstices of the mat. The formation initially of a Cassie-Baxter state, wherein the droplet sits on a heterogeneous surface of fiber and air, could be a consequence of trapping the air when the droplet is first placed gently on such a fibrous mat. The metastable nature of the Cassie-Baxter state in this case can also be demonstrated by applying pressure to the droplet or by allowing the droplet to fall freely from an elevated height to contact with the mat. Dropping the beads of water onto the mat from a height of 8 cm, we observed contact angles for these same as-spun mats as low as 10°. This metastable nature of the hydrophobic state is further verified by the fact that the droplet does not slide even when the mat is tilted to 90° due to the pinning effect. Nevertheless, the initial contact angles still provide useful information on surface roughness. Namely, as shown in Figure 5-2, the contact angles for both beaded fibers and bead-free fibers increase as the average fiber diameter decreases. The contact angles for the beaded fibers increase as the bead density increases and the bead size decreases. Therefore, we conclude that the thinner, beaded fibers have higher surface roughness and therefore higher initial contact angles than the thicker, bead-free fibers.

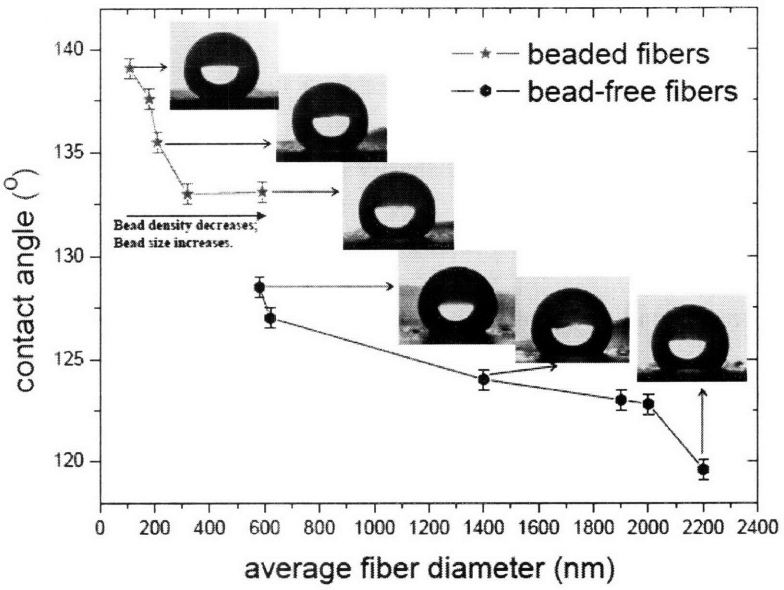

Figure 5-2 The water contact angles for the as-spun PCL mats. From bottom to top in the inset are representative droplet images on Sample F1, Sample F4, Sample F6, Sample B1, Sample B3, and Sample B5. The contact angles are 119°, 124°, 129°, 133°, 135°, and 139°, respectively. The error bars are indicative of statistical variations among multiple measurements; other sources of uncertainty, such as image quality, curve fitting procedures, and operator estimation, suggest that the uncertainty in contact angle determination could be as large as ±3°.

To obtain a stable superhydrophobicity for these electrospun PCL mats, surface modification through iCVD coating is employed. The contact angles for water on all the PPFEMA-coated PCL mats are summarized in Figure 5-3, with selected droplet images shown in the inset. The highest contact angle for the PPFEMA coated mats is larger than 175°. In Figure 5-3, thinner, beaded fibers are observed to give mats with higher contact angles than thicker, bead-free fibers, which is in good agreement with the trend for the as-spun mats. Specifically, for bead-free fibers, mats with smaller fibers are more hydrophobic than those with larger fibers; for beaded fibers, a high density of smaller beads imparts higher hydrophobicity than a low density of larger

beads. Lastly, for the same fiber diameters, the mats with beaded fibers are more hydrophobic than those composed of bead-free fibers. In contrast to the metastable hydrophobicity of the as-spun PCL mats, the superhydrophobicity of the PPFEMA coated mats is stable; a free falling droplet bounces off the surface and splits into smaller droplets instead of spreading on the mat and penetrating into the interstices, as in the case of as-spun mats.

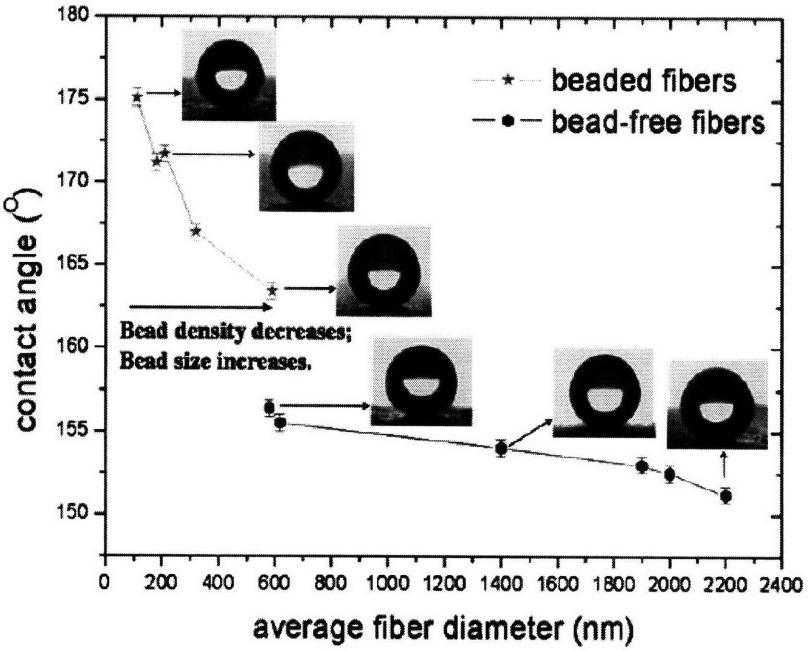

Figure 5-3 Contact angles for PPFEMA-coated PCL mats. From right to left in the inset are representative droplet images on Sample F1, Sample F4, Sample F6, Sample B1, Sample B3, and Sample B5. The corresponding contact angles are 151°, 154°, 156°, 163°, 172°, and 175°, respectively.

As mentioned in Chapter 2, a useful water-repellent surface should have not only a high static contact angle but also a low contact angle hysteresis or threshold sliding angle. Both the hysteresis and sliding angle are important parameters to determine the sliding resistance. Figure 5-4 shows the threshold sliding angles of a 20

mg droplet on the PPFEMA-coated PCL mats with different fiber morphologies. The sliding angle is observed to decrease concurrent with the increase in superhydrophobicity from Sample F1 to F6 and from B1 to B5, confirming the conclusion we made previously from the static contact angle measurements. All the sliding angles shown in Figure 5-4 are less than 12°, again in direct contrast to the as-spun mats, where the droplet does not slide even when the surface is tilted to 90°. The lowest sliding angle is 2.5°, observed for Sample B5, which also has the highest static contact angle at 175°.

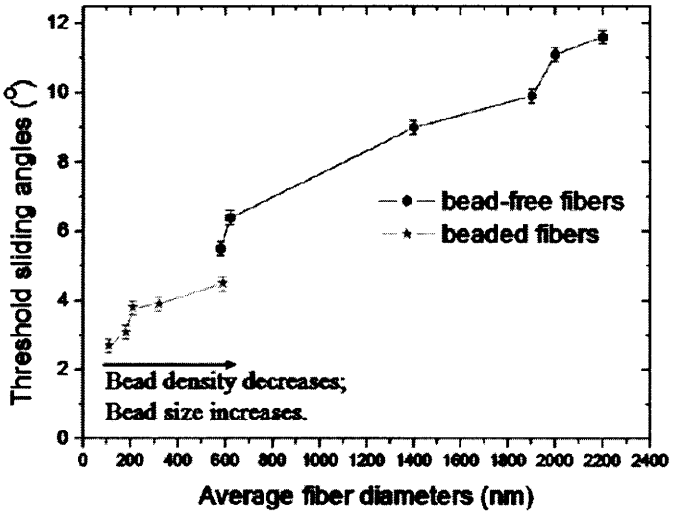

Figure 5-4 Threshold sliding angles for the PPFEMA-coated PCL mats

5.2 Modeling Results

To understand better the effect of fiber morphology on the superhydrophobicity, theoretical studies were performed, based on the Cassie-Baxter equation. For the sake of simplicity, we use parallel cylinders to represent bead-free fibers and

square-packed spheres to represent the beads on the fibers (See Figure 5-5). Figure 5-5 (a) shows cross sectional and top-down views of the water droplet sitting across the fibers, where the bending of the water-fiber interface and the contact area is determined by the intrinsic contact angle, θ, as shown in the figure. Figure 5-6 (b) shows cross sectional and top-down views of the droplet sitting on the tops of beads, where the wetted area enclosed by the dash lines is determined again by the intrinsic contact angle. We have assumed the water can be described by the Cassie Baxter state and thus does not penetrate into the apertures of the mat. This is a valid assumption for the mats employed in this work because the hydrostatic pressure which must be overcome in order for penetration to occur is much larger than atmospheric pressure for micrometer-sized apertures.[54] The contact angle, θ, for PPFEMA is 119°, obtained by measuring the contact angle on the PPFEMA-coated silicon wafer. From this, we calculate the apparent contact angle, θ^*, as a function of $x=d/s$, the ratio of diameter (cylinder or sphere) to separation distance, using the following equations:

$$\cos\theta^* = \frac{x(\pi-\theta)}{x+1}\cos\theta + \frac{x\sin\theta}{x+1} - 1$$

for the case of cylinders and

$$\cos\theta^* = \frac{\pi x^2(1+\cos\theta)}{2(x+1)^2}\cos\theta + \frac{\pi x^2\sin^2\theta}{4(x+1)^2} - 1$$

for the case of spheres. Figure 5-5 (c) shows how these theoretical apparent contact angles for PPFEMA- coated cylinders and spheres vary with d/s. The contact angle decreases as the diameter increases if the separation distance is fixed. Figure 5-5 (c) also shows that the droplet sitting on spheres has a higher contact angle than that sitting on cylinders of comparable radius. Both of the predictions are consistent with

the experimental data. No attempt is made here to fit the data precisely, since the random orientation of fibers in the real materials, as well as the three-dimensional nature of the mats imaged, complicate the determination of an appropriate value for the separation distance between fibers. For beaded fibers, the assumption that the droplet only sits on beads might also break down if the areal bead density is so low that the normal component of surface tension is not sufficient to suspend the droplet only on beads (e.g. see Sample B1). At this point, we hypothesize that if the water sits on both fibers and beads, the contact angle values should fall between the two curves depicted in Figure 5-5 (c). Nevertheless, the simplified model provides useful ranges of contact angles for both bead-free fibers and beaded fibers and all the experimental contact angles roughly fall in these ranges.

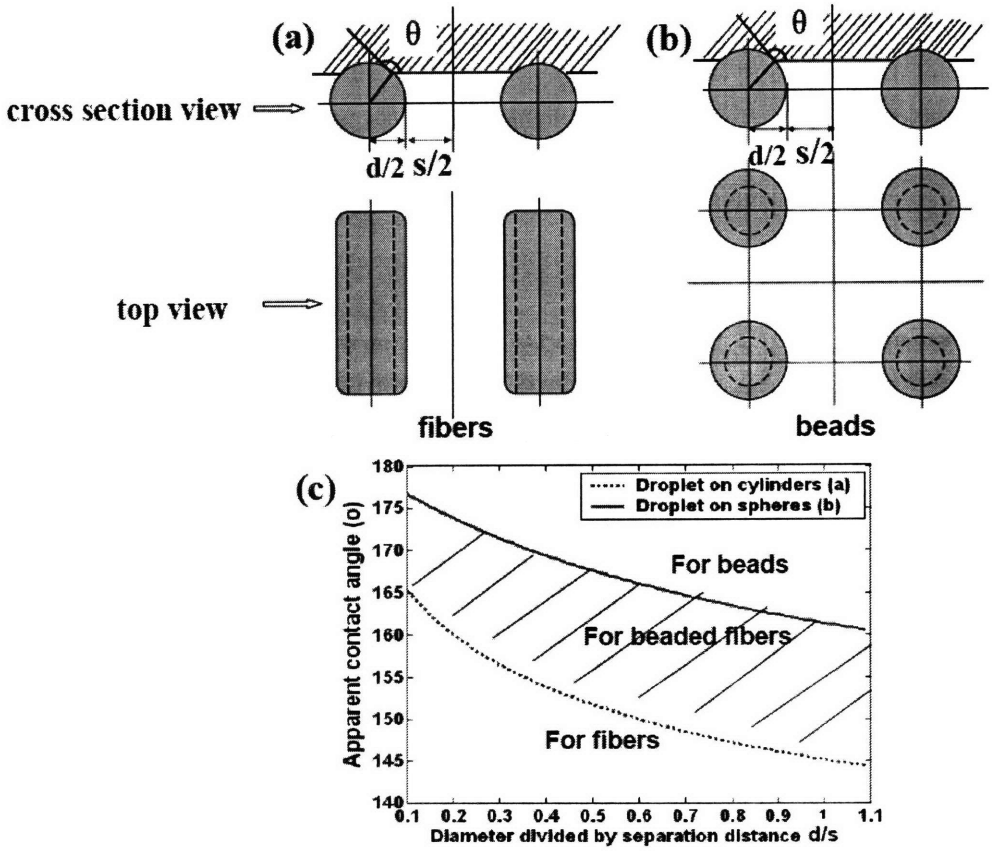

Figure 5-5 Modeling of superhydrophobic property of electrospun fiber mats. (a) and (b), Schematic representations of water droplet sitting on (a) cylinders and (b) spheres. The shaded area represents water and the dashed lines represent triphasic contact lines. (c), Corresponding apparent contact angles for (a) and (b).

The metastable Cassie-Baxter state for water droplets on as-spun PCL mats or alkane droplets on PPFEMA coated mats can be explained and further analyzed based on the geometrical model developed above.[41] For electrospun fibers or simply cylinders, as shown in Figure 5-5 (a), as θ decreases, the air-liquid-solid contact lines moves progressively downwards until some point where Young's angle is satisfied locally at the three phase contact line; the penetration depth of the liquid-air interface into the interstices increases as well. Figure 5-6 shows such a situation where $0° < \theta < 90°$ and a composite interface on the fibers is formed, with the drop sitting partially on air. This is in contrast to other common patterned surfaces, e.g. arrays of vertical posts, which can only form a composite interface and satisfy the Young equation when $\theta > 90°$. An important implication of the so-called "reentrant curvature"[41] associated with the fibers is that one can have $\theta^* >> 90°$ even with $\theta < 90°$ due to the Cassie-Baxter state (composite interface) formed on the fiber mat. This Cassie-Baxter state is only locally stable as the total energy of the system decreases appreciably if the liquid advances and completely covers the fibers, leading to a Wenzel state. However, in order for the transition from Cassie state to Wenzel state to occur, an energy barrier must be overcome. If the barrier is sufficiently high, then it is possible to make a superhydrophobic (superoleophobic) surface from a hydrophilic (oleophilic) material. Another important implication of the model developed above (Figure 5-5) is

that decreasing the *d/s* value increases the apparent contact angles (θ^*), i.e. fibers with relatively small diameter and large separation distance are favored for superhydrophobicity. However, low *d/s* value causes sagging of the liquid-air interface as shown in Figure 5-6.[41] This sagging may lead to wetting of next level of fibers and therefore decreases the robustness of the metastable Cassie state or the superhydrophobic property. The robustness was quantified recently by Tuteja *et al.*,[41] as a ratio of h_1 and h_2: $H^* = h_1/h_2 = 2(1-\cos\theta)dl_{cap}/s^2$, where θ is the intrinsic contact angle for the liquid with a smooth film of the same material as the fibers and $l_{cap} = (\gamma_{lv}/\rho g)^{1/2}$ is the capillary length, γ_{lv} is the vapor-liquid interfacial tension, ρ is the liquid density and g is the gravitational constant of acceleration. Figure 5-7 (a) shows how the apparent contact angle (θ^*) and robustness (H^*) change with the intrinsic contact angle (θ) for a model mat with given structures (d = 1 μm and s = 10 μm), while Figure 5-7 (b) shows how they vary with separation distance (s) for a given surface chemistry (θ = 119°) and fiber size (d =1 μm). It is clear that although high apparent contact angles can be achieved with relatively low intrinsic contact angle and high separation distance, the robustness is significantly sacrificed. Similarly, varying the fiber diameter (d) also has competing effects on the apparent contact angles and the stability of the composite interface. Thus, simply lowering *d/s* can not result in a robust superhydrophobicity. One way to enhance the superhydrophobic property of the electrospun fiber mats without sacrificing the robustness is to create additional level of structures on individual fibers. This will be discussed in the next chapter.

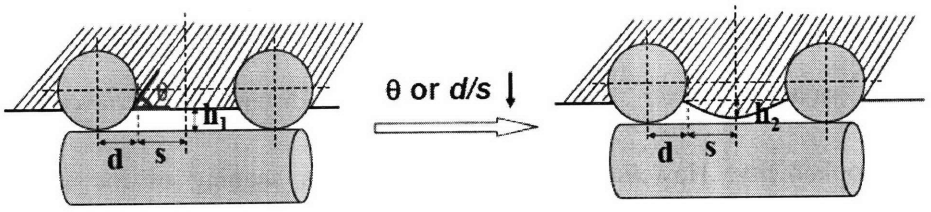

Figure 5-6 Schematic representations of water droplet sitting on fibers. The intrinsic contact angle or characteristic ratio of fiber size to inter-fiber distance may affect the shape of the water-air interface between fibers.[41]

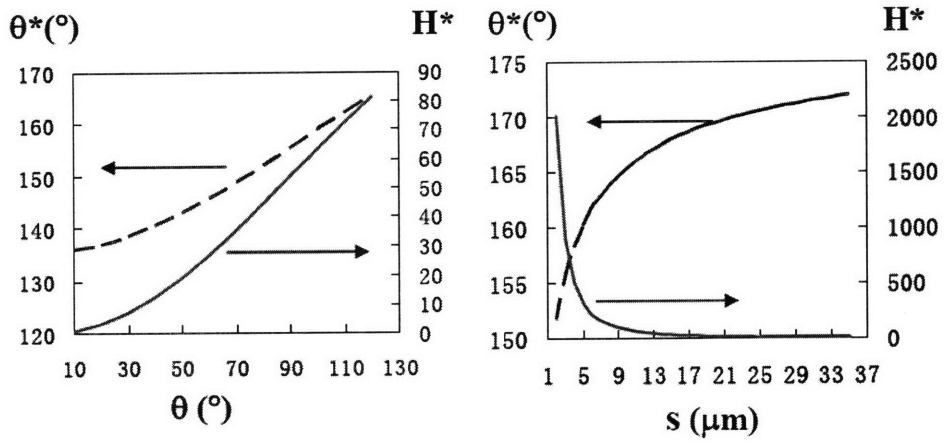

Figure 5-7 A robust superhydrophobic mat requires both high intrinsic contact angle and high density of small fibers. (a), Apparent contact angles and robustness as a function of θ, given d = 1 μm and s = 10 μm; (b), Apparent contact angles and robustness as a function of s, given $\theta = 119°$, d = 1 μm.

Chapter 6 Introducing Hierarchical Roughness to Electrospun Mat to Enhance the Robustness of Its Superhydrophobic Property

6.1 Introduction

Many self-cleaning plants not only excrete a waxy material but also have a clever hierarchical morphological structure with at least two different length scales of roughness on their leaves, typically a nanometer-scale structure decorated on top of a micrometer-scale structure.[55] The best known example of this is the lotus leaf. Inspired and guided by such observations from the natural world, researchers have designed and synthesized various superhydrophobic surfaces with hierarchical surface roughness.[56, 57, 58] These studies clearly reveal that surfaces with hierarchical roughness have higher hydrophobicity than the corresponding surface with only one level (micron scale or nano-scale) of roughness. It has been suggested that the second level of roughness promotes the trapping of air between the water droplet and surface, which in turn helps to prevent water from penetrating the surface. It also increases the tortuosity of the three-phase contact line and reduces the pinning effects.[59,60] The effect of hierarchical roughness can also be explained by the robustness parameter $H^* = 2(1-\cos\theta)dl_{cap}/s^2$, as introduced above. For hierarchically roughened fiber mats, the intrinsic contact angle can be replaced by the effective contact angle θ^* arising from a surface with fine scale roughness but lacking the larger scale topology associated with the curvature of the fiber itself, as indicated in Figure 6-1 and discussed below. Since

$\theta^* > \theta$, it follows that the robustness parameter H^* also increases, suggesting that the hydrophobicity of a hierarchically roughened mat is generally more robust than that of a mat with smooth fibers.

Introducing micro-particles into an electrospun fiber mat generally improves the hydrophobicity, but the main problem associated with a fiber/particle hybrid membrane is that it is not robust mechanically; under deformation and wear conditions, the disconnected particle component is readily lost from the membrane. Processing the fibers with a beaded morphology as described above solves the problem of wear, but it remains likely that the enhanced hydrophobicity is due to the introduction of beads rather than fibers as points of contact with the water drop. One way to improve the hydrophobicity of electrospun fiber mats without sacrificing the robustness (decreasing *d/s* value) or introducing micro-particles (beads) is to make hierarchically roughened fiber mats, where finer-scale structures (e.g. nanometer scale particles or pores) are decorated on a coarser-scale structure associated with the fibers.[61]

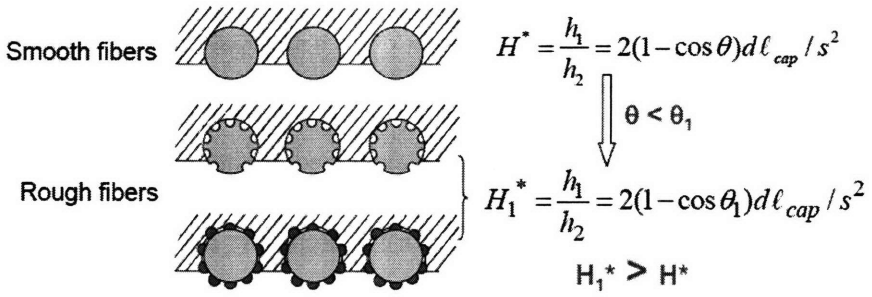

Figure 6-1 Schematic representations of water droplet sitting on smooth fibers and rough fibers, and corresponding robustness parameters. The hatched region represents a portion of the liquid water droplet lying on the fibers, indicating the different natures of the composite interfaces between water and fibers. For smooth fibers, the liquid penetrates the mesh to a depth that satisfies the intrinsic contact angle; the

apparent surface is a composite of the curved solid/liquid and vapor/liquid interfaces. For fibers with nanometer scale pores, the liquid penetrates the mesh to a depth that most closely approximates the intrinsic contact angle with the fiber outer surface; the fiber surface itself becomes a composite of solid/liquid and vapor/liquid interfaces. For fibers coated with nanoparticles, the liquid penetrates both the mesh and the inter-particle spaces such that the intrinsic contact angle is realized at all 3-phase contact lines; the apparent fiber surface becomes a composite of curved solid/liquid (on particles) and vapor/liquid interfaces. The significance of the re-entrant geometry of the fibrous surface is illustrated here using a solid-liquid contact angle less than 90° in all three schematics.

6.2 Introducing Nanopore Structures to Electrospun Fibers

The first approach to create hierarchical surface roughness for electrospun fiber mats is to introduce nanometer scale pores on surfaces of micrometer scale fibers. The pore structures were created by electrospinning from solutions in a highly volatile solvent under conditions with relatively high (~ 45% or higher) humidity. To demonstrate the concept, several polymer/solvent combinations have been used, including poly(carbonate) (PC)/dichloromethane (CH_2Cl_2), PS/CH_2Cl_2, PCL/CH_2Cl_2, (Figure 6-2) and poly(methyl methacrylate) (PMMA)/$CHCl_3$. (Figure 6-3a) The formation of pore structures on the fiber surfaces has been attributed to two mechanisms: rapid phase separation and breath figure formation during the electrospinning process. [62,63] Whether one or both of these mechanisms are actually operative in the case discussed here is not certain and requires further work to clarify. However, the moisture in the air plays an important role in the formation of pores. For example, electrospinning the same PMMA/$CHCl_3$ solutions in a relatively dry environment (22% relative humidity achieved by setting up the apparatus in a modified oven with insulated walls and venting holes and purging the oven with dry

nitrogen for 2 h prior to spinning) did not give pore structures. In some cases, the fibers show collapsed structures with noncircular cross sections. The phenomena have been attributed to the formation of polymer skin on the liquid jet during electrospinning.[64] After the skin forms, the solvent in the interior of the jet escapes and the tube formed by the skin is collapsed by the atmospheric pressure into flat or elliptical fiber.

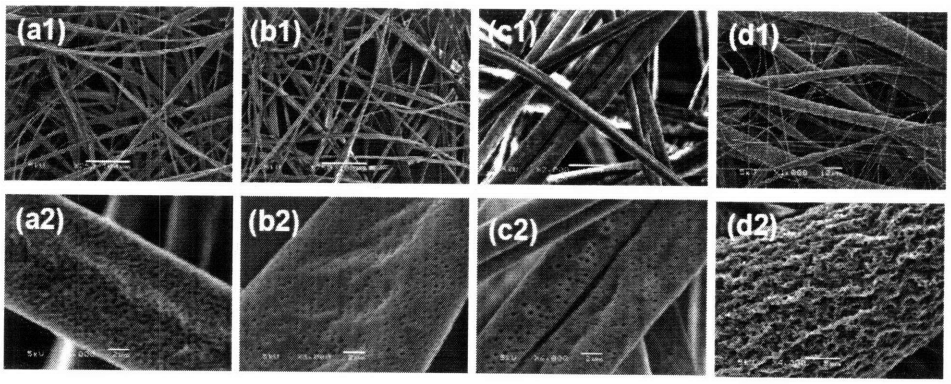

Figure 6-2 SEM images of fibers with nanopore structures made from different materials. (a) Poly(carbonate) fibers made from its 15 wt% solution in CH_2Cl_2; (b) Low molecular weight (280 kDa) PS fibers made from its 20 wt% solution in CH_2Cl_2; (c) High molecular weight (2000 kDa) PS fibers made from its 7.2 wt% solution; (d) PCL fibers made from its 10 wt% solution in CH_2Cl_2.

To explore the effect of surface pore structures on hydrophobic property of electrospun fibers, PMMA fibers with an average fiber diameter of 1.7 μm with and without surface pore structures were made by electrospinning from a 6.8 wt% solution in $CHCl_3$ and a 15 wt% solution in DMF, respectively. The flow rate, plate-to-plate distance, and voltage were set, respectively, to 0.05 mL/min, 50 cm, and 18.0 kV for the PMMA/$CHCl_3$ solution and 0.03 mL/min, 45 cm, and 21.8 kV for the PMMA/DMF solution. To increase the solution conductivity and make thin fibers, a small amount (about 0.1 wt%) of an organic salt, tetrabutylammonium chloride

(TBAC, Fluka), was added to both solutions. The two types of PMMA fibers have similar fiber size and fiber size distribution. The only remarkable difference between them is that one has smooth fiber surface and the other has pore structures on the surface with average pore size of approximately 80 nm. Therefore, the difference for their wettability discussed as following is mostly due to the pore structures.

The initial average contact angle on the PMAA mat with fiber surface pores, recorded within 30s after placing droplets on the mat, is 147°. This angle is slightly higher than the value of 144° obtained for the mat without surface pores. Both of these contact angles were unstable and decreased to about 74° and 71°, respectively, as the droplets evaporated under ambient conditions over a period of 25 minutes. This decreasing contact angle with increasing time for the as-spun mat is indicative of an unstable initial hydrophobic state and has been studied systematically for textured surfaces of SU-8 photoresist by McHale *et al.*[65] The decrease of contact angle as the droplet evaporates and the contact line recedes provides a reasonable estimate for the contact angle hysteresis.

To decrease the surface energy of the fiber mats, a thin conformal PPFEMA coating (30nm on the reference silicon wafer) was applied using initiated chemical vapor deposition (iCVD) as described previously. In Chapter 4, XPS data confirmed the PPFEMA surface coatings on the fibers, while SEM showed that the topology of the electrospun mat was not significantly altered. In this work, the surface pores on the fibers and the overall appearance remained after the coating, as shown by the SEM images in Figure 6-3 (c) and (d). The average contact angle increased to 163°

(inset in Figure 6-3c) for the fiber mat with surface pores, which is again slightly higher than the value of 158° (inset in Figure 6-3d) observed for the fiber mat without surface pores. These two angles changed to 160° and 151° respectively after 25 minutes under ambient conditions, indicating that the PPFEMA-coated mat with surface pores had not only a higher contact angle but also a lower hysteresis than the mat without surface pores. A comparable increase in contact angle of a (non-superhydrophobic) electrospun mat associated with the introduction of porosity within the fibers by precipitation in a cryogenic fluid was reported recently by McCann *et al.*[66] In both instances, the enhancement of hydrophobicity associated with the introduction of pores is modest. Nevertheless, the approach of introducing pore structures on electrospun fibers has the practical advantage of achieving hierarchically roughened fabrics in a single process step.

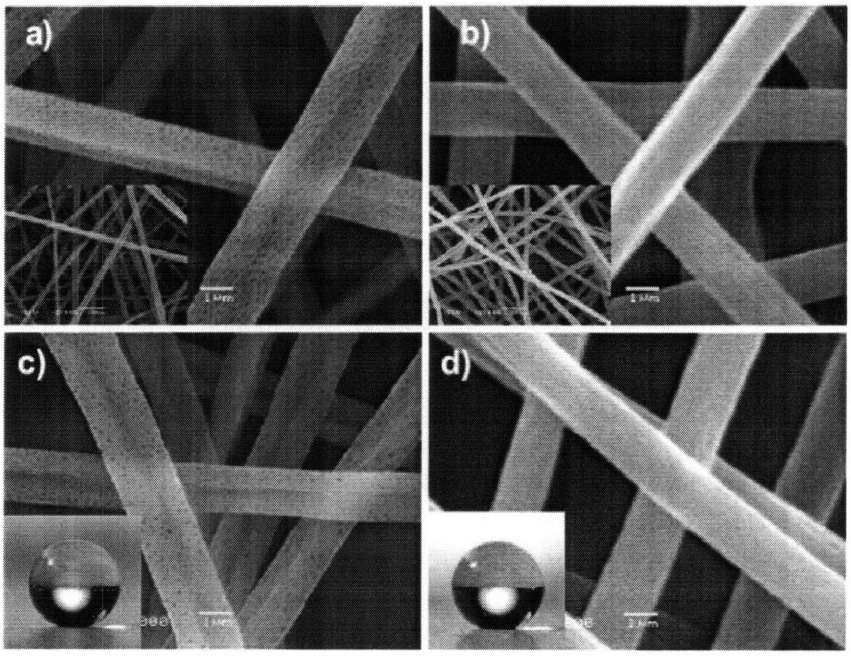

Figure 6-3 Electrospun mat with nanopore structure exhibiting enhanced superhydrophobic property. (a) and (b), SEM images of as-spun PMMA fibers with

and without surface pore structures; scale bars: 1 μm and 10 μm (insets). (c) and (d), SEM images of PPFEMA coated fibers and corresponding droplet images (insets); scale bars: 1 μm.

On a related note, electrospun fibers with surface pore structures can also be made by a template method. Nanoparticles suspensions are blended with a polymer and made into fibers. Porous fibers are obtained after removing the nanoparticles from the fibers using a selective solvent. For example, a poly(ethylene oxide) (PEO) was added into PS nanoparticle aqueous suspensions and electrospun into fibers. The PS nanoparticles were selectively removed using THF. Figure 6-4 shows the SEM images of the fibers before and after the removal of the nanoparticles. High molecular weight PEO fibers normally have relatively small fiber sizes. To increase the fiber size, poly(ethylene glycol) (PEG) can be further added to the PEO and PS nanoparticle solution. (Figure 6-4c)

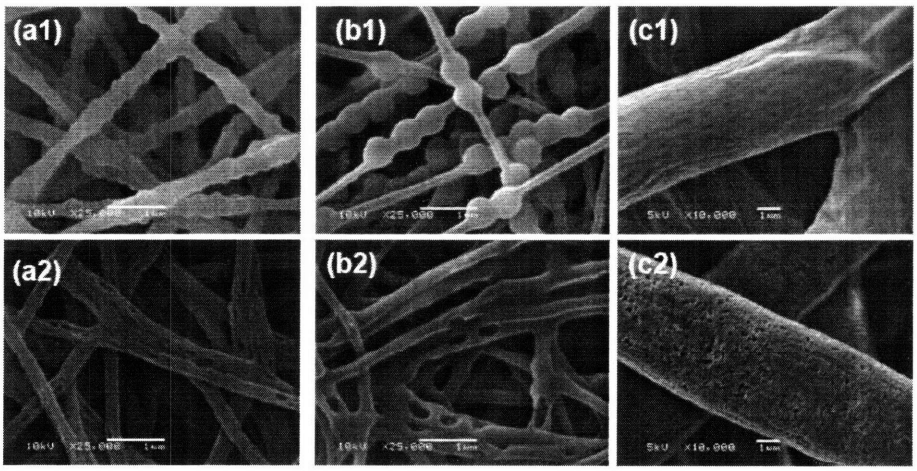

Figure 6-4 SEM images of polymer/nanoparticles composite fibers and porous fibers made by removing the nanoparticles. The fibers were made from aqueous solutions of (a) 1.4 wt% PEO (1500 kDa) and 0.8 wt% PS nanoparticles (200 nm diameter); (b) 1.1 wt% PEO (1500 kDa) and 1.2 wt% PS nanoparticles (500 nm diameter); (c) 0.93 wt% PEO (1250 kDa), 26.4 wt% PEG (10 kDa) and 2.7 wt% PS nanoparticles (130 nm diameter).

6.3 Introducing Nanoparticles to Electrospun Fibers

The second approach to create hierarchical surface roughness for electrospun fiber mats is to coat the electrospun fibers with nanoparticles. In this approach, hierarchically roughened superhydrophobic fabrics were obtained by coating electrospun fibers with silica nanoparticles using the layer-by-layer (LBL) self-assembly technique and then depositing a semifluorinated silane on to the surfaces. Hierarchically roughened electrospun fibers coated with colloidal gold particles have been shown previously by Li *et al.* [67] The LBL process, a well-known technique to fabricate conformal thin film coatings with molecular level control over film chemistry and thickness, [68] has been used previously to construct superhydrophobic coatings on thin films and silicon wafers.[69] Zhai *et al.*[56] used LBL to prepare a superhydrophobic surface by forming a honeycomb-like polyelectrolyte multilayer film, followed by coating with silica nanoparticles and post-treatment with a semifluorinated silane. LBL is capable of conformally coating complex geometries and has been applied to electrospun fibers for sensor applications,[70] but not for the purpose of demonstrating hierarchical roughness. Here, an electrospun Nylon mat with a uniform fiber diameter of about 1.7 μm was coated with positively charged poly(allylamine hydrochloride) (PAH) and negatively charged 50 nm silica nanoparticles using the LBL self-assembly technique as described in the experimental chapter. The Nylon-6 fiber mat is the same as the one used for dip-coating or iCVD

coating described in Chapter 4. The surface-exposed silica nanoparticles on the LBL treated fiber mats were then reacted with a low surface energy species, (tridecafluoro-1,1,2,2-tetrahydrooctyl)-1-trichlorosilane ($(CF_3)(CF_2)_5(CH_2)_2SiCl_3$) using a vapor phase deposition. Smooth glass surfaces covered with the silane alone and coated with two layers of silica nanoparticles and the silane exhibit contact angles of 110° and 113°, respectively.

The fiber appearances before and after silica nanoparticle and trichlorosilane treatment are shown in Figure 6-5 (a) and (b), respectively. It is clear that the as-spun fibers have smooth surfaces that are noticeably altered by the nanoparticle coatings. Figure 6-5 (b) also indicates that the layer-by-layer coating as well as the subsequent vapor-deposited fluorinated silane layer is thin and conformal. The higher magnification SEM images (See Figure 6-5 (c) and (d) for as-spun and treated fibers, respectively) confirm the nanometer scale surface roughness of the treated fibers. The nanoparticle coating was verified further by comparing the AFM phase images of the as-spun fibers and treated fibers as shown in the insets of Figure 6-5 (c) and (d), respectively. An exceptionally smooth surface with no visible surface features was observed for a representative region of the as-spun fibers, while for treated fibers a high density of nanoparticles was clearly seen.

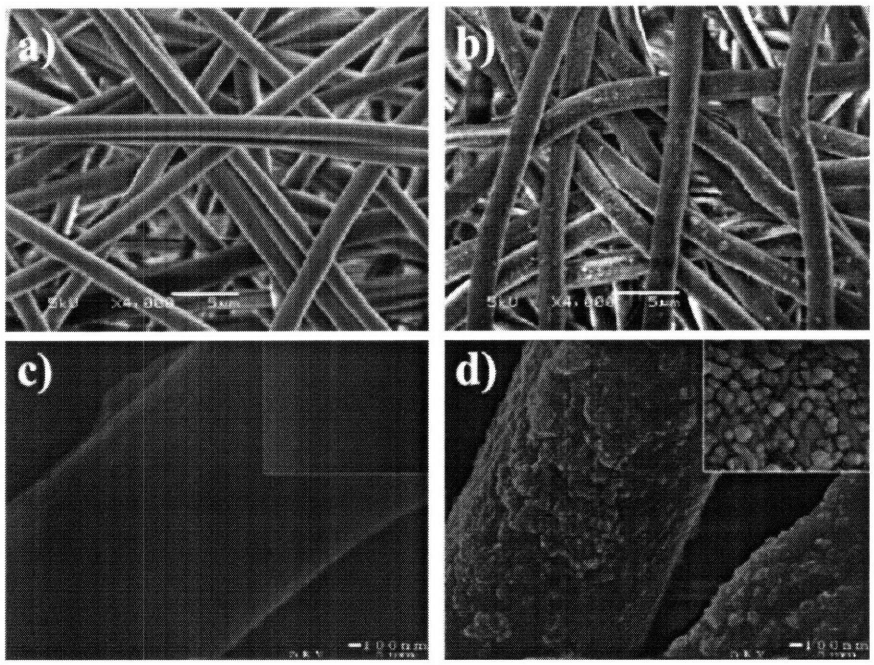

Figure 6-5 Comparison of surface structure of smooth and nanoparticle-decorated electrospun Nylon fibers. (a) and (c), As-spun fibers; (b) and (d), Treated fibers. The insets in (c) and (d) show AFM phase images of representative area (1000 nm×800 nm) on the surfaces of the as-spun and treated fibers, respectively.

The surface chemistry of the Nylon fibers before and after treatment was analyzed by using XPS, as shown in Figure 6-6 (a) and (b), respectively. Figure 6-6 (a) shows that the as-spun mat does not contain any characteristic fluorine (680-690 eV for F1s) or silicon peaks (150 eV for Si2s), as expected. Figure 6-6 (b) shows significant peaks characteristic of fluorine and silicon but no detectable peaks for nitrogen contained in the Nylon and PAH components of the treated sample, indicating that the coverage of silica nanoparticles and the polymerized fluorosilane coating on the fiber surfaces is complete.

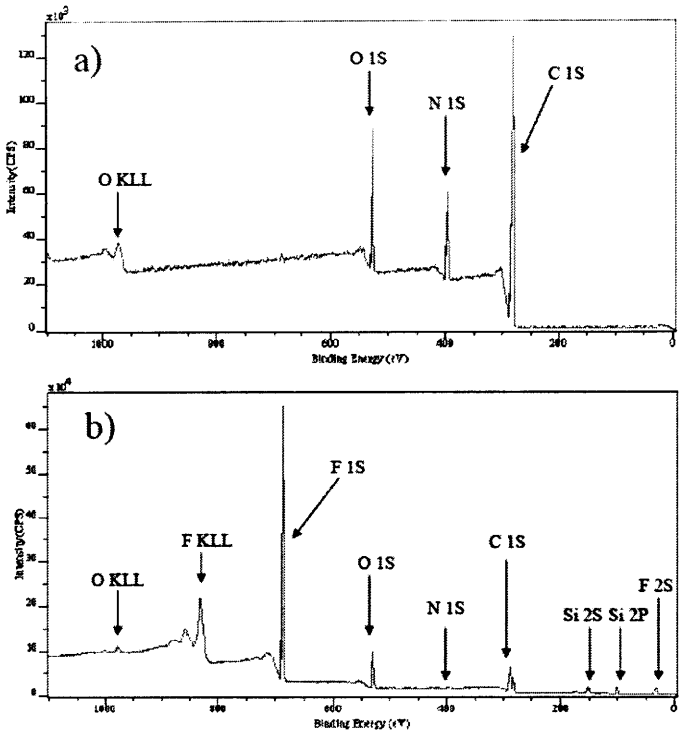

Figure 6-6 Comparison of surface chemistry of as-spun Nylon fibers and treated fibers. (a), XPS data of as-spun Nylon fibers; (b), XPS data of treated Nylon fibers. The peaks corresponding to each element are labeled.

Water contact angle measurements on both as-spun and treated Nylon fibers are shown in Figure 6-7. The as-spun fiber mat exhibited an initial contact angle of 135°. This value is significantly higher than the advancing contact angle of 69° measured for a smooth, solvent cast Nylon film, and is due to a metastable Cassie state in which air is trapped in the interfibrillar space. As the droplet evaporated under ambient condition for about 25 minutes on the as-spun mat, the contact angle changed to a receding value of 60°. In contrast, the initial average contact angle for the treated fiber mat was 168°. This contact angle did not change as the droplet evaporated, indicating a stable superhydrophobicity with almost zero contact angle hysteresis. The effect of the silica nanoparticles in enhancing the hydrophobicity is further evidenced by the

fact that the Nylon fiber mat coated with this fluorosilane alone under same experimental condition only has contact angle of 142°and hyteresis of 14°.

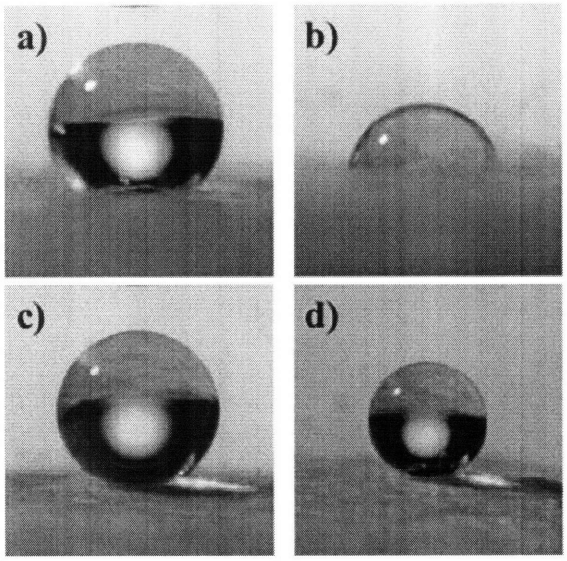

Figure 6-7 Electrospun mat decorated with nanoparticles exhibiting enhanced superhydrophobic property. (a) and (c), Images of water droplets on as-spun and modified Nylon fiber mats immediately after deposition; (b) and (d), Images of the same droplets shown in (a) and (c) respectively captured 25 minutes later.

The generality of the LBL approach to make robust superhydrophobic mats is further demonstrated by using a hydrophilic substrate material, poly(acrylonitrile) (PAN). A smooth PAN film has a contact angle of about 37°, while an electrospun PAN mat gets wetted immediately due to the capillary suction. The silica nanoparticle coating followed by the trichlorosilane reaction transformed the highly hydrophilic mat into a superhydrophobic one with almost zero hysteresis. (Figure 6-8)

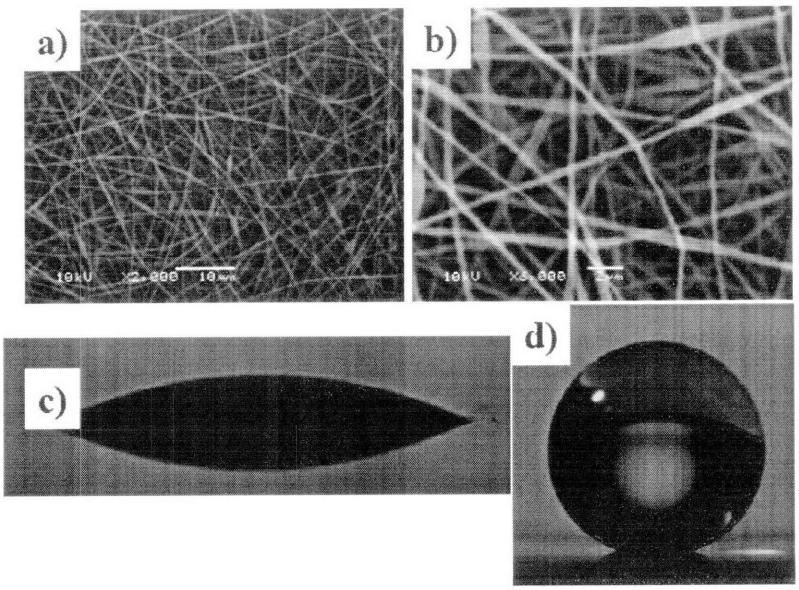

Figure 6-8 Another example of nanoparticle-decorated electrospun mat exhibiting enhanced superhydrophobic property. (a) and (b), SEM images of as-spun PAN fiber mats. (c) and (d), Water droplets on as-spun and treated PAN fiber mats, respectively.

Chapter 7 Conclusions and Recommendations

7.1 Conclusions

The first part of this dissertation mainly describes the author's work on superhydrophobic property of electrospun materials. The most important contributions of this work include the discovery of electrospun fiber mats having appropriate surface roughness for superhydrophobicity, the understanding of the role of fiber morphology on superhydrophobic property and multiple ways to enhance the robustness based on the understanding. As a versatile method to make ultrafine fibers, electrospinning, combined with other nanotechnology such as chemical vapor deposition and layer-by-layer deposition, is shown to not only produce highly robust superhydrophobic surfaces but also have the potential to bring multifunctionalities into such surfaces (See Appendices). The superhydrophobic surfaces composed of electrospun fibers have numerous advantages over the conventional superhydrophobic surfaces. Examples include their breathability, flexibility, free-standing, light weight and robustness of metastable Cassie states. Specifically, the following conclusions can be made.

1. Electrospun fibers represent an example of re-entrant structure. Electrospun fiber mats have sufficient surface roughness for superhydrophobic property.
2. Superhydrophobic fabrics can be made by either electrospinning a relatively hydrophobic material or applying hydrophobic coating on a pre-formed fiber mat.

3. Hydrophobicity was demonstrated to increase monotonically with a reduction in diameter among bead-free fibers within the range between 600 nm to 2.2 μm, and with the introduction of a high density of relatively small diameter beads.
4. Superhydrophobic mats with enhanced robustness can be obtained by decorating electrospun fibers with nanometer scale pore structures or particles on the fiber surfaces.
5. Other functionalities such as anisotropy, structural color, transparency and fluorescence can be incorporated into superhydrophobic surfaces based on electrospinning or electrospraying (See Appendix II)

7.2 Recommendations for Future Work

Superhydrophobicity is a very useful material property. Superhydrophobic surface composed of electrospun fibers is particularly interesting as mentioned above. There are still many research opportunities in the area of superhydrophobic properties of electrospun materials. Based on the author's experience and the work that has been done, the following recommendations are made.

1. A systematic study on the wetting behavior of micro/nano fibrous materials is not only scientifically interesting but also provides insights in designing such materials for various applications including filtration, textiles and biomedical uses. However, such a study is currently not available. The versatility of electrospinning technique provides a good opportunity for this study. For example, the same materials, when processed into fibers with different sizes and morphologies, may

have totally different wetting behavior including Wenzel state, Cassie state or imbibition.[71,72] In addition, how the fiber size distribution affects the wettability of electrospun mats remains unresolved.

2. The robustness of the superhydrophobic property of electrospun mats has not been systematically explored. Careful studies on droplet evaporation or droplet impacting on the mat may lead to better understanding of the robustness.
3. It is well-known that many plant leaves in the nature are water-repellent and self-cleaning. Some undesirable plants such as gorse (Ulex europeaus) introduced into New Zealand, and many common yard weeds have waxy leaf surfaces that make wetting them with water-based herbicides very difficult. The trisiloxane superwetters [73] were developed for their remarkable ability to wet such hard-to-wet surfaces and enhance herbicide efficacy. It is therefore extremely useful to study how the superwetter solutions wet a superhydrophobic surface especially with a fibrous structure such as an electrospun fiber mat. A plot of contact angles as a function of superwetter concentration (surface tension), similar to the Zisman plot ($\cos \theta^*$ vs. γ) that determines the critical surface tension to completely wet the surface, is a good starting point for this study.
4. It is desirable in many real applications to have a surface that can reversibly switch between hydrophobic state and hydrophilic state upon the application of an external stimulus. Thus, reversible control of the wetting property of electrospun materials is an interesting topic. There are a few different methods to make mats with switchable wettability. The first one is to use a thermally sensitive polymer

such as poly (*N*-isopropylacrylamide) (PNIPAM). This polymer has a lower critical solution temperature (LCST) of about 33 °C. A smooth surface of this material has been shown to have contact angles of 63° at 25 °C due to the intermolecular hydrogen bonding at this temperature and 93° at 40 °C due to the intramolecular hydrogen bonding.[74] Processing this material into electrospun fibers can amplify its wettability and in principle can result in superhydrophobic or superhydrophilic mats depending on the temperature. Electrospun fibers have been successfully made as shown in Figure 7-1. However, the wettability of the mat at different temperatures has not been systematically tested. Varying the fiber size and morphology is also worth doing in the future.

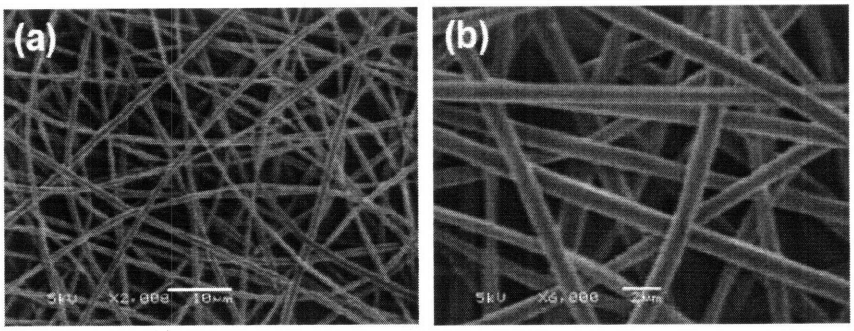

Figure 7-1 SEM images of poly(*N*-isopropylacrylamide) electrospun fiber mat. The fibers were made from a 16 wt% solution of a Mw = 300 kDa PNIPAM in acetonitrile/H2O (4/1 by volume).

The second method to make a switchable mat is to apply a conducting polymer coating on an electrospun mat. A switchable mat may be obtained in two different ways based on electrospun mats coated with conducting polymers. The first way is to coat the mat with a low surface energy material and then use electrowetting to achieve the switchability.[75] The second way is to use a low

surface energy dopant (e.g. tetrabutylammonium perfluorooctane-sulfonate) in the monomer (e.g. pyrrole) polymerization and then take advantage of electrochemical redox reaction of conducting polymers to get switchability. Electrowetting is generally not reversible, while the redox reaction has been demonstrated to cause reversible conversion of conducting polymer films from superhydrophobic to superhydrophilic.[76]

Besides the two methods introduced above, reversibly switchable mats may also be obtained using shape memory materials and photo-sensitive materials.[77]

Part II

Block Copolymers in Electrospun Fibers

Chapter 8 Introduction to Block Copolymers

8.1 Block Copolymers in Bulk

Block copolymers are macromolecules composed of blocks of chemically distinct and thermodynamically incompatible monomers.[78,79,80] Figure 8-1 (a) schematically illustrates the molecular architectures for a diblock and a triblock copolymers. Due to their connectivity, phase separation of the incompatible blocks at a macroscopic level is prevented. Instead, the phase separation occurs at a microscopic level, a process termed as microphase separation. In the bulk, the extent of phase segregation of a diblock copolymer is dictated by a dimensionless parameter, χP. Here, χ is the Flory-Huggins interaction parameter which signifies the incompatibility of the monomers and has a temperature dependence approximately as $\chi \approx \alpha/T + \beta$. P is the total degree of polymerization, which is related to the entropic penalty associated with chain stretching upon microphase separation. If either χ or P is sufficiently high, the enthalpic (demixing) effect will dominate, leading to a compositionally ordered phase. The transition from a homogeneous melt of polymer chains to ordered phases is called order-disorder transition (ODT). The type of ordered phase that is formed for $\chi P > (\chi P)_{ODT}$ depends further on the volume fraction of each block, f, which determines the curvature of the interface between blocks. The phase behavior for a diblock copolymer in bulk can thus be summarized in phase diagrams parameterized by χP and f. Figure 8-1 (b) shows a self-consistent field

phase diagram for a conformationally symmetric diblock copolymer, where the statistical segment length of the two blocks are equal. Depending on the χP and f, various periodic microphase separated structures are formed, such as close-packed spheres (CPS), bcc packed spheres, hexagonally packed cylinders, bicontinuous cubic double gyroid and lamellae (Figure 8-1c)

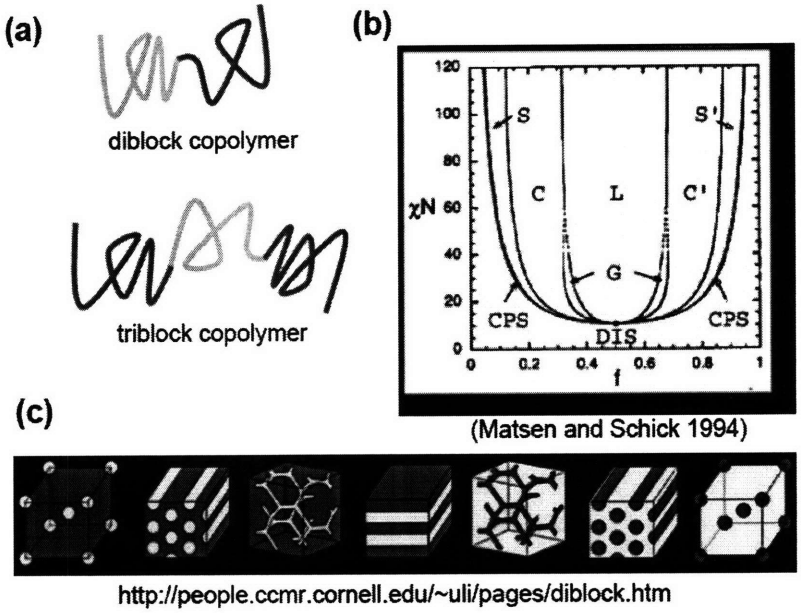

Figure 8-1 A introduction to block copolymer in bulk. (a), A schematic illustration of the molecules of a diblock copolymer and a triblock copolymer; (b), A calculated phase diagram for a diblock copolymer in bulk; (c), A schematic illustration of the different morphologies.

It has been suggested that there exist three different regimes for the composition profile of ordered phase structures of diblock copolymers in bulk depending on the incompatibility: the weak segregation limit (WSL, $\chi P \sim \chi P_{ODT} \sim 10$), the intermediate segregation limit ($10 < \chi P < 100$) and the strong segregation limit (SSL, $\chi P > 100$). (Figure 8-2) In WSL, due to their weak repulsion, the interface between different blocks is wide and the composition profile is approximately

sinusoidal with the domain period scaling as $L_0 \sim R_g \sim P^{1/2}$. In SSL, however, the interface is much narrower with a width of $\sim a\chi^{-1/2}$, where a is the statistical segmental length. Due to the sharp interface in SSL, a simple balance between the localized interfacial energy and entropic loss due to chain stretching under the constraint of incompressibility has been used to predict the domain period that scales as $L_0 \sim aP^{2/3}\chi^{1/6}$.

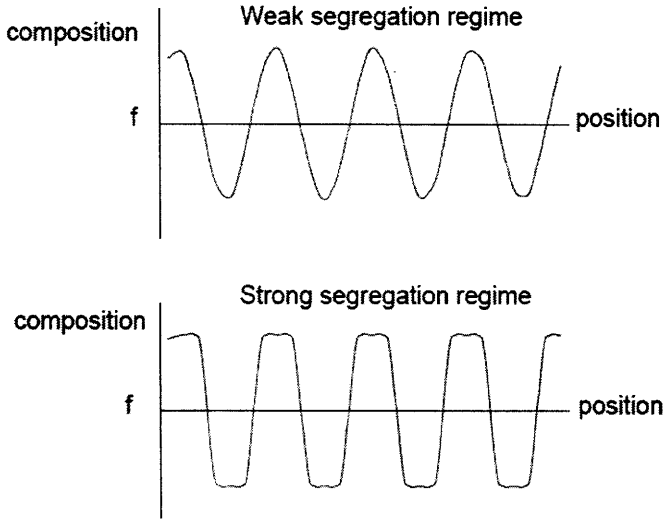

Figure 8-2 Composition profiles for weakly segregated and strongly segregated block copolymers in bulk.

Block copolymers are not only very interesting from the scientific point of view but also extremely useful materials. For example, in solid state they are used as thermoplastic elastomers and in areas such as impact modification, compatibilization and pressure-sensitive adhesion. In addition, their ability to form a wide variety of ordered morphologies with periodicity typically in the range of 10-100 nm, dimensions that are hard to achieve by conventional, top-down technologies such as photolithography, has made block copolymers very attractive in nanotechnologies.[81,82]

For example, Figure 8-3 schematically shows some applications for block copolymers in nanotechnologies. Many of the applications such as templates are based on block copolymer thin films which will be reviewed briefly next.

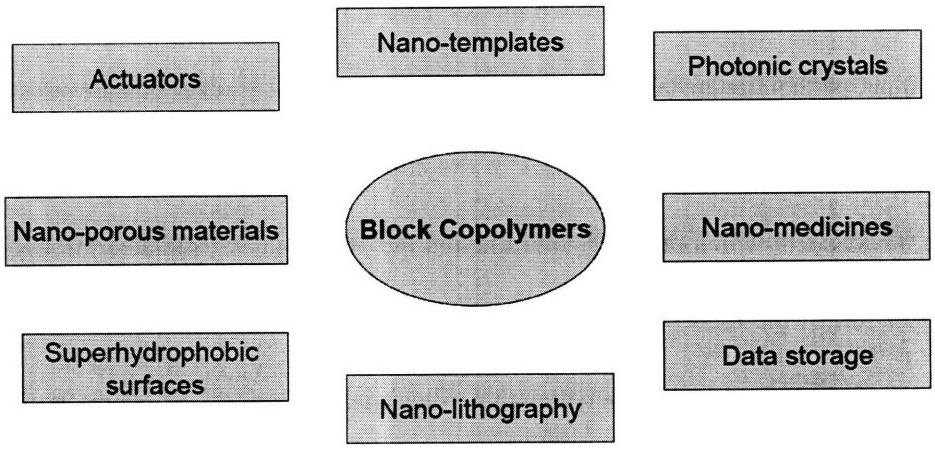

Figure 8-3 A Schematic illustration for different applications of block copolymers in nanotechnologies.

8.2 Block Copolymer Thin Films

In block copolymer thin films, the confinement effects and boundary conditions are sufficient to alter the phase behavior, making it significantly different from bulk.[83] For example, for supported film of symmetric lamella-forming diblock copolymers, when there is a sufficiently high preference of one block to the substrate, free surface or both, the lamellae will orientate parallel to the substrate to minimize the interfacial energy. The period of the block copolymer in the parallel orientated lamellae is normally equal to the bulk value. However, if the initial film thickness (t) is not quantized as $t = nL_0/2$, holes or islands with step height of L_0 may form on the free surface to maintain bulk chain dimensions.[84] Replacing the free surface with another rigid substrate suppresses the surface topography and forces the copolymer to change

the period to accommodate the incommensurate film thickness.[85,86] In this case, it has been shown that the period deviated from the bulk in a cyclic manner as a function of the confined film thickness, and the deviation decreased as the film thickness increased. In the case where the two blocks have similar preference to the surface or substrate, perpendicular lamellae may form with the period always equal to the bulk value.[87] Given the specific properties of the copolymer and substrates, the range of film thickness in which one orientation favors the other can be estimated through the comparison of the total free energy for respective orientation. In SSL, the total free energy of confined block copolymer thin films mainly consists of chain stretching energy, interfacial energy between blocks and interfacial energy between the copolymer and the substrates. The phase behavior of block copolymer thin films discussed above can be simply summarized in Figure 8-4. In addition, external fields such as flow fields[88] or electrical fields[89] and lithographically defined templates[90,91] can be used to direct the block copolymer self-assembly in thin films to achieve long range order.

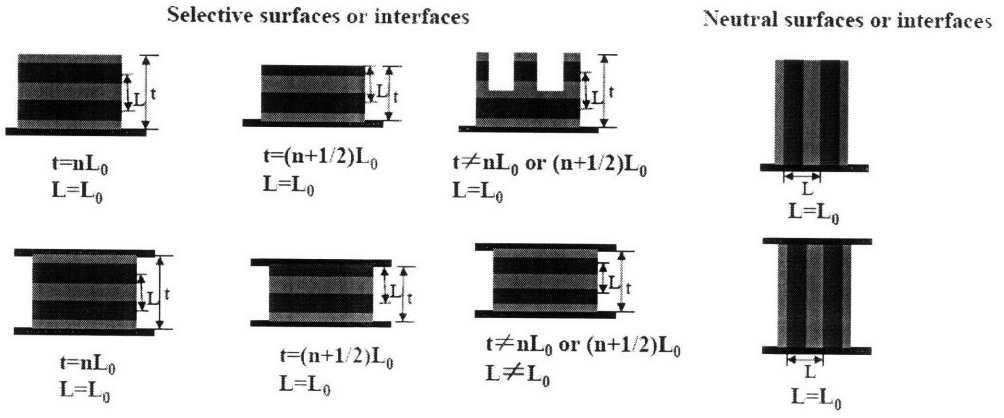

Figure 8-4 A schematic illustration for thin films of symmetric block copolymers

supported on one substrate or confined between two substrates.

8.3 Block Copolymers under Curved Confinement

Entirely novel structures have been found to arise when block copolymers are confined in geometries with curved walls of dimensions up to an order of magnitude larger than the bulk period (L_0) of the copolymer.[92,93] Early experimental studies on block copolymers under curved confinement were performed more than a decade ago by Reffner and Thomas.[94] They processed block copolymer systems into spherical microparticles by an aerosol technique and studied the morphology of the block copolymers or their blends with homopolymers under spherical confinement. Lamella- and cylinder-forming block copolymers were found to exhibit a concentric packing of microdomains into "shells", while sphere-forming block copolymers formed disordered arrays of spheres inside the microparticles. The morphology of spherically confined block copolymers was also studied recently by other researchers[95,96,97,98] The concentric-sphere morphology observed in these studies was first predicted using Monte Carlo simulation by He *et al.* [99] Now various morphologies of spherically confined block copolymers have been obtained by simulations.[100,101]

Another type of curved confinement is cylindrical confinement which has been stimulating tremendous interest among both experimentalists[102,103,104,105,106] and theoreticians. [107,108,109,110,111,112,113,114] For the theoretical work, many methods have been used to study the block copolymers confined in cylindrical nanopores, including Monte Carlo simulations, dynamical density functional simulations, self consistent

field theory (SCFT) calculations and dissipative particle dynamics (DPD) simulations. A range of morphologies have been identified: concentric lamellae, i.e. lamellae parallel to the pore axis; stacked disks, i.e., lamellae perpendicular to the pore axis; porous lamellae (meshes); single and double helices. Among the experimental work, Russell and co-workers published a series of papers to report different morphologies formed by lamella-, cylinder- and sphere-forming block copolymers confined in nanoporous alumina membranes. They found the lamella-forming symmetric poly(styrene-*b*-butadiene) (PS-PBD) diblock copolymers formed concentric lamellar morphology in relatively large pores and a novel toroidal morphology in relatively small and incommensurate pores. For cylinder-forming PS-PBD, they observed non-hexagonally packed cylindrical domains with cylinder axes aligned along the pore axis in relatively large pores and helical morphology in relatively small pores. For sphere-forming PS-PBD, they observed spherical microdomains aligned along the pore axis in large pores and helical arrays of the spherical microdomains in smaller pores. Similarly, Stucky and coworkers also used the nanoporous alumina membrane to confine block copolymer-like silica-surfactant composite and observed various unusual silica structures such as toroids and helices.

8.4 Electrospinning of Block Copolymers

All these previous studies on the cylindrically confined block copolymer as reviewed above demonstrated that cylindrical confinement can lead to novel self-assembled structures that are not accessible in the bulk. These structures are of

particular interest in areas such as optics and drug delivery. However, all the previous work for producing these materials, including that by Russell *et al.*, Stucky *et al.* and others, is to use the capillary sorption into porous alumina membrane. This fabrication method significantly limits the potential applications of such materials because it is extremely slow and produces only very short "nanorods" (~5 μm in length). In contrast, electrospun block copolymer fibers, which are of comparable diameter with the nanorods and therefore represent another novel sample geometry as cylindrical confinement, are continuous and can be produced at a much higher rate (on the order of 0.1 gram, or 10^6 meters, of fiber per hour per spinneret). One motivation for electrospinning of block copolymers is thus to make novel block copolymer structures in the form of continuous fibers. In addition, to realize fully the applications of those novel structures, as for nanostructures of block copolymer thin films or bulk in general, understanding and control of the domain sizes is essential.[115] A quantitative study on the effect of cylindrical confinement on the lamella-forming block copolymers will be provided in this dissertation.

Although electrospun fibers offer a novel and robust platform in which the self-assembly of block copolymers can be induced under extreme cylindrical confinement, the time scale of the fiber formation process itself does not permit the organization of blocks into an ordered morphology in situ. Intensive post-spin annealing of the fibers is hindered by loss of the cylindrical fiber geometry when the fibers are held above the glass transition temperatures or melting temperatures of the blocks. One way to overcome this problem, as will be demonstrated in this

dissertation,[116] is to use a two-fluid coaxial electrospinning technique where the block copolymer is processed as the core component and encapsulated in a second, shell polymer that has a high glass transition temperature (T_g). Subsequent annealing of the fibers above the upper T_g of the block copolymer but below the T_g of the shell polymer results in self-assembly of the block copolymer under cylindrical confinement. Further removal of the shell polymer results in block copolymer fibers.

Chapter 9 Experimental Methods

9.1 Fabrication of Electrospun Block Copolymer Fibers

The electrospinning was conducted on the same device as that described in Chapter 3. Block copolymer fibers can be made by choosing appropriate molecular weight of the copolymer, solvent and concentration using a single-fluid electrospinning. However, in most cases in this dissertation, block copolymers were processed into core-shell fibers using a two-fluid electrospinning method. The two-fluid electrospinning device is based on previous design by Jian Yu.[117] It is very similar to the single-fluid device. The only difference is the capillary arrangement at the upper disk. Instead of having just one capillary, the two-fluid electrospinning device has two capillaries, one inside of the other, forming an annulus. The inner capillary (Upchurch® # 1145) has an inner diameter of 0.45 mm and an outer diameter of 0.79 mm, whereas the outer capillary (Upchurch® # U-825) has an inner diameter of 0.08 inch (2.032 mm) and an outer diameter of 1/8 inch (3.175 mm). A stainless steel 1/8" Tee union (Ohio Valley # SS-200-3) connects two separate Teflon® tubes to the capillaries, one to the inner capillary and one to the outer capillary. Two syringe pumps deliver two separate fluids to the capillaries simultaneously, a block copolymer solution as the inner fluid and a higher T_g polymer solution as the shell fluid. Figure 9-1 illustrates the strategy of the two-fluid electrospinning for the encapsulation of block copolymer in core-shell fibers.

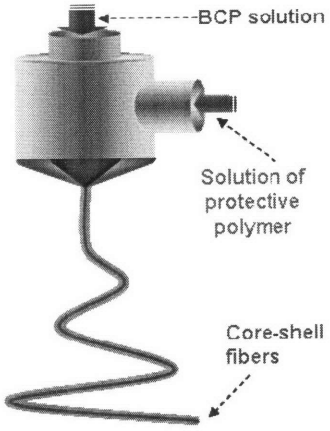

Figure 9-1 Schematic for the two-fluid core-shell electrospinning spinneret by which block copolymer is encapsulated into core-shell fibers.

The annealing of the fibers was performed in a vacuum oven at specified temperature. The two temperatures predominantly used in this study were 140 °C and 160 °C. The annealing time, unless otherwise specified, was set at 10 days.

9.2 Block Copolymers, Solution Compositions and Operating Parameters

All the block copolymers that will be described in following chapters in this dissertation are listed in Table 9-1. The PS-PDMS block copolymers were provided by Dow Corning Corp.; the V4111, V4211 and V4411 PS-PI-PS block copolymers were provided by Dexco Polymers; other block copolymers were purchased from Polymer Source Inc.

abbreviation	block copolymer	Mw (kDa)	Composition (by volume)	PDI	Morphology
PS-PDMS/PS	Poly(styrene-*b*-dimethylsiloxane)*	266	45% PS	1.12	-
PS-PI	Poly(styrene-*b*-isoprene)	830	38% PS	1.15	-
V4111	Poly(styrene-*b*-isoprene-*b*-styrene)	128	15.8% PS	1.11	Cylinder
V4411	Poly(styrene-*b*-isoprene-*b*-styrene)	62	41% PS	-	Lamella
PS-PDMS-L1	Poly(styrene-*b*-dimethylsiloxane)	93.4	55% PS	1.04	Lamella
PS-PDMS-L2	Poly(styrene-*b*-dimethylsiloxane)	46.4	50% PS	1.08	Lamella

PS-PI-S1	poly(styrene-*b*-isoprene)	85	83% PS	1.05	Sphere
PS-PI-S2	Poly(styrene-*b*-isoprene)	91	75% PS	1.05	Sphere
V4211	Poly(styrene-*b*-isoprene-*b*-styrene)	102	26% PS	-	Cylinder
PS-PDMS-G1	Poly(styrene-*b*-dimethylsiloxane)	75.4	58.5% PS	1.04	Gyroid
PS-PDMS-G2	Poly(styrene-*b*-dimethylsiloxane)	136.1	58.9% PS	1.09	Gyroid

* This block copolymer also contains 23.4 wt% homopolymer PS (Mw = 127 kDa).

Table 9-1 Different block copolymers used in this study.

For single-fluid electrospinning of block copolymer fibers, the solution composition and operating parameters are summarized in Table 9-2.

block copolymer	solvent	concentration	Voltage (kV)	Flow rate (ml/min)	Plate-to-plate distance (cm)
PS-PDMS/PS	THF/DMF (3/1 by volume)	21%	30	0.05	50
PS-PI	THF/DMF (3/1 by volume)	3.7%	22.1	0.04	43
V4111	THF/DMF (3/1 by volume)	15%	20.4	0.04	45

Table 9-2 Solution concentrations and operating parameters for the single-fluid electrospinning of different block copolymers.

For two-fluid electrospinning, the compositions of core and shell solutions and operating parameters are summarized in Table 9-3. The polymers used in the shell solutions are poly(methyl methacrylate) (PMMA), poly(methyl methacrylate-*co*-methacrylic acid) random copolymer (denoted as P(MMA-*r*-MAA); weight ratio MMA/MAA=20/80) and poly(methacrylic acid) (PMAA).

Block copolymer	Solutions		voltage (kV)	plate-to plate distance (cm)	flow rates (ml/min)	
	core	Shell			Shell	Core
V4111	13.5 wt% in CHCl3/DMF (3/1)*	13.5 wt% PMMA in CHCl3/DMF (3/1)	28	48	0.08	0.01

V4411	18 wt% in CHCl3/DMF (3/1)	P(MMA-*r*-MAA) 21 wt% in DMF	31.6	45	0.05	0.005
PS-PDMS-L1	15 wt% in CHCl3/DMF (3/1)	21 wt % PMAA in DMF	33	45	0.045	0.005
PS-PDMS-L2	18 wt% in CHCl3/DMF (3/1)	21 wt % PMAA in DMF	35	50	0.05	0.004
PS-PI-S1	18 wt% in CHCl3/DMF (3/1)	P(MMA-*r*-MAA) 18 wt% in DMF	30	45	0.05	0.005
PS-PI-S2	16 wt% in CHCl3/DMF (3/1)	P(MMA-*r*-MAA) 20 wt% in DMF	32	45	0.05	0.006
V4211	15 wt% in CHCl3/DMF (3/1)	P(MMA-*r*-MAA) 19 wt% in DMF	30.5	45	0.06	0.005
PS-PDMS-G1	13 wt% in CHCl3/DMF (3/1)	PMAA 22 wt% in DMF	35	45	0.04	0.005
PS-PDMS-G2	7 wt% in CHCl3/DMF (3/1)	PMAA 22 wt% in DMF	38	45	0.06	0.003

* The solvent ratio is by volume.

Table 9-3 Solution concentrations and operating parameters for the two-fluid electrospinning of different block copolymers.

9.3 Characterization of Block Copolymer Fibers

The general feature of the fibers was again observed by SEM, as described in Chapter 3. The internal nanostructures of the block copolymer core-shell electrospun fibers were characterized mainly by transmission electron microscope (TEM). For axial views, the annealed fibers were first embedded in epoxy resin (LR White-Medium Grade, Ladd Research) and cryo-microtomed into ~70 nm thick sections. (Figure 9-2) The cutting temperature was set at -160 °C, lower than the T_g of PS (105 °C), PI (-70 °C) or PDMS (-120 °C), to minimize any distortions of microphases during the microtoming. The cross sections were then examined using a JEOL JEM200 CX (JEOL Ltd, Japan) transmission electron microscope (TEM) operated at an accelerating voltage of 200 kV. For longitudinal views, the fibers were

deposited on TEM grids directly and examined after annealing. For polystyrene (PS) and polyisoprene (PI) block copolymers, osmium tetraoxide (OsO_4) was used as the staining agent to selectively stain PI microdomains. For PS-PDMS block copolymers, since the electron density of the PDMS block is sufficiently high to provide the necessary contrast over the PS block, no staining was needed.

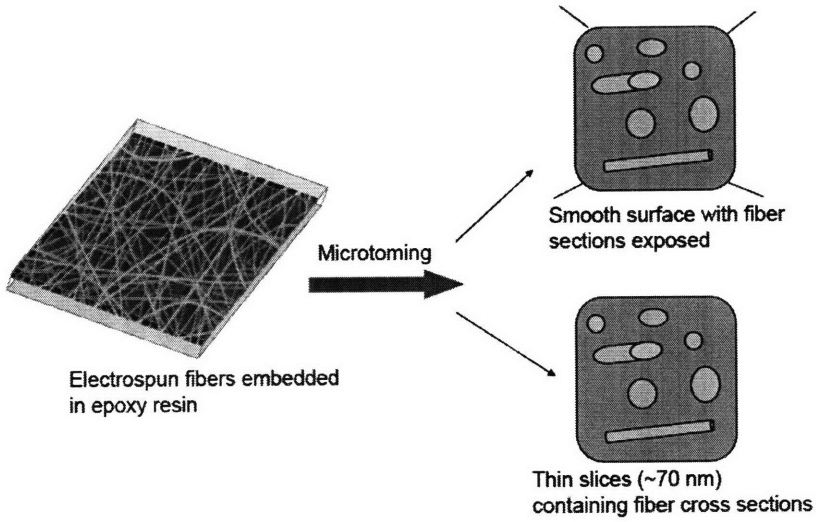

Figure 9-2 Characterization of electrospun block copolymer fibers: core-shell structures and block copolymer microphase separated structures. The thin slices are transformed onto TEM grid and imaged by TEM, while the remaining sample with smooth surface can be explored by AFM.

Atomic force microscopy (AFM), small angle X-ray scattering (SAXS) and differential scanning calorimetry (DSC) were also occasionally used to characterize the block copolymer fibers. AFM characterization was done in a similar way as described in Chapter 3 except that the fibers were embedded in epoxy resin and trimmed using microtoming technique (also see Figure 9-2). SAXS data were acquired in-house using a Molecular Metrology SAXS instrument, including a Bede Microsource X-ray Generator with copper target, Osmic Confocal Max-Flux optic,

three pinhole collimation, and a Gabriel-style gas-filled multiwire detector. The relative X-ray intensity at the beam-stop (I_1) was measured using a photodiode. The thermal transitions in the block copolymer fibers were characterized using a Q1000 modulated differential scanning calorimeter (TA Instrument Inc., DE). The measurements were carried out under a nitrogen atmosphere and the sample was scanned for two cycles from -100 to 200 °C with a rate of 10 °C per minute.

Chapter 10 Block Copolymer Electrospun Fibers

This chapter presents the data on the non-equilibrium structures in the block copolymer fibers and preliminary results on the novel strategy to encapsulate block copolymers in core-shell electrospun fibers.

10.1 Block Copolymer Fibers by Single-Fluid Electrospinning

To study the microphase separation of electrospun block copolymer fibers, a PS-PDMS block copolymer blended with PS (PS-PDMS/PS, see Table 9-1 for details) was first chosen. The microphase separated structure for this polymer in bulk is shown in Figure 10-1 (a). The fibers (Figure 10-1 (b), also see Table 9-2 for details) have diameters of 150 nm to 400 nm.

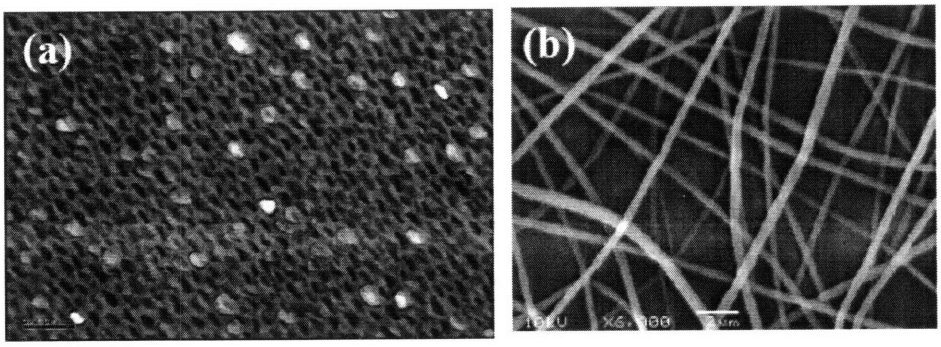

Figure 10-1 PS-PDMS/PS electrospun fibers. (a), TEM image of the PS-PDMS/PS solution-cast film. The scale bar is 200 nm. The dark regions are PDMS blocks and the light regions are PS blocks. The lightest regions are homopolymer PS. (b), SEM images of electrospun fibers made from the PS-PDMS/PS sample.

The microphase separation in the PS-PDMS/PS fibers was first evidenced by the glass transition temperature T_g of 105°C exhibited in the DSC curve in Figure 10-2. This transition temperature is characteristic of unblended PS. The glass transition of

PDMS is -125°C. The rule of mixtures[118] would predict a glass transition of about –5°C if the PS and PDMS were well mixed; no such peak is observed here. The endotherm around –40°C during heating is attributed to the crystal melting point of PDMS, while the exotherm around –75°C during cooling could be due to crystallization.

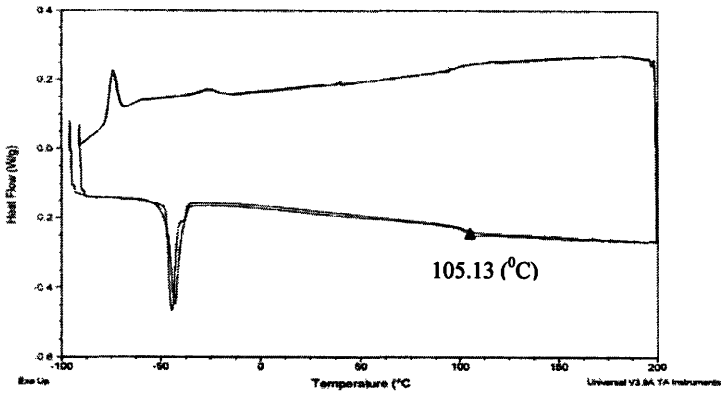

Figure 10-2 DSC curves for the microphase separated PS-PDMS/PS fibers. The top curves are the cooling runs in the first and second cycles and the bottom curves are the heating runs.

The microphase separation was further studied using TEM. In Figure 10-3 (a), the rod-like PDMS microdomains are randomly orientated, giving an appearance of fish scales. As the fiber diameter decreases as shown from Figure 10-3 (b) to (e), the alignment of these PDMS microdomains is significantly improved.

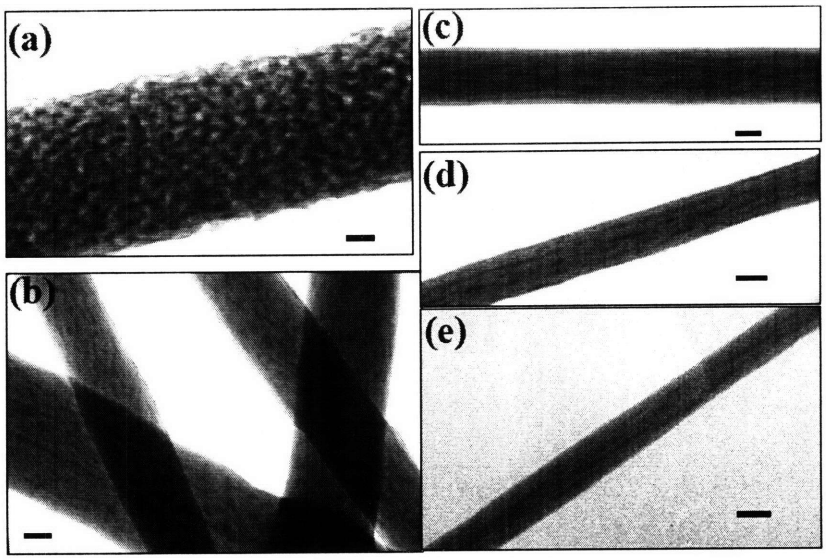

Figure 10-3 Internal nanostructures of electrospun PS-PDMS/PS fibers. Note that in large fibers, the rod-like domains are randomly arranged, while in smaller fibers these domains are aligned along the axis of the fibers. Scale bars: 100 nm.

The microphase separated structures and the improvement of domain alignment with decreasing fiber size were also observed for a PS-PI fibers as shown in Figure 10-4. It is believed the alignment of the block copolymer microdomains inside the fiber is mainly due to the effect of the elongational flow in the fiber-forming process.

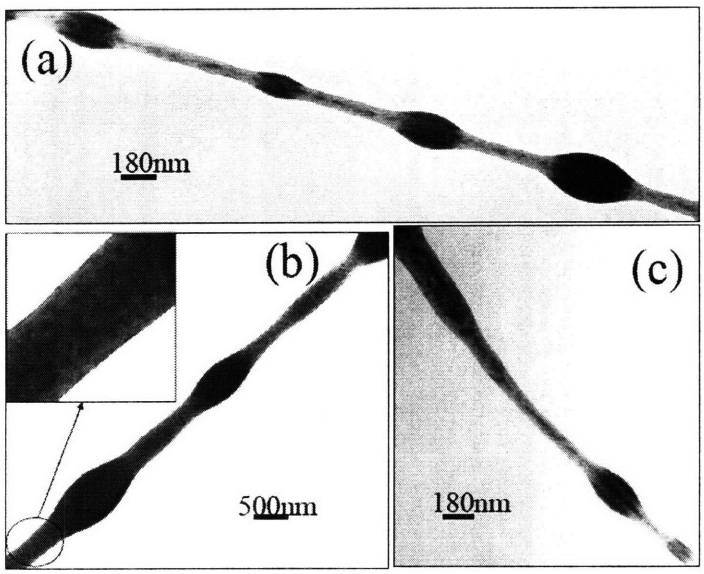

Figure 10-4 Internal nanostructures of electrospun PS-PI fibers. Note the

improvement of the alignment of the microdomains as the fiber size decreases. The isoprene domains were selectively stained with osmium tetraoxide (OsO_4) and thus appear dark, while the unstained styrene domains appear light.

10.2 Encapsulating Block Copolymers Using Co-axial Electrospinning

Although the block copolymer fibers made by single-fluid electrospinning have microphase separated structures, they are far from equilibrium. In order to induce near equilibrium structure by post annealing, a two-fluid co-axial electrospinning technique[119] can be used to encapsulate the desired block copolymer as the core with another, protective polymer as the shell. The two-fluid electrospinning provides at least three significant advantages here. First, being electrospinnable itself the shell fluid serves as a process aid for block copolymers which are otherwise difficult or impossible to electrospin. For example, Figure 10-5 (a) shows SEM image of beaded fibers produced from a PS-PI-PS triblock copolymer (V4111) by a single fluid electrospinning. No uniform fibers could be obtained from this polymer using single-fluid electrospinning. However, the two-fluid electrospinning method allows the production of uniform fibers from V4111. Figure 10-5 (b) shows the PMMA/V4111 core-shell fibers with an average diameter of 5 μm made by the two-fluid electrospinning. The core-shell structure is evidenced by the SEM image of a fractured fiber shown in Figure 10-5 (c). Uniform V4111 fibers with an average diameter of 2.3 μm (Figure 10-5d) were obtained after the removal of PMMA shell using methanol. Second, the shell polymer defines a cylindrical confining geometry and may have a glass or melt transition temperature well in excess of either

component of the block copolymer, thereby creating a temperature window in which the confined block copolymer may be annealed without compromising the integrity of the fiber. For example, the fibers made from a blend of V4111 and high molecular weight (Mw = 400 kDa) PI are uniform (Figure 10-5e) and show ordered structures after annealing at 100 °C for 24 hours evidenced by the SAXS pattern in the inset of Figure 10-5 (f), but the fibers were melted by the annealing as shown by Figure 10-5 (f). In contrast, the PMAA/V4111 core-shell fibers can be annealed at higher temperatures for much longer time without changing the fiber shapes as long as the annealing temperature is lower than the Tg of PMMA (~120 °C). (See Figure 10-6) Preliminary AFM studies (Figure 10-7) have shown that cylindrical microdomains aligned along the fiber axis formed in these annealed core-shell fibers. Third, independent control of the two fluid flow rates permits wider variation in the core fiber diameter, in particular enabling the production of much smaller diameter block copolymer fibers. As will be shown in next chapter, block copolymer fibers with diameter less than 100 nm can be easily made using the two-fluid electrospinning.

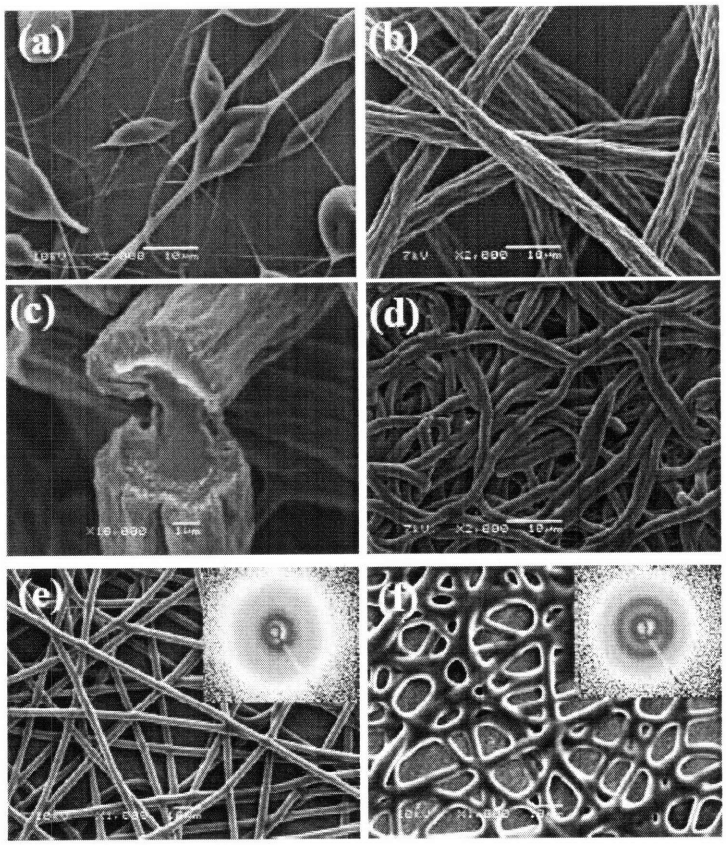

Figure 10-5 Advantages of co-axial electrospinning to make block copolymer fibers. (a), SEM images of V4111 fibers made by single-fluid electrospinning; (b) and (c), PMMA/V4111 core-shell fibers; (d), V4111 fibers after the removal of PMMA; (e)-(f), SEM images of the V4111 fibers before and after annealing. To make uniform fibers from V4111, 1 wt% PI (Mw = 400 kDa) was added to the electrospinning solution. The 2D SAXS patterns in the insets show that the as-spun fibers do not have any order, while the annealed fibers have significant ordering.

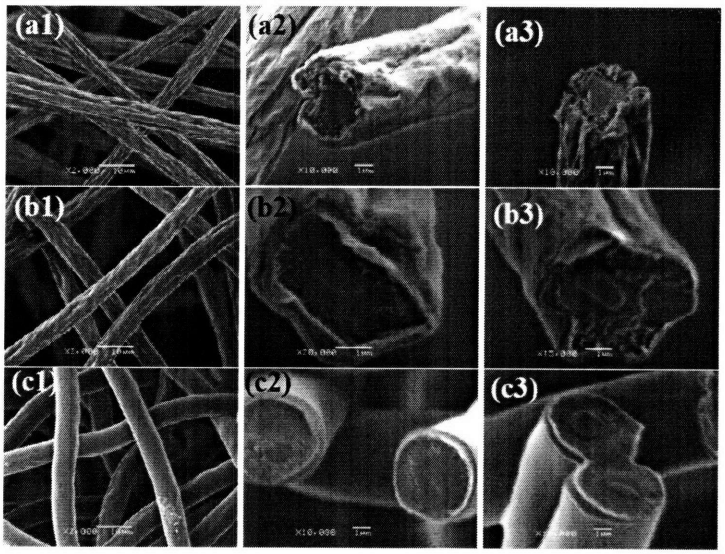

Figure 10-6 SEM images of annealed PMMA/V4111 core-shell fibers. The annealing conditions for (a), (b) and (c) are 105 °C for 13 days, 115 °C for 6 days and 150 °C for 5 hours, respectively. For fibers annealed below the Tg of PMMA (~120 °C), both the fiber appearance and core-shell structure do not change, while those annealed at higher temperatures, the surface of the fibers become smoother and some fibers are welded together.

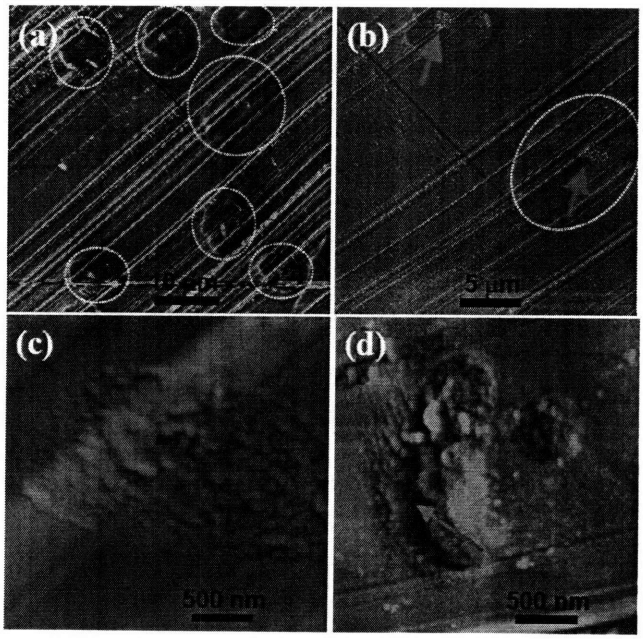

Figure 10-7 Cross sectional AFM images of the PMMA/V4111 core-shell fibers that have been annealed at 115 °C for 6 days. The dashed circles and arrows in (a) and (b) highlight the core-shell structure. The arrow in (d) indicates the aligned cylindrical microdomains.

Chapter 11 Lamella-forming Block Copolymers under Cylindrical Confinement

This chapter describes the morphology of two different types of lamella-forming block copolymers confined in core-shell electrospun fibers and provides a quantitative study on the morphology. Long range order of the morphology will be discussed.

11.1 PS-PI-PS Triblock Copolymer

The first type of lamella-forming block copolymer investigated is a PS-PI-PS triblock copolymer (V4411). It has a molecular weight of Mn ~ 62 kDa, PS volume fraction of 0.41 and forms a lamellar morphology in bulk with an equilibrium long period of 25 nm.[120] Figure 11-1 shows a TEM image of a section microtomed from a thick (~ 1 mm) film cast from a dilute solution in toluene. For the shell material, a thermally stable random copolymer (P(MMA-*r*-MAA)) was chosen. The glass transition temperature of this polymer is 167.5°C as determined by DSC.

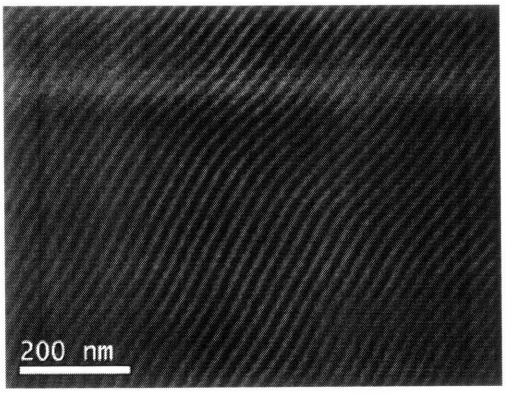

Figure 11-1 A TEM image of the V4411 PS-PI-PS triblock copolymer in bulk. The dark domains are osmium tetraoxide (OsO_4) stained isoprene, while the light domains are unstained styrene.

Figure 11-2 (a) and (b) show SEM images of the as-spun core-shell fibers (see experimental part in Chapter 9 for details). The continuous core-shell nature of these fibers is confirmed by the TEM images in Figure 11-2 (c) and (d). The fibers have diameters ranging from 300 nm to 800 nm with the core sizes varying from 50 nm to 500 nm. The individual V4411 block copolymer core fibers (Figure 11-2 (e) and (f)) were obtained by selective dissolution of the P(MMA-*r*-MAA) shell using methanol.

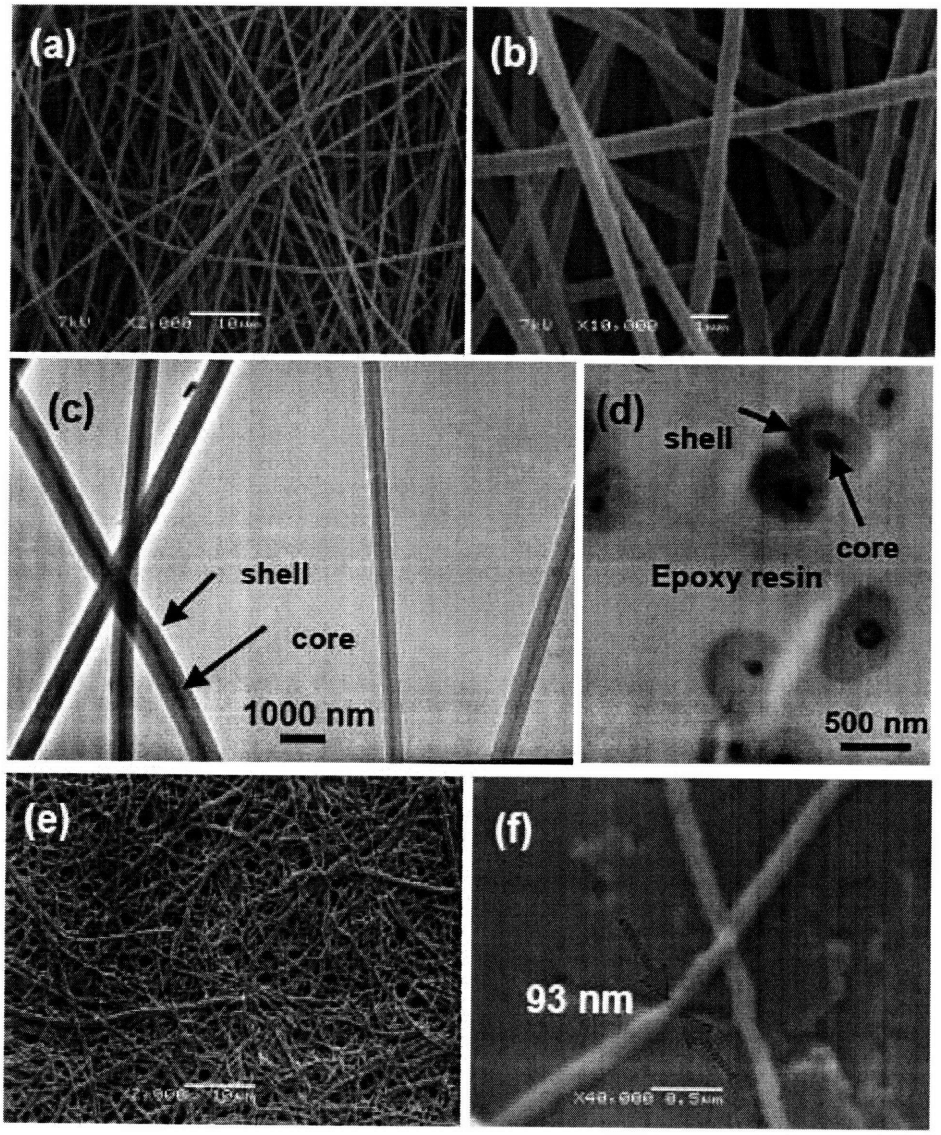

Figure 11-2 Two-fluid co-axial electrospinning of the V4411 PS-PI-PS triblock copolymer. (a) and (b), SEM images of the P(MMA-*r*-MAA)/V4411 core-shell fibers;

(c) and (d), TEM images (longitudinal view and axial view) of the core-shell fibers with V4411 core; the dark cores of the fibers are OsO_4-stained block copolymer and the light parts of the fibers are P(MMA-*r*-MAA) shells; (e) and (f), SEM images of the V4411 nanofibers.

The microphase separation of the block copolymer in the as-spun fibers was observed (see Figure 11-3) but lacked any long range order, similar to the block copolymer fibers made by single-fluid electrospinning as described in the previous chapter.

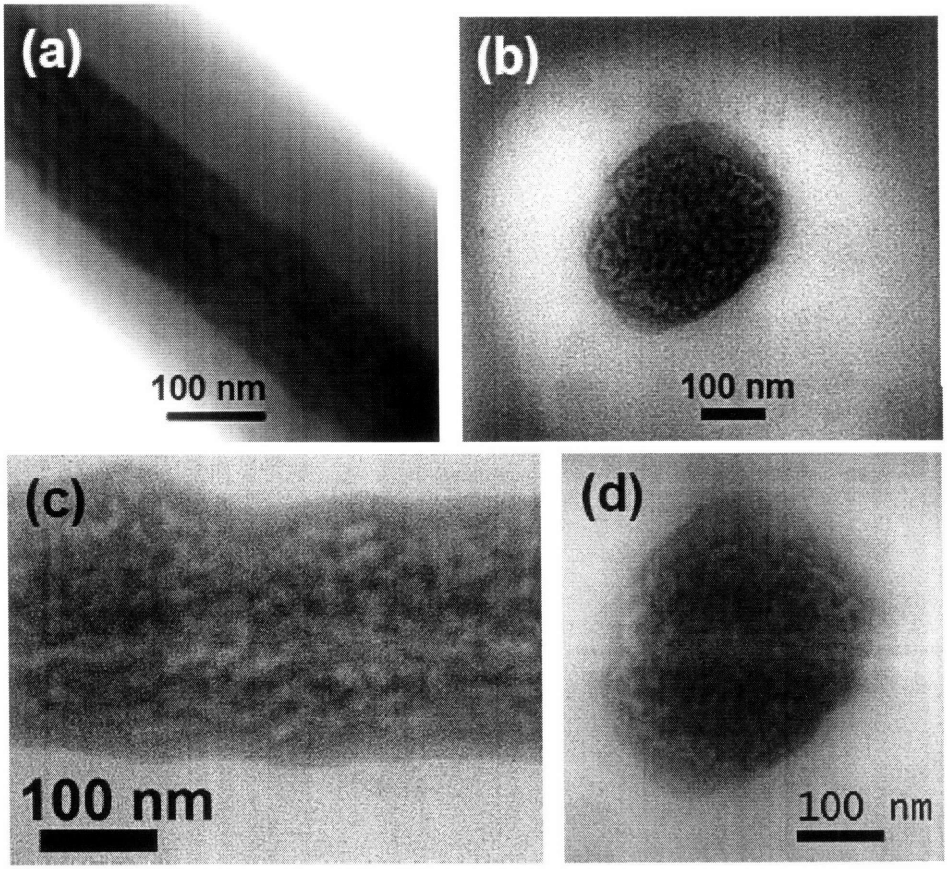

Figure 11-3 TEM images of the V4411 PS-PI-PS core in the as-spun fibers showing the non-equilibrium microphase separation. (a) and (c) are longitudinal views; (b) and (d) are axial views.

To induce long range order, the as-spun fibers were annealed in a vacuum oven at

140 °C for 10 days. The annealing temperature was chosen to be well above the Tg of the styrene and isoprene blocks (~105 °C and ~ -70 °C, respectively) but not to exceed the order-disorder transition temperature of the PS-PI-PS or the onset of thermal degradation of the isoprene block. (Both temperatures are higher than 160 °C.) The fibers remained intact due to the high Tg of the P(MMA-*r*-MAA) shell material. The internal structure of the V4411 core was significantly improved by annealing. Well-defined structures consisting of concentric layers are clearly seen from TEM images in Figure 11-4. The concentric lamellar structures result from the curving of the lamellar phase due to the fiber confinement. The effect of confinement is made evident by the decreasing number of concentric layers as the fiber core size decreases, from 21 in a fiber of core diameter 510 nm (Figure 11-4a) to only 3 in a fiber of core diameter 50 nm (Figure 11-4f). Compared to the equilibrium period (25 nm) of this block copolymer in bulk, the average thickness of a bilayer under confinement in fibers of different diameter varies from 19 nm to 29 nm. The average bilayer thickness is defined as the core diameter (along the shortest dimension if the core is not circular) divided by number of bilayers.

Many fibers display an outermost PI layer that has the same thickness as the interior PI bilayers (Figure 11-4b), contradictory to half thickness that would be expected for PI outmost monolayer. This observation suggests that in these fibers, styrene actually comprises the outermost domain, but it can not be resolved by TEM images due to its low contrast with the surrounding shell. This behavior is consistent with good adhesion between the core and shell regions of these coaxial two fluid

electrospun fibers, since estimates of the relevant χ parameters at 140 °C ($\chi_{PS\text{-}PMMA}$~0.105,. $\chi_{PS\text{-}PMAA}$~0.154,. $\chi_{PI\text{-}PMMA}$~0.382 and. $\chi_{PI\text{-}PMAA}$~0.472) indicate that the styrene would have the preferred interaction with the P(MMA-*r*-MAA) shell. The outermost isoprene domain in some cases appears to be approximately half the thickness of those closer to the fiber axis, consistent with the formation of a PI monolayer at the edge of the fiber core, rather than the bilayers typical of interior domains. PI is usually the outermost monolayer in block copolymer films and particles with free surfaces. This observation may be indicative of debonding between the core and shell components in some fibers during solidification, since the isoprene block has a lower surface tension (~31 mN/m at 20 °C) than the styrene block (~40 mN/m at 20 °C) and would therefore tend to segregate to the free surface in such instances.

Other variations of the domain size along the radial direction as well as under confinement in fibers of different core diameter may be due to the accommodation of the microdomains to the cylindrical confinement to minimize the total free energy. The total free energy in confinement consists of regular bulk free energy terms, and additionally the enthalpic term due to interfacial wetting and the entropic term of chain deformation (stretching or compression) due to the size and curvature constraints. Detailed quantitative analysis in this aspect will be given in next section for PS-PDMS lamella-forming block copolymers.

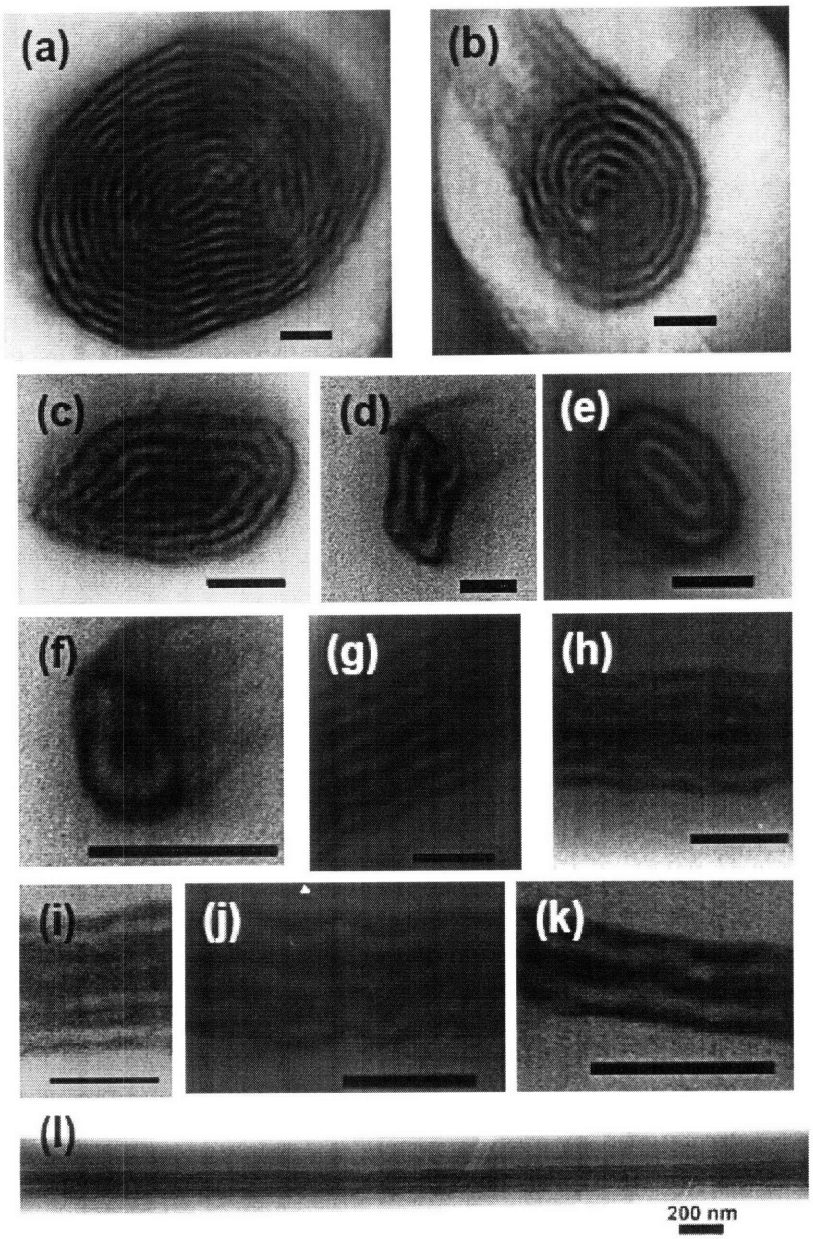

Figure 11-4 TEM images of the V4411 PS-PI-PS block copolymer in the fiber cores of different diameters after annealing, showing the concentric lamellar structure formed by the block copolymer. (a)-(f): axial views; (g)-(l): longitudinal views. (Scale bars in (a)-(k): 100 nm)

11.2 PS-PDMS Diblock Copolymer

The second type of lamella-forming block copolymer investigated here is

PS-PDMS diblock copolymer. PS and PDMS are well known for their strong immiscibility, exhibiting a relatively high Flory interaction parameter, $\chi_{PS/PDMS}$=0.32 at 20 °C (estimated from the group contribution methods[121]); this leads to strong phase segregation even at relatively high temperature and low molecular weights. The thermal stability of PS-PDMS block copolymers also ensures that no polymer degradation or oxidation occurs during the prolonged high temperature annealing which is required to obtain long range order within the electrospun fibers. In this work, two different lamella-forming PS-PDMS block copolymers will be used. For the shell material, a poly(methacrylic acid) (PMAA) was used. This polymer has a T_g of 220 °C much larger that that of PS (105 °C) or PDMS (-120 °C); in the presence of the PMAA shell, fiber dimensions remains unchanged upon annealing at 160 °C for 10 days under vacuum.

The first PS-PDMS block copolymer (PS-PDMS-L1) investigated here has a total molecular weight (Mw) of 93.4 kDa, PS volume fraction* of 55% and polydispersity index (PDI) of 1.04 and forms a lamellar morphology in bulk with a period (L_0) of 56 nm as determined by SAXS. A mat composed of the PMAA/PS-PDMS-L1 core-shell electrospun fibers and the ordered structure formed upon annealing are shown in Figure 11-5. Long continuous fibers of PS-PDMS-L1 (Figure 11-5c) can be produced by removal of the PMAA shell using methanol as the selective solvent. The average diameter of the core-shell fibers is 800±150 nm, while that of the PS-PDMS-L1 core fibers is 300±220 nm. The concentric lamellar structure formed in

* This volume fraction was obtained from ^{1}H-NMR, while image analysis on the bulk TEM images suggested the PS volume fraction was about 60%.

the fibers is consistent with observation for the lamella-forming V4411 PS-PI-PS block copolymer discussed above. Figure 11-5 (e) shows that the PS block preferentially segregates to the core-shell interface with PMAA due to its lower Flory interaction parameter ($\chi_{PS/PMAA}$=0.14 at 160 °C) compared to that of PDMS with PMAA ($\chi_{PDMS/PMAA}$=0.72 at 160 °C). As expected, this PS monolayer is approximately half as thick as the inner PS domains, which are bilayers.

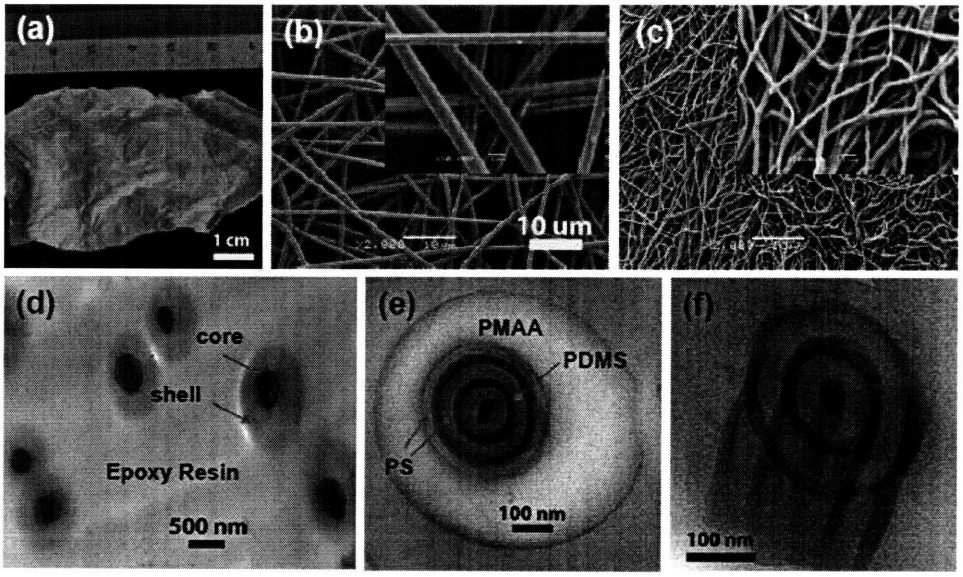

Figure 11-5 A multi-scale view of an electrospun PS-PDMS-L1 block copolymer fiber mat. (a) A macroscopic image of the PMAA/PS-PDMS-L1 fiber mat (scale bar = 1 cm); (b) SEM image of the as-spun core-shell fibers (scale bar = 10 μm); (c) SEM image of the PS-PDMS-L1 core fibers after removal of the PMAA shell using methanol (same magnification as (b)). (d), (e) Cross sectional TEM images of the fibers after annealing, showing the core-shell structure and concentric lamellar structure in the core; in (e), the dark layers are PDMS due to its higher electron density, and the light layers are PS. The region surrounding the PS-PDMS-L1 core is the PMAA shell. (f) A tilt TEM image of a PS-PDMS-L1 core, showing a 2D projection of the 3D concentric lamellar structure. Note that the outmost PS monolayer is not resolved in this image due to the lack of sufficient contrast between PS and PMAA in this case.

As in the case of V4411, the number of PS/PDMS bilayers depends on the

core sizes. Figure 11-6 shows representative examples from 2 to 9 bilayers. A quantitative analysis on the relationship between number of bilayers and core size will be presented in next section.

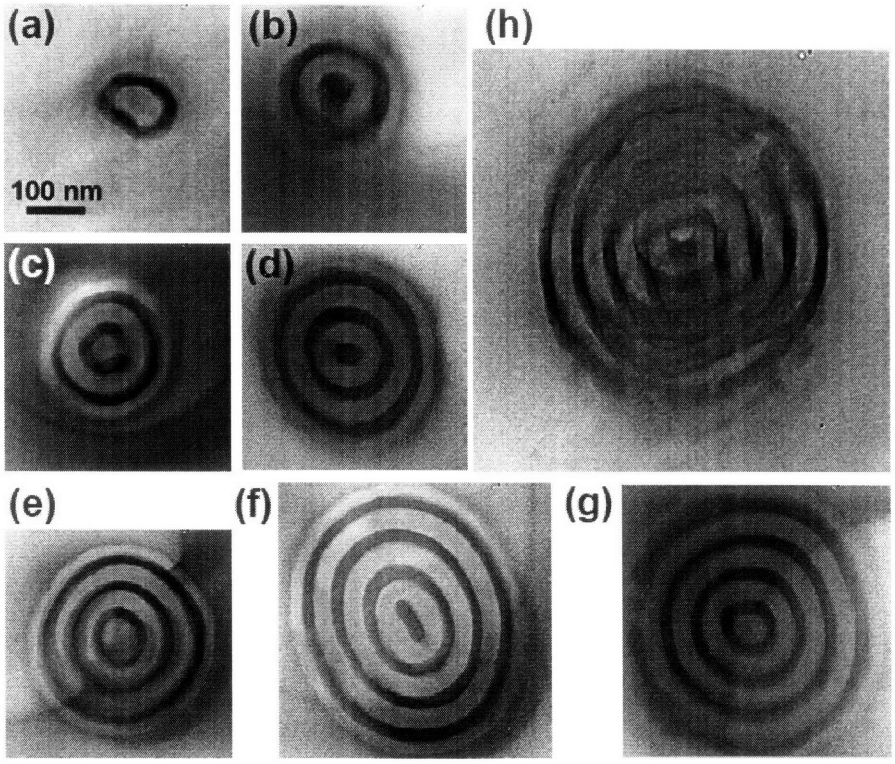

Figure 11-6 Axial views of the concentric lamellar morphology formed by the PS-PDMS-L1 confined in electrospun fibers with different sizes. All images are presented at the same magnification.

11.3 The Effect of Cylindrical Confinement on the Lamellar Domain Structure

To understand quantitatively the effect of cylindrical confinement on the block copolymer self-assembly, image analysis on different cross sectional TEM images of the PS-PDMS-L1 core (see Figure 11-7 to Figure 11-9 for examples) was performed. The total number of bilayers (N) is plotted as a function of the diameter (D) of core, as illustrated in Figure 11-10 (a). D/N is the average thickness of a complete bilayer of PS and PDMS. The degree of confinement can be expressed as the ratio, D/L_0. As D

increases, N increases in a discrete manner. However, N is not determined uniquely by D/L_0; different numbers of bilayers (e.g. $N = 6$ and $N = 7$) may be observed at the same degree of confinement (e.g $D/L_0 \sim 6.5$). Similarly, for a given N, a range of PS-PDMS-L1 core diameters (D) is observed. Experiments and simulations have previously reported average periods (D/N) both larger and smaller than in bulk. In these electrospun fibers, the distribution of D/N suggests that domains may be either compressed or expanded relative to bulk in the larger fibers ($D/L_0 > 5$). However, for the smaller diameter fibers observed ($D/L_0 < 5$), the data fall predominantly below the line, indicating that these domains are significantly expanded relative to bulk. This trend points to a systematic deviation of the domain size from the average. In this respect, the concentric lamellar morphology differs qualitatively from that observed in thin films.[85,86] This has been recognized previously by others, although no unanimous conclusion has been reached on whether the domains are expanded or compressed.

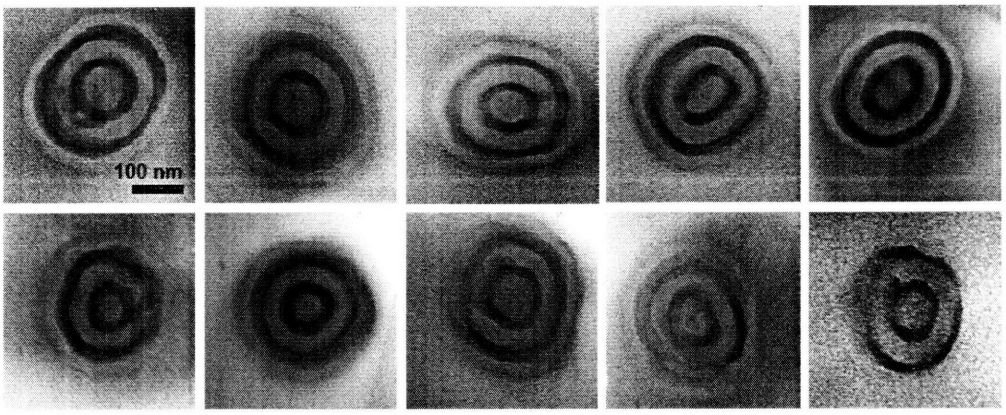

Figure 11-7 Axial views of the concentric lamellar morphology formed by PS-PDMS-L1 with 4 bilayers. All images are presented at the same magnification.

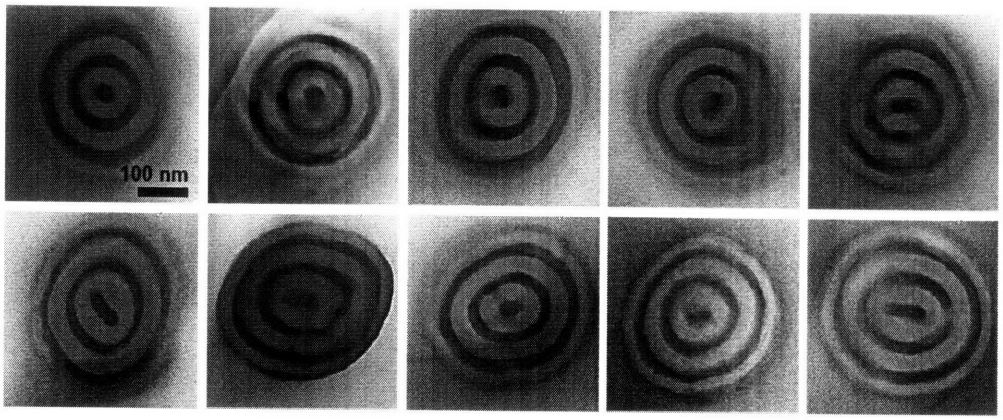

Figure 11-8 Axial views of the concentric lamellar morphology formed by PS-PDMS-L1 with 5 bilayers. All images are presented at the same magnification.

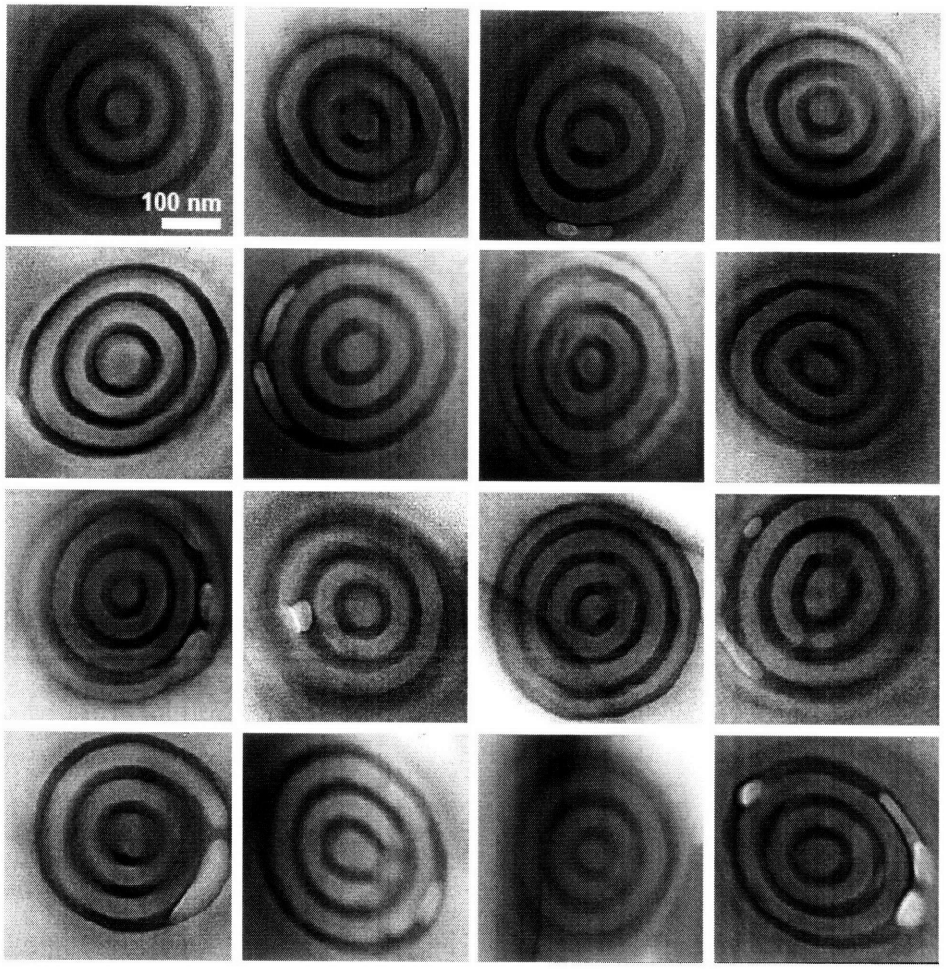

Figure 11-9 Axial views of the concentric lamellar morphology formed by PS-PDMS-L1 with 6 bilayers. The brightest holes in PDMS domains in some of the images (e.g. last one) are probably due to dewetting during high temperature annealing. All images are presented at the same magnification.

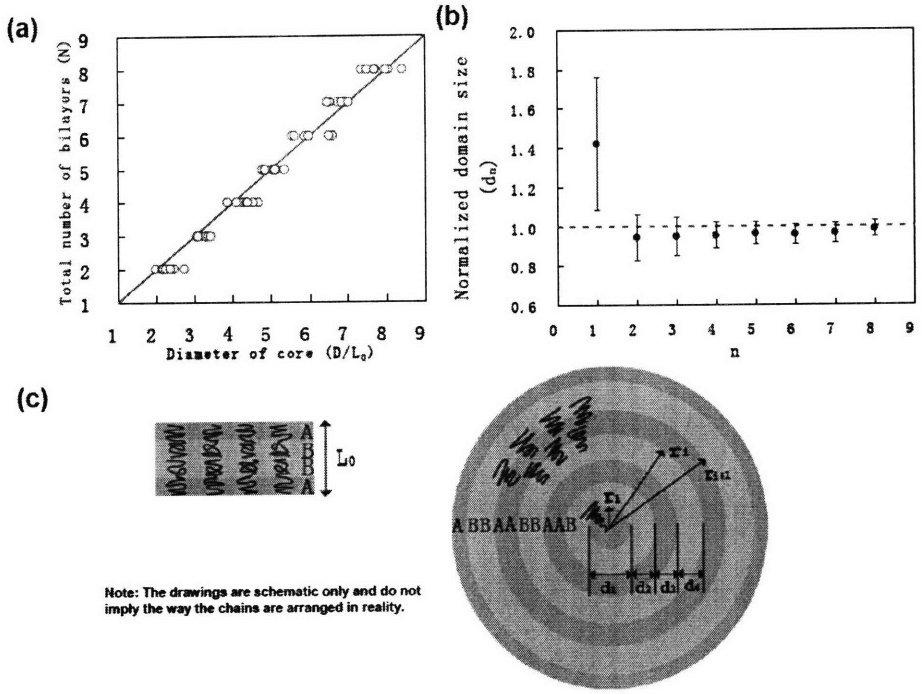

Figure 11-10 The effect of cylindrical confinement on the domain size of lamellar morphology. (a), Total number (N) of bilayers as a function of degree of confinement (D/L_0). The red line is a reference line based on the morphology of the unconfined bulk: $N = D/L_0$. The blue circles are data points from different TEM cross sections of electrospun fibers. D is defined as the diameter of the PS-PDMS-L1 core of fibers. (b), Dependence of domain thickness d_n on domain index, n, where d_n is defined as the distance between successive AB interfaces (A=PS and B=PDMS), counting from the central domain outward. The outermost PS domain is a monolayer and is approximately half as thick as other PS domains, so it is not included in the plot. (c), From left to right, schematics for block copolymer chains in bulk and in a fiber (axial view).

To explore this systematic deviation more closely, we show in Figure 11-10 (b) the variation of domain size as a function of domain number, counting from the axis of the fiber outward. The domain sizes are normalized by their unconfined bulk values for PS (34 nm) and PDMS (22 nm), respectively. This figure shows unambiguously that the sizes of outer domains (d_n, $n>1$) are only slightly smaller (less than 10% on average) than the bulk value, and that they approach the bulk value with increasing domain number. Meanwhile, the central domain (d_1) is 42% larger than the bulk

value. The unique behavior of the central domain explains why the D/N is systematically larger than L_0 for the smallest fibers.

It now remains only to account for the difference in size of the central and outer domains. For this purpose, we treat the PS-PDMS block copolymer chain very simply as comprising two strongly segregated brushes, A and B, of equal length, joined together at the AB interface (Figure 11-10c) so that the bulk domain size for each block is $L_0/2$. In bulk, equating the number of copolymer blocks within a domain bounded by two successive AB interfaces with the number of copolymer chains crossing each of the two interfaces (of equal area) leads to the following equation,

$$c_0 = \lambda_0 L_0/2 \qquad (1)$$

where L_0, c_0 and λ_0 are the bulk period (i.e. the bilayer thickness), interfacial chain density (number of chains per unit interfacial area) and packing density (number of chains per unit volume), respectively. Applying a similar conservation of the number of polymer blocks (per unit length of fiber) to the central domain and outer cylindrical shells depicted in Figure 11-10c, we obtain

$$c_1 = \lambda_0 r_1 \qquad (2)$$

for the central domain and

$$c_i r_i + c_{i+1} r_{i+1} = \lambda_0 (r_{i+1}^2 - r_i^2),\ i = 1, 2, 3\ldots \qquad (3)$$

for the outer domains. c_i is the interfacial chain density at the i^{th} interface counting from the center of the fiber (*c.f.* Figure 11-10c). In the two equations above, the polymer is assumed to have the same packing density in the fibers as in bulk; the compressiblities of PS and PDMS are approximately 2×10^{-10} Pa^{-1} and 6×10^{-10} Pa^{-1},

respectively, rendering them essentially incompressible under these conditions.[122]

Equations (1) to (3) suggest that the domain sizes are related to the interfacial chain densities. We consider two limiting cases for an incompressible system: bulk-like interfacial chain density and bulk-like chain stretching. Taking first the case of bulk-like interfacial chain density, i.e. $c_i = c_0$, we get $r_1 = 0.5L_0$ and $r_{i+1}-r_i = 0.5L_0$ or equivalently, $d_1 = 2$ and $d_{n>1} = 1$. This result indicates that the domain in the center must be significantly expanded to maintain bulk-like block density and bulk-like interfacial chain density. Intuitively, it is a result of the excluded volume interactions among the polymer blocks in the central domain that would otherwise be "squeezed" by the singularity in volume at the axis of the fiber. However, expansion of the domain requires stretching of the polymer blocks confined in the center, which causes an unfavorable reduction in chain conformational entropy. Besides this space-filling induced entropy loss, there is additional entropy loss due to the curvature itself that restricts the range of angles the chain is allowed to explore. (See Figure 11-11)

On the other hand, taking the case of bulk-like chain stretching, (i.e. $d_1 = d_{n>1} = 1$ or $r_1 = 0.25L_0$ *and* $(r_{i+1}-r_i) = 0.5L_0$), the interfacial chain density at the first interface must decrease by a commensurate amount (i.e. $c_1 = 0.5c_0$) in order to maintain bulk-like block density within the domain. This results in an increased interfacial energy per chain. The curvature induced chain entropy loss is also larger due to the larger curvature in this case compared to previous case where the interfacial chain density is assumed to be equivalent to bulk. The experimental value observed for the size of central domain (Figure 11-10b) lies between the bulk value, $d_1 = 1$, and $d_1 = 2$

obtained for the case of bulk interfacial chain density, and can be explained simply as a consequence of the trade-off between the reduced chain entropy due to space-filling and curvature, and increased interfacial energy due to depletion of block junctions. This is similar to the case of block copolymer bulk, where the balance between the chain entropy and interfacial energy has been used to estimate the lamellar period in the strong segregation regime.[123] The experimental data are also consistent with the classic theory on curvature elasticity of block copolymer monolayers which showed curvature increased the interfacial area per chain or decreased the interfacial chain density compared to bulk. [124,125]

For the outer domains, the model suggests the domain sizes assume the bulk value if $c_i = c_0$, implying that the curvature does not affect phase behavior of the outer domains. In reality, curving the intrinsically flat interface in a lamella costs energy, resulting in a slightly decreased interfacial chain density, as demonstrated more dramatically for the central domain discussed above. This reduction in interfacial chain density consequently causes a decrease of the domain sizes, consistent again with the experimental data where the outer domains are slightly smaller than bulk value. Here similarly, the increase in interfacial energy due to the reduction in interfacial chain density and the curvature caused chain entropy loss are compensated by the entropy gain by lessening the stretching of chains from their preferred random-coil conformation compared to bulk. In addition, the experimental data show a trend where the sizes of domains approach the bulk value as the domain index increases. This may be explained by the decreasing curvature effect as the radii of the

interfaces increases.

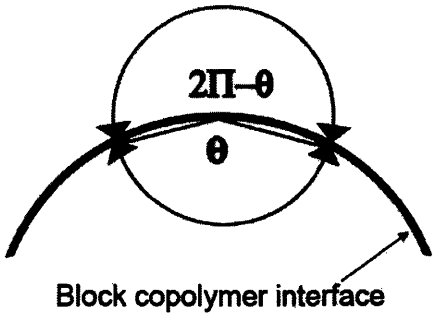

Figure 11-11 Schematics for curved block copolymer interfaces. Compared to a flat interface, the curvature decreases the range of angles the block in the concave side is allowed to explore and therefore its conformational entropy, while increases the range of angles the block in the convex side is allowed to explore and its entropy. The net entropy change for the whole chain, with the flat interface as the reference state, can be estimated as, $\Delta S(\theta) = ln\,[\theta(2\pi-\theta)] - ln\,(\pi^2)$, where θ depends on both the curvature and the characteristic dimension of the chain. This equation suggests that the curvature always causes an entropy loss for a symmetric block copolymer.*

11.4 Long Range Order of Concentric Lamellar Morphology

With respect to formation of fibers with long range order, the important question is the mechanism by which the cylindrical morphology is interrupted as the number of domains varies along the length of the fiber. The unique behavior of the central domain in fibers with concentric lamellar morphology offers some insight into this question. Taking advantage of the long continuous nature of electrospun fibers, we can locate and examine transitions in domain number as the core diameter varies. Figure 11-12 shows some representative longitudinal views of the cylindrical layer

* For more details, see coming PhD Thesis by Kirill Titievsky at MIT.

structure near transition points in the number of domains. A few observations can be made here. First, given the same number of domains, as the diameter of the core increases (e.g. larger D, along the direction of the arrow in Figure 11-12a), the change in diameter is mostly absorbed by the central domain, while the outer ones stay approximately the same. This is consistent with the plot in Figure 11-10 (b) where the central domain is shown to have a much larger variation than the outer ones. Second, as the diameter of the core increases further, one more bilayer is inserted to relax the large stress that would be experienced by the overly expanded central domain. This phenomenon is very similar to the formation of dislocation structure in smectic liquid crystals.[126] After the transition in the number of layers, the outer domains are slightly compressed, while the newly inserted domain is always larger than the bulk domain size. (See Figure 11-12e for details) This is again in contrast to the case of planar confined block copolymer thin films, where all domains change size equally to accommodate a new bilayer. Third, only one domain (the central one in most cases) bifurcates to increase the number of bilayers and all other domains are unaffected and essentially continuous – that is, the transitions are merely defects in this otherwise excellent long range order. Indeed, defect-free long range order was observed for fibers with less variation of core diameters. (See Figure 11-13) Lastly, disk-like stack of lamellae oriented with their normal parallel to the fiber axis were not observed for any of the fibers we examined. This is consistent with the strong interactions between the PS block and the PMAA shell, as pointed out recently by Sevink *et al.* [112] The perpendicular lamellae were seen by Kalra *et al.* [127] for poly(styrene-*b*-isoprene)

confined in silica, but were attributed to flow field rather than incommensurability.

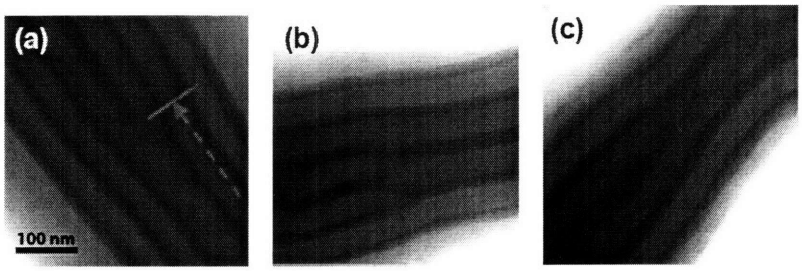

(e)

# of bilayers	d_1	$d_{n,avg}$ (n>1)
6→7 (a)	1.87→1.34	0.85→0.83
5→6 (b)	1.22→1.02	1.04→0.86
4→5 (c)	1.73→1.36	1.02→0.94
3→4 (d)	1.16→1.38	1.06→0.92

Figure 11-12 Longitudinal views of the concentric lamellar structure near dislocation point. (a)-(d), TEM images showing the number of bilayers increases by one as the diameter of the core increases. (e), The domain size changes for (a)-(d). $d_{n,avg}$ (n>1) is an average of outer domains. All images are at the same magnification.

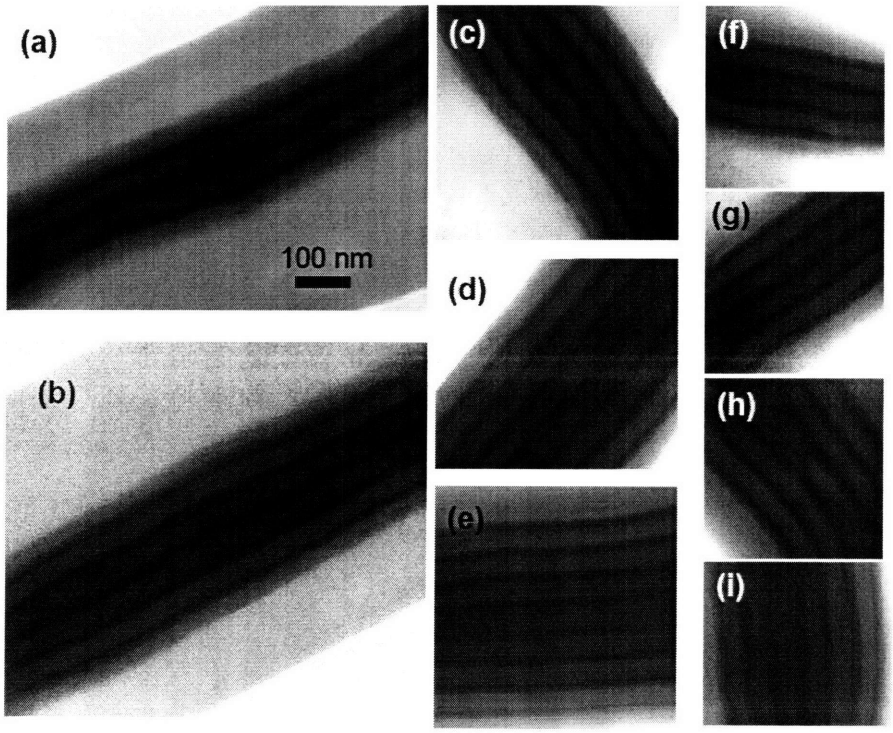

Figure 11-13 Longitudinal TEM images of the PS-PDMS-L1 block copolymer confined in core-shell electrospun fibers with nearly uniform core diameters. All images are presented at the same magnification.

Finally, similar phenomena as described above were also observed for a second lamella-forming PS-PDMS block copolymer (denoted as PS-PDMS-L2) that has a different total molecular weight (Mw = 46.4 kDa) but similar PDI (1.08) and PS volume fraction (~50%). (See Figure 11-14 for TEM images and details)

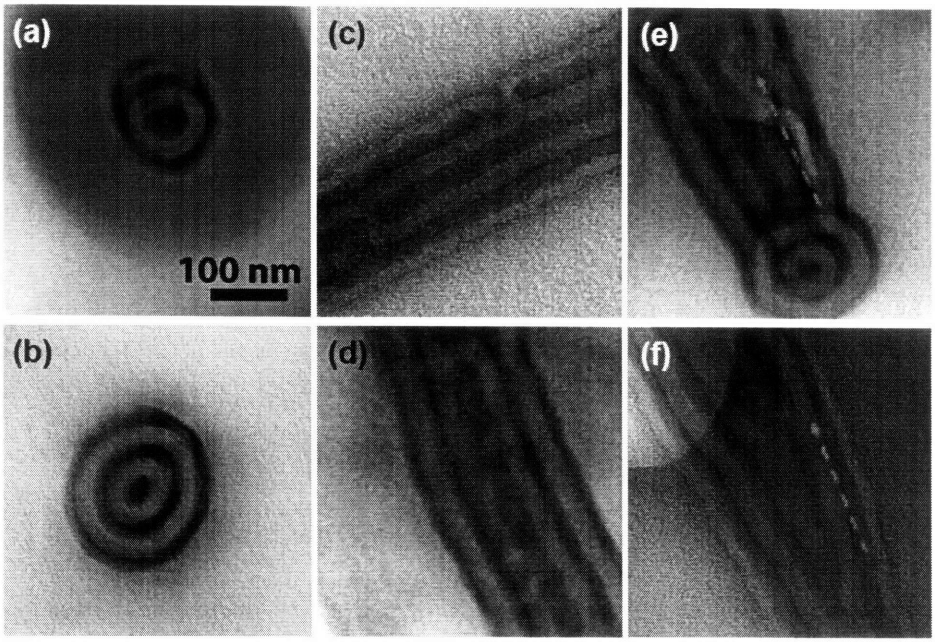

Figure 11-14 TEM images of PS-PDMS-L2 (L_0=42 nm) confined in electrospun fibers. (a), (b) Axial views. (c)-(f) Longitudinal views. The domain in the center is about 40% (a, c), 15% (b) and 45% (d) larger than the bulk value, and the outer domains are all slightly smaller the bulk value. In (e) and (f), 75% and 92%, respectively, of the increase in confinement size (indicated along the arrows) is absorbed by the central domain. All images have the same magnification.

Chapter 12 Other Types of Block Copolymers under Cylindrical Confinement

This chapter describes preliminary data on the morphology formed by sphere-, cylinder- and gyroid-forming block copolymers confined in core-shell electrospun fibers.

12.1 Sphere-forming Block Copolymers

To study the effect of cylindrical confinement on sphere-forming block copolymers, a PS-PI block copolymer (denoted as PS-PI-S1, See Table 9-1 for details) was used. It forms spherical morphology in bulk as shown by the TEM image in Figure 12-1 (a), consistent with its composition. [128] The P(MMA-*r*-MAA)/PS-PI-S1 core-shell electrospun fibers made by the two-fluid electrospinning were shown in Figure 12-1 (b).

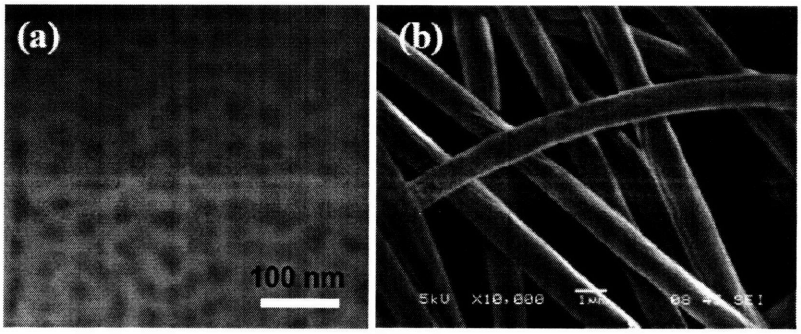

Figure 12-1 Co-axial electrospinning of the PS-PI-S1 block copolymer. (a), TEM image of the PS-PI-S1 in bulk; (b), SEM image of P(MMA-*r*-MAA)/PS-PI-S1 core-shell fibers.

The core-shell structure and block copolymer microphase separated structures in as-spun fibers are shown in Figure 12-2. The microphase separation is quite

random, as expected.

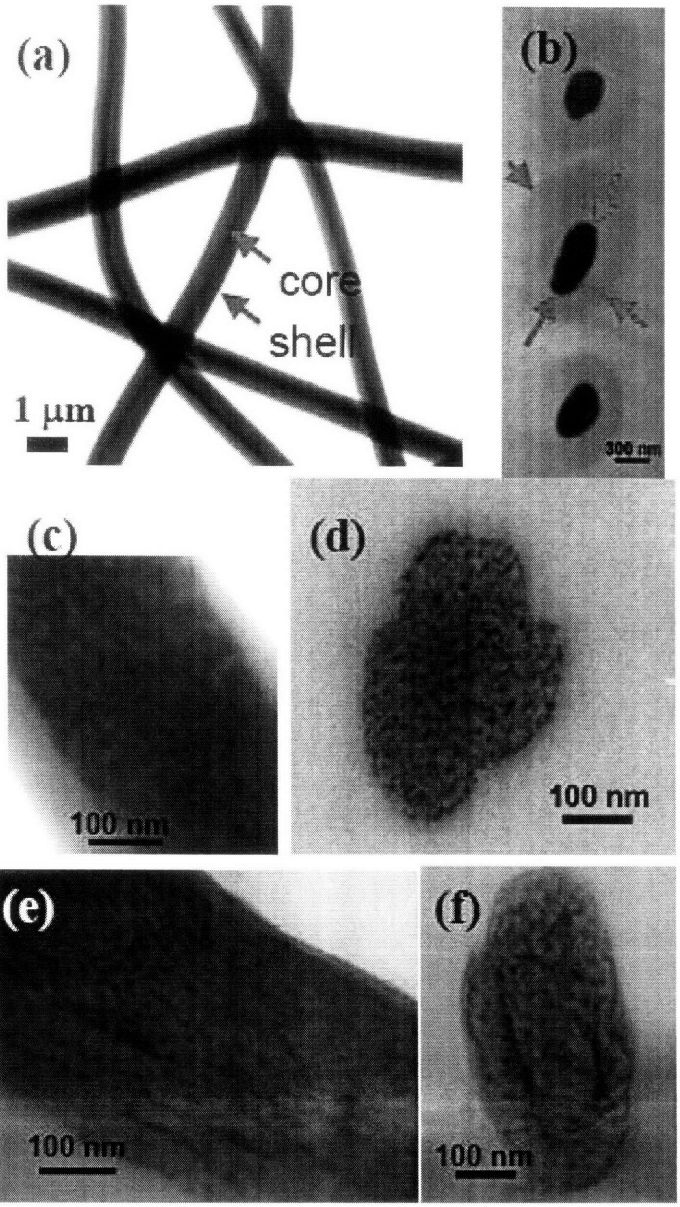

Figure 12-2 TEM images of the P(MMA-*r*-MAA)/PS-PI-S1 fibers. (a), (c) and (e): longitudinal views; (b), (d), (f): axial views.

Figure 12-3 shows typical TEM images of the PS-PI-S1 core after annealing at 140 °C for 10 days. The images show clearly the spherical isoprene microdomains dispersed in the styrene matrix, in contrast to the incomplete microphase separation

observed in as-spun fibers.

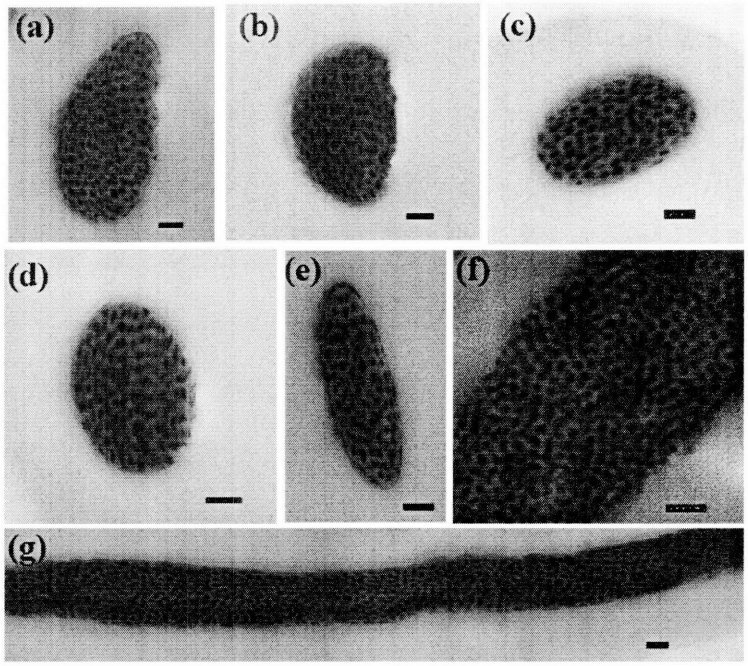

Figure 12-3 TEM images of the PS-PI-S1 block copolymer in the cores of annealed fibers with relatively large diameters. (a)-(e): axial views; (f)-(g): longitudinal views. Note that the spherical isoprene domains were distorted by the cutting during microtomy in some cases. The scale bars are 100 nm.

The confinement effect becomes obvious as the core size decreases. In small fiber cores (see Figure 12-4), the spherical microdomains tend to line up in concentric shells parallel to the core-shell interface. This is in contrast to the bcc packing typical of spheres in the bulk state, but is consistent with observations by Cheng *et al.*[129] of spherical domain packing in parallel-sided grooves etched in silicon. Similarly, Yokoyama *et al.* have shown that hexagonally packed spheres persist for many layers away from a flat substrate before the packing reverts to the bcc structure characteristic of the bulk.[130] The number of spherical microdomains within a cross-section of the fiber core decreases as the core diameter decreases, from approximately 20 domains

in a fiber of core diameter 160 nm (Figure 12-4a) down to a single domain in a fiber of core diameter 60 nm (Figure 12-4h) In some of these fibers, isoprene is observed to form a thin surface layer, again suggesting debonding of the SI core from the surrounding shell in some fibers.

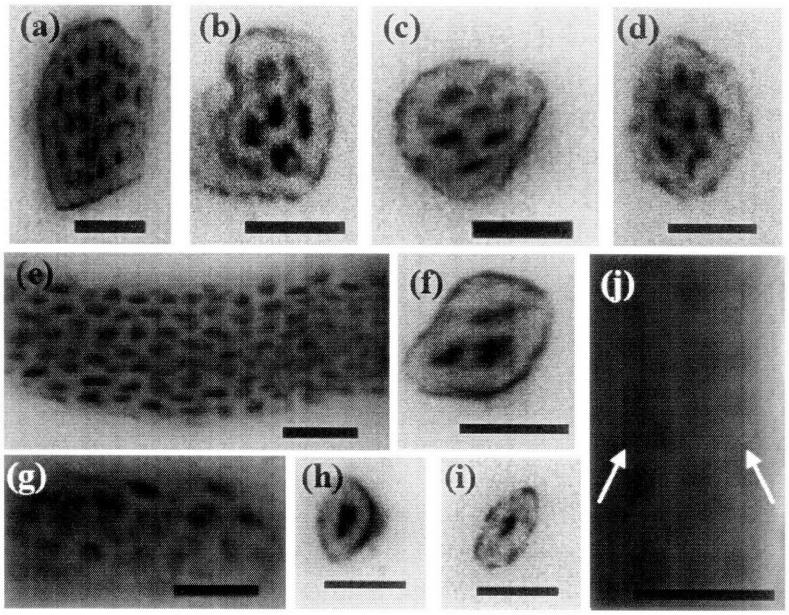

Figure 12-4 TEM images of the PS-PI-S1 block copolymer in the cores of annealed fibers with relatively small diameters; (a)-(d), (f), (h) and (i): axial views; (e), (g) and (j): longitudinal views. The arrows in (j) indicate the profile of the core. The scale bars are 100 nm.

A second sphere –forming block copolymer used is PS-PI-S2, which has similar molecular weight as PS-PI-S1 but different composition. The TEM images of the PS-PI-S2 core in annealed fibers shown in Figure 12-5 indicate again the well-defined spherical microdomains that tend to align parallel to the core-shell interface.

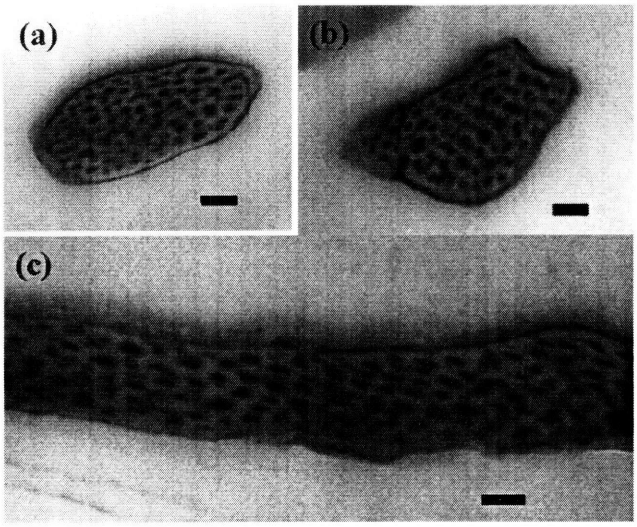

Figure 12-5 TEM images of the PS-PI-S2 block copolymer in the cores of annealed fibers. The scale bars are 100 nm.

12.2 Cylinder-forming Block Copolymers

For cylinder-forming block copolymers, V4211 was chosen as an example. This PS-PI-PS triblock copolymer forms cylindrical morphology with an intercylinder spacing of 31 nm and cylinder diameter of 8.3 nm, according to previous studies.[131] Figure 12-6 (a)-(c) show TEM images of this copolymer from a section of solution-cast film. The P(MMA-*r*-MAA) was chosen again as the shell material for the two-fluid electrospinning. The core-shell fibers as well as their internal structures are shown in Figure 12-6 (d)-(f).

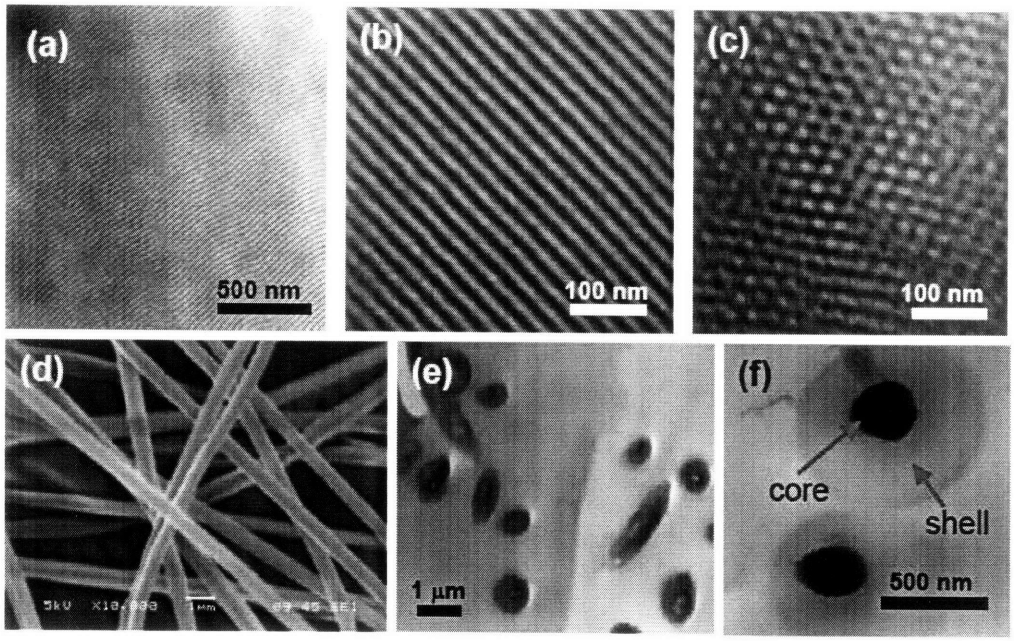

Figure 12-6 Co-axial electrospinning of the V4211 PS-PI-PS triblock copolymer. (a)-(c), TEM images of the V4211 cylinder-forming block copolymer in bulk with electron beam incident perpendicular (a-b) and parallel (c) to the cylinder axes; (d), SEM image of the P(MMA-*r*-MAA)/V4211 core-shell fibers; (e) and (f), Cross-sectional TEM images showing the core-shell structure.

The self-assembled structures of V4211 in annealed fibers are shown in Figure 12-7. PS cylindrical domains are seen dispersed in the PI matrix, consistent with bulk morphology. The cylindrical domains are aligned along the axis of the fibers and tend to line up in concentric shells especially in small cores. This is different from the hexagonal packing in bulk, but similar to the case of sphere-forming block copolymers where the domains line up in concentric shell manner.

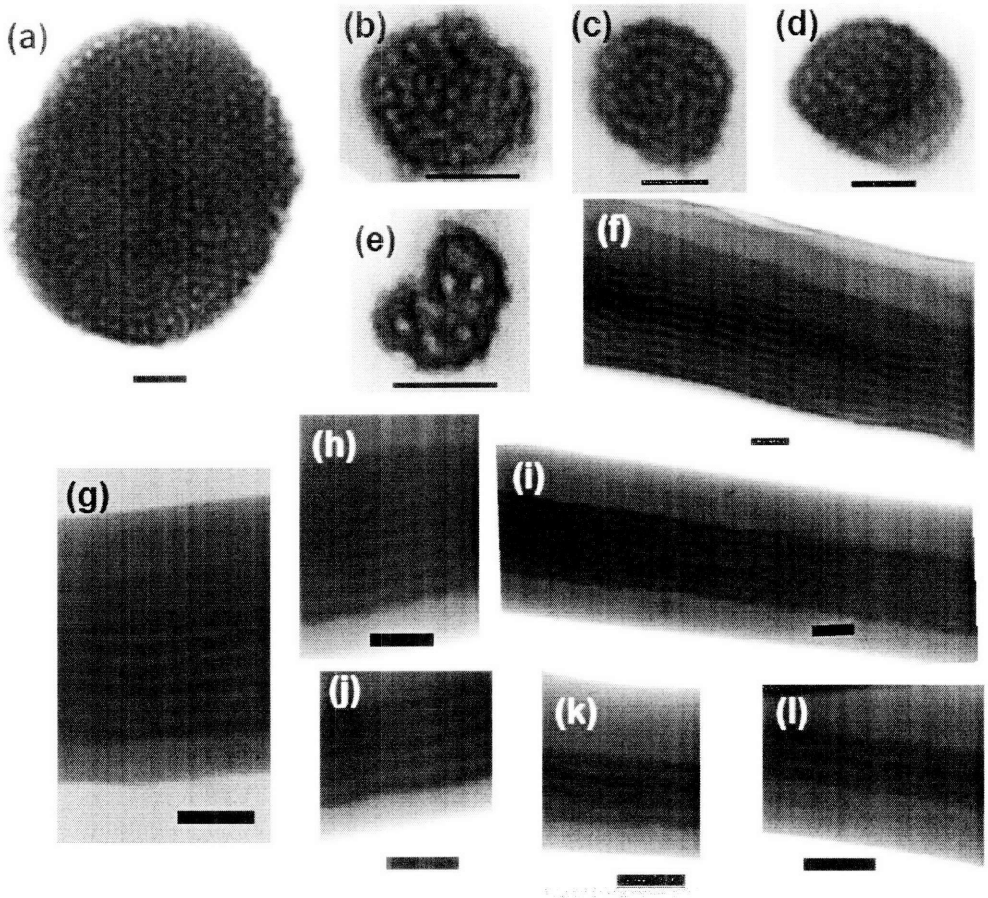

Figure 12-7 TEM images of the V4211 cylinder-forming block copolymer confined in relatively large electrospun fibers. (a)-(e), axial views; (f)-(l), longitudinal views. Scale bars: 100 nm. (Some of the images have been modified by Photoshop to enhance their visibility.)

Remarkably, morphologies that differ from cylinders were observed as the sizes of the fiber cores further decrease. Figure 12-8 shows a few TEM images of V4211 confined in fibers with core sizes less than 100 nm. Figure 12-8 (a)-(c) show that helical structure forms at core sizes of about 1 to 2 times the inter-cylinder spacing, while helix with a central spin forms at slightly larger core sizes. Both of the morphologies have been predicted by Li *et al.* [113] and Chen *et al.* [114] using self-consistent mean-field theory.

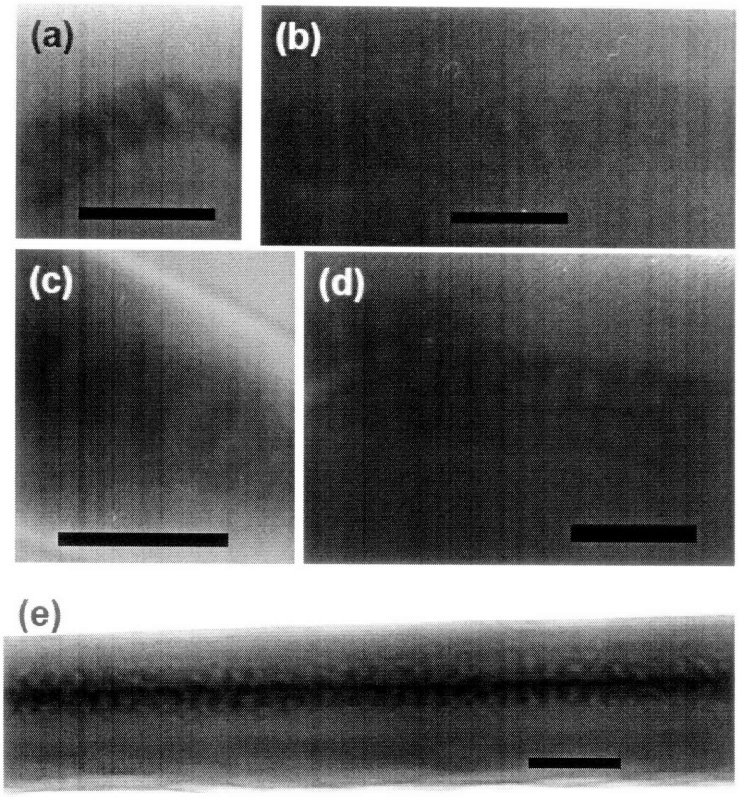

Figure 12-8 TEM images of the V4211 cylinder-forming block copolymer confined in relatively small electrospun fibers. (a)-(e), axial views; (f)-(l), longitudinal views. Scale bars: 100 nm.

12.3 Gyroid-forming Block Copolymers

The double gyroid is a particularly interesting phase because of its double network structure and three-dimensional (3D) periodicity. [132] For example, nanoporous ceramic films can be fabricated from gyroid-forming block copolymer precursors.[133] However, gyroid-forming block copolymers under confinement have not been well studied. The PS-PDMS-G1 was first chosen to study the morphology of gyroid-forming block copolymer under cylindrical confinement. It forms double gyroid structure in bulk with [211] spacing of 61 nm. (See Figure 12-9 (a)-(c) for

TEM images.) Figure 12-9 (d) shows the core-shell fibers using PMAA as the shell. The PS-PDMS-G1 fibers were obtained after the removal of PMAA using methanol. (Figure 12-9d)

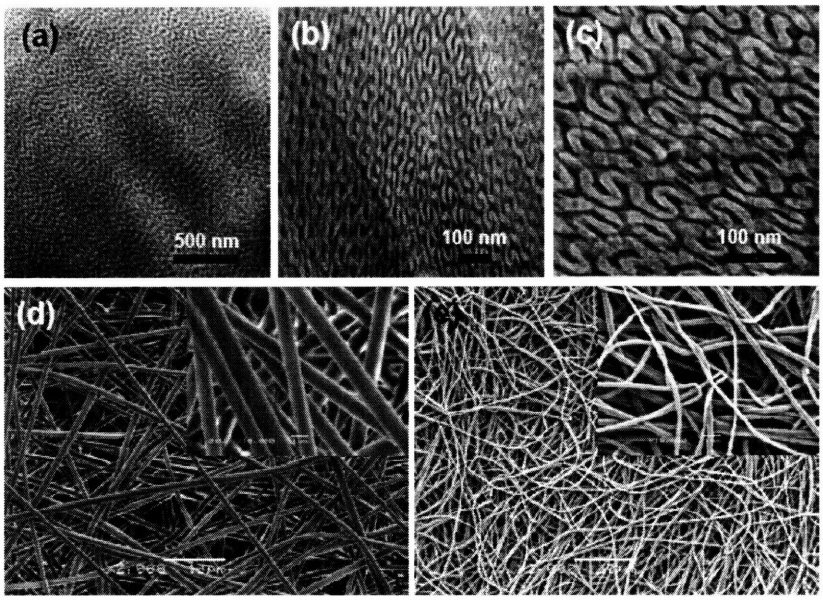

Figure 12-9 Co-axial electrospinning of the PS-PDMS-G1 block copolymer. (a) to (c), TEM images of the gyroid-forming PS-PDMS block copolymer (PS-PDMS-G1) in bulk. (d), SEM image of the PMAA/PS-PDMS-G1 core-shell fibers. (e), SEM image of the PS-PDMS-G1 core fibers obtained from the removal of PMAA shell. The insets are corresponding higher magnification images.

Figure 12-10 shows cross-sectional TEM images of the PMAA/PS-PDMS-G1 fibers after annealing. Concentric lamellar structures similar to those formed by lamella-forming block copolymers are observed. This observation suggests that a fundamental phase transition, from gyroid to lamella, has occurred under the cylindrical confinement. This phase transition is probably induced by the preferred interfacial wetting at the core-shell interface. As in the case of PMAA/PS-PDMS-L1 fibers, the PS blocks preferentially wet the PMAA confining wall (Figure 12-10 b-d) and this PS layer subsequently drives the formation of successive inner lamellar layers.

Similar phase transition was observed in thin films of the same polymer (PS-PDMS-G1) confined between two PMAA layers. (Figure 12-11 for TEM images and experimental details.)

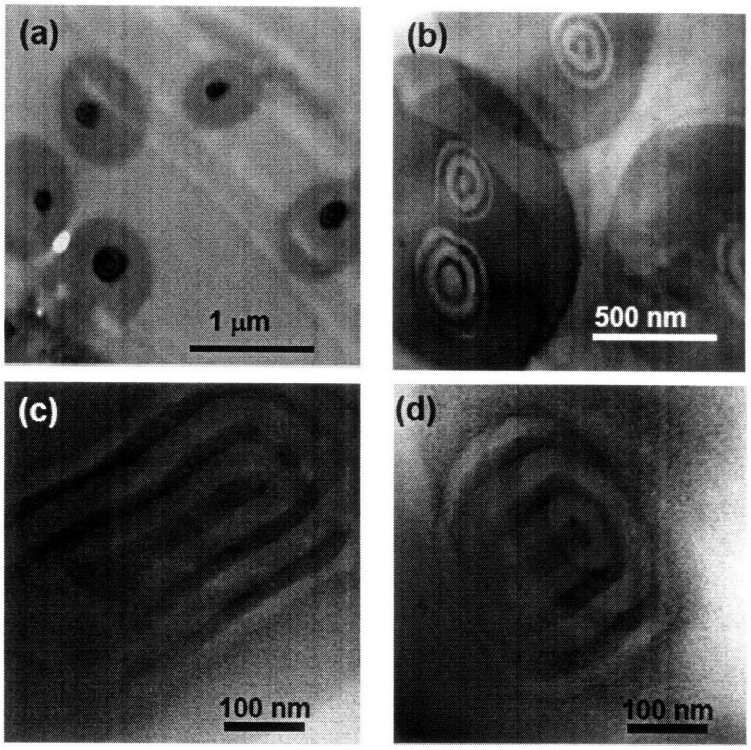

Figure 12-10 TEM images of the PMAA/PS-PDMS-G1 fibers. (a) core-shell structure; (b) self-assembly structure of the PS-PDMS-G1 in the fibers; (c) and (d), longitudinal view and tilt view of the concentric lamellar structure formed by the PS-PDMS-G1.

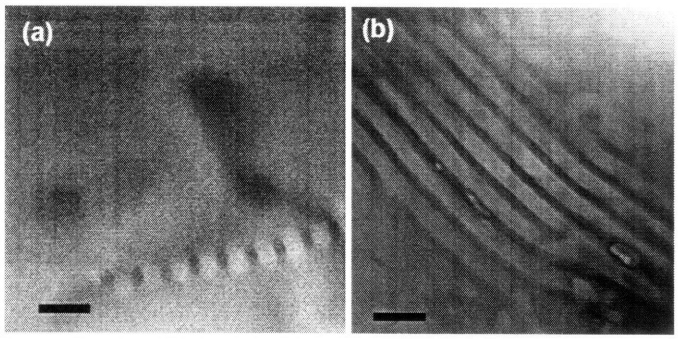

Figure 12-11 TEM images of PS-PDMS-G1 thin film. (a), Plan view;* (b), Cross-sectional view. Scale bars: 100 nm. The film was made by sequentially spin-coating PMAA, PS-PDMS-G1 and PMAA layers on a glass slide. The film was

* The strip pattern which is likely to be a 2-D projection of a Scherk's First Surface indicates that the lamellae may undergo a 90° twist reorientation.[132]

then floated onto methanol after annealing.

Similar to PS-PDMS-L1, PS-PDMS-G1 forms different number of bilayers in cores of different sizes. Figure 12-12 also shows that, for the same number of bilayers, the core sizes can be significantly different. It is notable although not obvious that in some cases (e.g. Figure 12-12 k1) the PDMS layers show a periodic variation of contrast along azimuthal direction, indicating that the PDMS lamella may be perforated in this case. In bulk, the hexagonally perforated lamellar (HPL) phase appeared as metastable morphology intermediating lamella and gyroid.[134]

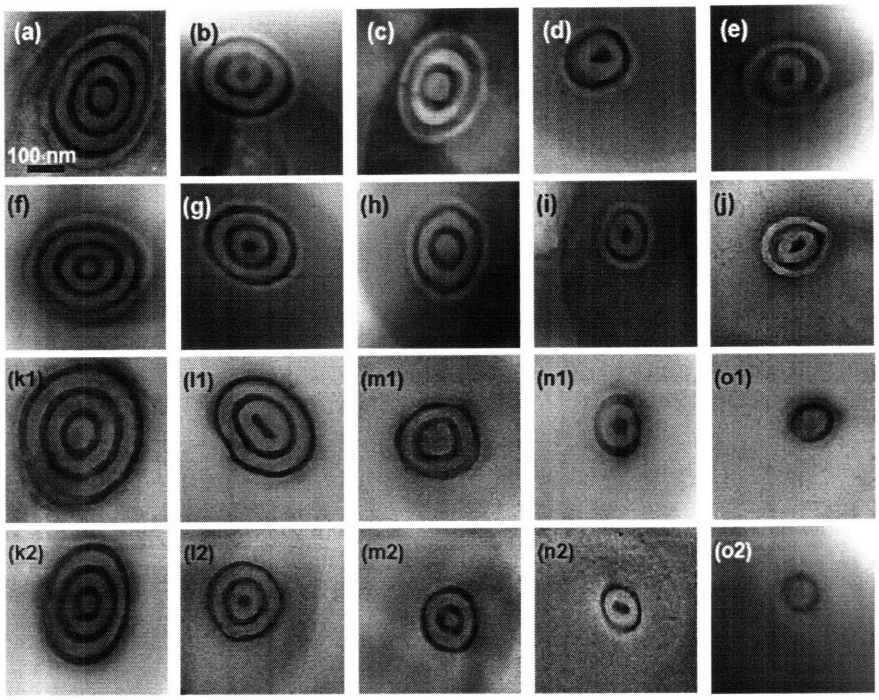

Figure 12-12 Cross-sectional TEM images of the PS-PDMS-G1 block copolymer under cylindrical confinement, showing the concentric lamellar morphology. Note the differences of the core sizes between cross sections with same number of bilayers. The outmost PS monlayers are resolved in (a)-(j), while those in (k)-(o) are not well resolved due to the lack of contrast between PS and PMAA.

Besides the typical concentric lamellar morphology, other unusual morphologies

were also observed for this PS-PDMS-G1 copolymer annealed under identical thermodynamic condition (i.e. 160 °C for 10 days under vacuum). Figure 12-13, Figure 12-14, and Figure 12-15 show axial TEM views of these unusual structures. Remarkably, some of the structures observed here are the same as the previous 2D theoretical predictions,[108] but the match does not necessarily imply that the simulation results can be completely used to explain the experimental data. The simulation was only for 2D microphase separation, while the structures observed here were not translationally invariant along the fiber aixs. However, similar structures have been seen in multiple cross sections, suggesting that they are not random but thermodynamically stable or metastable structures with local minimum free energy. They may be understood as the result of the competition between interfacial wetting and bulk packing. As mentioned above, the strong interfacial wetting between PS block and PMAA probably drives the formation of the outmost layer of PS and most likely subsequent inner layers. However, there exists packing frustration for the copolymer chains away from the confining wall which prefer to be bulk-like, for example to form the gyroid phase. Depending on which effect dominates, the copolymer chains away from the interface may form concentric lamellar structure or the unusual, gyroid-like structures. For example, the center region of the cross section in Figure 12-15 (d) has a threefold junction characteristic of gyroid phase and is essentially the same as the cross-sectional view from [11-2] direction for previous 2D simulation of a confined gyroid phase.[135]

Other unusual structures resemble the simulated TEM images (Figure 12-16)

obtained from molecular dynamics simulation by Kirill Titievsky.* From the simulated 3D structures, it appears that PS-PDMS-G1 forms a structure consisting of a combination of helical and hexagonally perforated concentric lamellar motifs. Lastly, comparison of core sizes between concentric lamellar structure and the unusual structures suggests that there is no clear correlation between confinement size and the domain morphology formed.

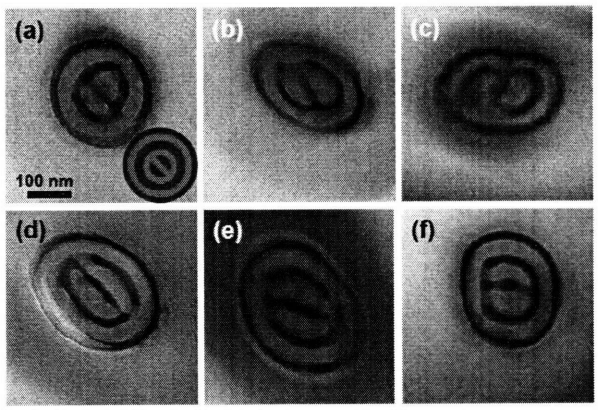

Figure 12-13 Cross-sectional TEM images of the PS-PDMS-G1 block copolymer confined in electrospun fibers, showing a projected structure similar to the schematically illustrated 2D simulation structure in the inset of (a).

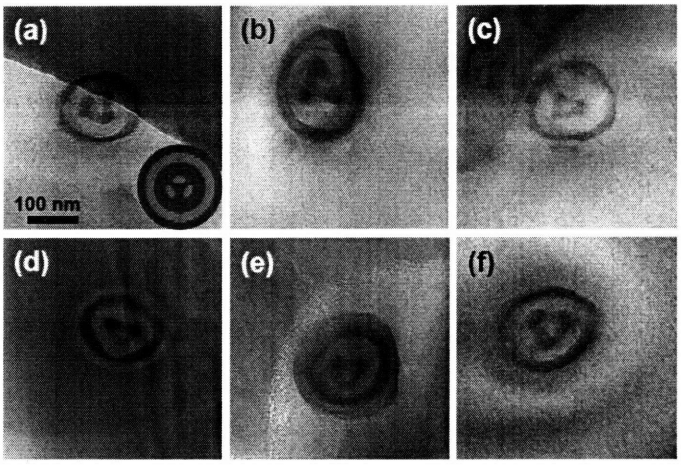

Figure 12-14 Cross-sectional TEM images of the PS-PDMS-G1 block copolymer confined in electrospun fibers, showing a projected structure similar to the schematically illustrated 2D simulation structure in the inset of (a).

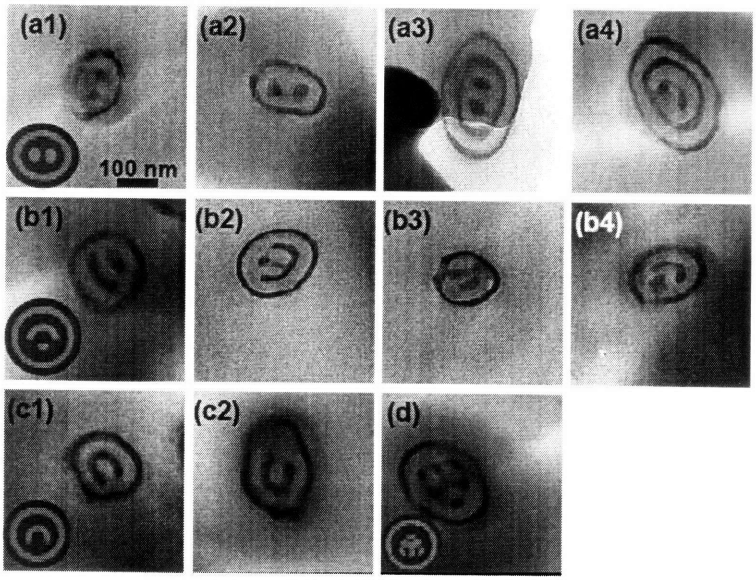

Figure 12-15 Cross-sectional TEM images of the PS-PDMS-G1 block copolymer confined in electrospun fibers, showing other unusual projected structure similar to the schematically illustrated 2D simulation structures in the respective insets.

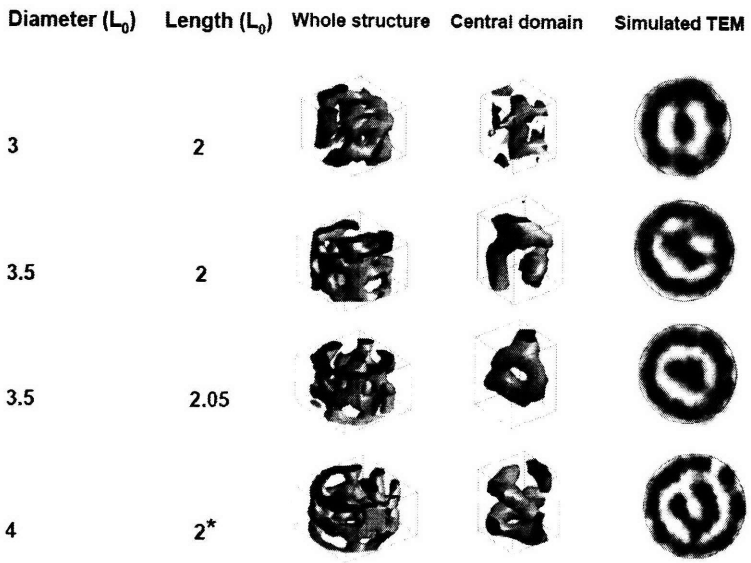

* The simulated TEM image corresponds to length of L_0 rather than the $2L_0$ used in simulation.

12-16 3D simulation results of a gyroid-forming block copolymer (A_4B_8) confined in cylindrical pores with different diameters and lengths. The majority component is assumed to be transparent. (Courtesy of Kirill Titievsky)*

* For details of simulation, see coming PhD Thesis by Kirill Titievsky at MIT.

To further verify that the structures formed by PS-PDMS-G1 under cylindrical confinement are not random, another gyroid-forming PS-PDMS block copolymer (denoted as PS-PDMS-G2) was investigated. The [211] spacing of PS-PDMS-G2 in bulk is 80 nm. Since the molecular weight of PS-PDMS-G2 is higher than the previous two PS-PDMS block copolymers, the fibers were annealed at a higher temperature, 170 °C, for 10 days under vacuum to ensure a near-equilibrium state. Figure 12-17 shows some representative TEM images of this polymer in annealed fibers. As observed for PS-PDMS-G1, concentric lamellar structure (Figure 12-17 a-e) as well as unusual structures (Figure 12-17 f-i) formed. The unusual structures observed here are similar to those formed by PS-PDMS-G1; they are again not translationally invariant but reproducible and stable.

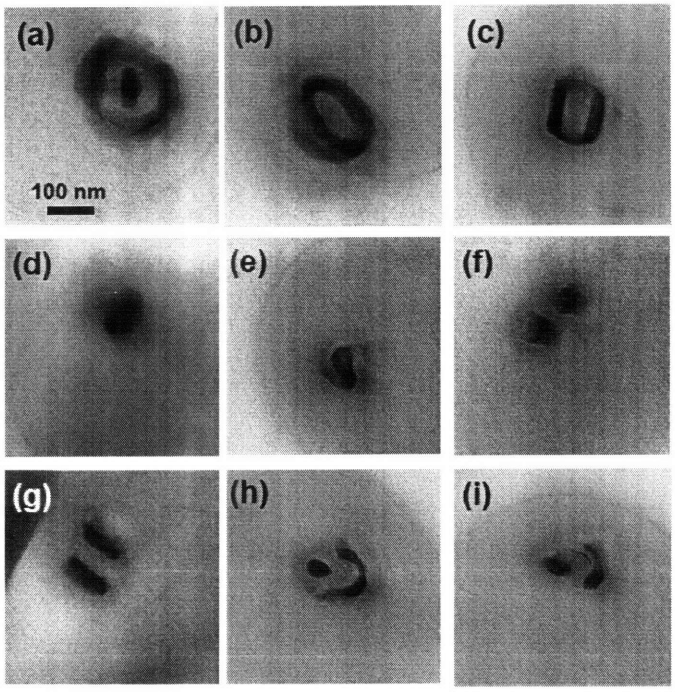

Figure 12-17 Cross-sectional TEM images of the PS-PDMS-G2 block copolymer

under cylindrical confinement, showing the concentric lamellar morphology (a-e) and the unusual morphologies (f-i). Note that in all images the outmost PS monolayer is not well resolved due to the lack of contrast between PS and PMAA shells surrounding PS.

Chapter 13 Conclusions and Recommendations

13.1 Conclusions

The second part of this dissertation mainly describes the author's work on self-assembly of cylindrically confined block copolymers in core-shell electrospun fibers. The most important contributions of this work include the processing strategy to get long-range ordering in block copolymer fibers using a two-fluid electrospinning method and detailed studies on the phase behavior of cylindrically confined block copolymers. Various novel block copolymer self-assembled structures were obtained in the form of long continuous fibers. Compared to the capillary absorption technique method developed by Russell *et al.* [103] and Stucky *et al.* [104] to confine block copolymers, the process described here allows the study of block copolymer microphase separation under cylindrical confinement by an industrially practical route that leads to continuous, structured fibers. This dissertation demonstrates the possibility to alter the shell material, thereby permitting greater freedom in the formation of fibers of different size and composition, as well as potential for exploration of surface and interfacial energy effects between the respective blocks and the shell material on the details of microphase separated structures of cylindrically confined block copolymers. Theoretical work has shown that a variety of morphologies such as stacked-disk and helical structures may arise as the surface energy varies. From the technological point of view, making well-structured, tailored block copolymer fibers is the first step towards a number of potential applications. For

example, decorating one of the blocks with nanoparticles or carbon nanotubes can be an effective way to disperse these nano-objects in electrospun fibers in well-controlled manner. Selective functionalization or removal of one of the blocks may lead to highly functional or porous fibers. Other areas where these fibers may find great applications include optical fibers, phase-selective chemistry and drug delivery.

For lamella-forming block copolymers, the cylindrical geometry is shown to alter the domain sizes in a way that is remarkably different from thin films. While the outer domains are slightly smaller than bulk value, the one in the center is much (42%) larger than the bulk value but smaller than the value estimated by assuming interfacial chain density equivalent to bulk. Both the central and outer domains can be explained by a reduction in interfacial chain density imposed by the curvature associated with the cylindrical geometry. The study presented here provides not only a basic explanation for the trends observed in the domain sizes but also insights into the defect formation. All the domains except the central one are essentially continuous and the increase in fiber core size is mainly accommodated by the central domain, through expansion or bifurcation. The "core-flip" defects can be avoided and extreme long range order can be achieved through tight control of fiber core size. This is a significant step towards the design of fibers for specific applications as mentioned above.

For sphere-forming block copolymers, the spherical domains are shown to line up in concentric shells. This is in contrast to the bcc packing of spheres in bulk. For

cylinder-forming block copolymers, the cylindrical domains are aligned with cylinder axes parallel to the fiber axis. These domains also tend to line up in concentric shells, similar to the case of sphere-forming block copolymers under confinement but different from the hexagonal packing of cylinders in bulk. Remarkably, novel helical domain structures were observed in fibers with extremely small cores. Finally, for gyroid-forming block copolymers, a fundamental phase transition from gyroid to lamella was observed due to the interfacial wetting and confinement. Several interesting and unusual structures were also observed as degenerate structures. The experimental observation along with the computer simulation by Kirill Titievsky revealed that these unusual structures appeared to be a combination of helical and hexagonally perforated concentric shell motifs.

13.2 Recommendations for Future Work

Based on the author's experience in working on the block copolymer self-assembly confined in electrospun fibers as discussed above, the following recommendations for future work in this area are proposed:

1. There are a lot of work left on the self-assembly of cylindrically confined block copolymers. For example, a phase diagram of cylindrically confined block copolymers needs to be constructed experimentally. The variables include the molecular weight, composition, the interaction between the blocks and that between the blocks and shell material, and the size of the block copolymer core.
2. It is interesting to study the self-assembly of homopolymer blend, block

copolymer/homopolymer, block copolymer/block copolymer blends under cylindrical confinement. It has been demonstrated that adding homopolymer to a block copolymer can cause a phase transition in bulk. Similarly, in electrospun fibers, it has been shown that a blend of PS-PDMS-G1 and PS forms spherical morphology, as illustrated in Figure 13-1. Therefore, by blending homopolymer, different morphologies can be studied using the same block copolymer. Actually block copolymer/homopolymer blend under spherical confinement has been studied more than a decade ago by Reffner.[94] There are two other interesting ideas worth trying. First, in a macrophase separated blend of two block copolymers of the same monomers but different molecular weight, which one is in the center (or the interface with the shell)? Second, in a macrophase separated blend of homopolymer (A)/block copolymer (A-B)/homopolymer (B), can the cylindrical confinement induce miscibility? Miscibility has been demonstrated in thin film case.[136]

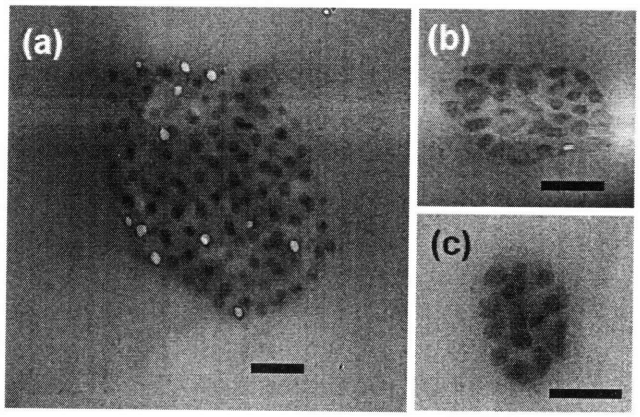

Figure 13-1 Cylindrically confined block copolymer/homopolymer blend. (a)-(c), TEM images of a blend of PS-PDMS-G1 and PS (Mw=5.11 kDa) with a weight ratio (PS-PDMS-G1/PS) of 1/2 confined in fibers with PMAA as the shell.

3. The effect of surface energy on the self-assembly of cylindrically confined block copolymers needs to be further explored. The coaxial electrospinning method followed by annealing described in this dissertation is a quite general strategy to study cylindrically confined block copolymers. The effect of interaction between the confining wall and the block copolymer on its phase behavior can be explored by simply choosing different core or shell materials.
4. Dispersing nanoparticles uniformly in electrospun fibers in a controlled manner has many practical applications. Previous work on this is not successful because of the difficulty to disperse the nanoparticles into polymer solutions homogeneously. Using block copolymer microphase separation, it is possible to not only disperse the nanoparticles into fibers but also control the location of the particles. It has been shown that in bulk or thin films, nanoparticles segregate either to one phase or the interfaces between phases, depending on the size and surface chemistry of nanoparticles.[81] Figure 13-2 shows some preliminary results for block copolymer/nanoparticle composite fibers.

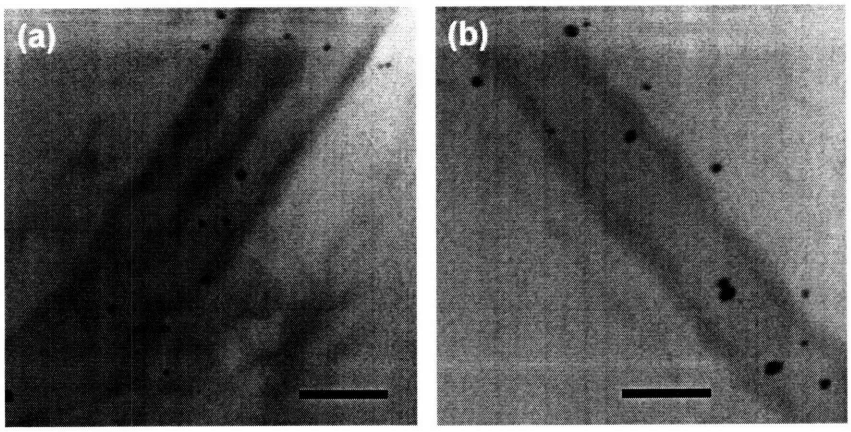

Figure 13-2 Incorporating nanoparticles into block copolymer fibers. (a) and (b), TEM images of PS-PDMS-L1 core containing dodecanethiol functionalized Au

nanoparticles. The particles are expected to segregate to PS phase.

Electrospinning is an exciting technique that produces very useful materials. Tailoring the nanostructures of the fibers hugely expands their applications. There are other opportunities for nanostructured electrospun fibers in general. Recommendations are made as well in the areas the author has started exploring but has not been able to finish.

1. Incorporating nano-objects into electrospun fibers

Incorporating nanoparticles or nanotubes into fibers can improve their mechanical, electrical and other properties. However, to achieve a high concentration of these nano-objects in fibers is challenge. Surface functionalization to promote hydrogen bonding or chemical bond between the nano-objects and fiber polymer is probably one way to meet the challenge. One preliminary example is shown in Figure 13-3 where hydrogen bonding may form between –COOH functionalized carbon nanotubes and poly(ethylene oxide).

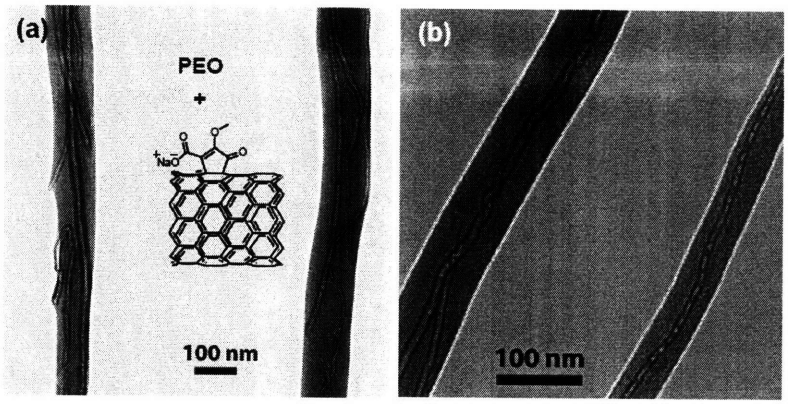

Figure 13-3 TEM images of PEO electrospun fibers containing functionalized multi-wall carbon nanotubes. (The carbon nanotubes were provided by Dr. Wei Zhang in Prof. Swager Group.)

2. Applying electron/proton conducting polymer coatings

One interesting and useful property for electrospun fibers is their free-standing feature and extremely high surface area. This material coated with conducting polymers may be used in many areas such as electromagnetic inference (EMI) shielding, proton exchange membrane[137] and electrodes for fuel cells or batteries.

Appendix I Electrospun Mats Decorated with Functional Nanoparticles

Decorating electrospun mats with nanoparticles is a versatile way to increase further the surface area of electrospun mats and enhance their properties. Besides improving the robustness of the superhydrophobic property of electrospun mats as discussed in the main text, the nanoparticles immobilized on electrospun fibers may also bring unique functionalities to the mats. Two examples are presented here to illustrate the author's efforts in this regard.

AI.1 Antimicrobial Electrospun Mats

In an unpublished collaboration with Xiaoxia Sheng from Prof. Robert Cohen Group and Prof. Michael Rubner Group and Alex Hsieh from Arm Research Lab (ARL), poly(methyl methacrylate-*co*-methacrylic acid) P(MMA-*r*-MAA) random copolymer fibers coated with silver nanoparticles were demonstrated to exhibit excellent antimicrobial property against both Gram-positive strain (*S. epidermidis*) and Gram-negative strain (*E. coli*) bacteria. In the coating process, the fiber mats were first immersed into a 5 mM silver acetate aqueous solution for 15 min, where free acid protons of MAA were exchanged for silver cations. After water rinsing, the Ag^+-loaded mats were then dipped into a 5 mM aqueous solution borane dimethylamine complex DMAB ($(CH_3)_2NH{\bullet}BH_3$) for 15 sec, resulting an Ag nanoparticle coated fiber mats. Here we use random copolymer of MMA and MAA because MAA component provides the necessary –COOH groups while MMA

component ensures the fibers are not soluble in water. The appearance of the fiber mats with different MMA/MAA ratios after Ag nanoparticle coatings is shown in Figure AI-1 (a). It is clear that the mats have a brownish color and the darkness of the color increases as the MAA ratio increases, indicating more Ag coating, as expected. Figure AI-1 (b) shows a SEM image for a copolymer fiber mat with MMA/MAA weight ratio of 40/60, which suggests that the nanoparticle coating is conformal. The cross sectional transmission electron microscopy (TEM) image in the inset demonstrates that the nanoparticles (20-30 nm) are uniformly distributed on the surface of the fibers (600-800 nm). The antibacterial property of the fiber mats with different MMA/MAA ratios is shown in Figure AI-1 (c). The antimicrobial property was evaluated by using the disk-diffusion test (also known as the Kirby-Bauer method) in which the fiber mats (deposited on round cover slips) were placed atop bacteria inoculated agar plates and incubated at 37 °C for 24 h; circular zones (zone of inhibition, or ZoI) where the bacterial growth was completely inhibited were measured. The area of the ZoI suggests that the mats with higher MAA ratio generally have higher antibacterial property, as expected again.

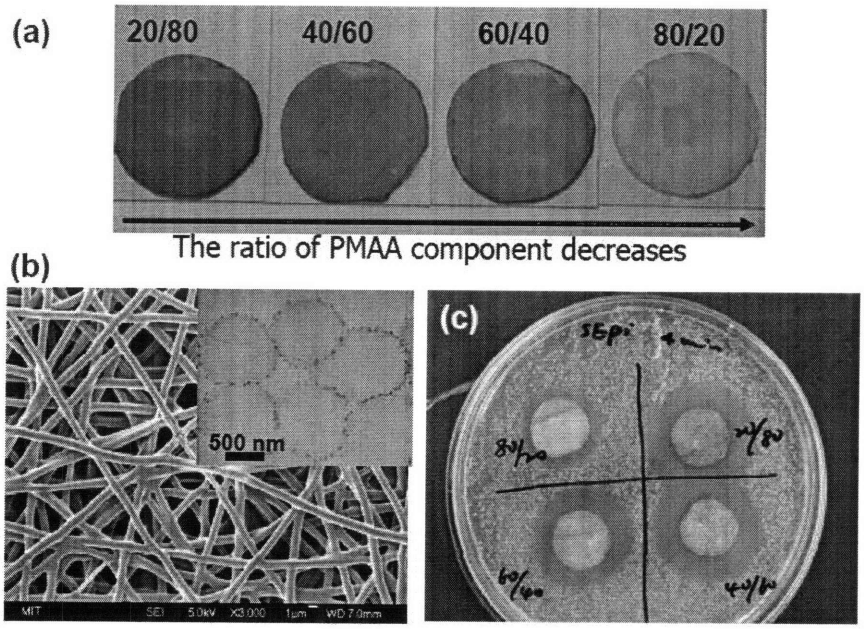

Figure AI-1 Antimicrobial property of Ag nanoparticle coated P(MMA-*r*-MAA) random copolymer fibers. (a) Photos of the coated fibers with different MMA/MAA ratios. (b) SEM image of the fibers with MMA/MAA ratio of 40/60; the inset is a TEM image showing the axial views of the fibers; the dark dots surrounding the fibers are Ag nanoparticles. (c) A photo of the *S. epidermidis* bacteria cultured in a petri dish in the presence of the Ag coated electrospun fiber mats. The MMA/MAA ratios are labeled on the photo.

AI.2 Photo-catalytic Electrospun Mats

The second example for functional nanoparticle coating is titania (TiO_2) nanoparticles coated on electrospun fibers which exhibit photo-catalytic property. Anatase crystalline TiO_2 is a well-known material that can convert O_2 to highly reactive O_2^- under UV irradiation and subsequently decompose harmful toxic organic chemicals. However, immobilization of TiO_2 with large surface area and high reactivity is still challenging. In collaboration with Jung Ah Lee from Prof. Paula Hammond Group and Prof. Gregory Rutledge Group, we have demonstrated a simple method to prepare highly photo-catalytic TiO_2 nanoparticles decorated on electrospun

fibers using LBL assembly of TiO_2 and silica (POSS) nanoparticles. The TiO_2 nanoparticles were synthesized by combining a solution of 1 part tetrabutyl ammonium hydroxide and 50 parts ethanol with a solution of 1 part titanium isopropoxide and 6 parts ethanol by volume. The combined solution was then slowly diluted with Milli-Q water to 4 times its original volume under rapid stirring and refluxed for 3 days at 98 °C. The mean diameter and Zeta-potential of stabilized TiO_2 nanoparticles are 7 nm and -34 mV, respectively. Electrospun poly(dimethylsiloxane-*r*-etherimide) random copolymer (PSEI, Gelest) fibers treated with 1 minute air plasma were then alternately dipped into the synthesized negatively charged TiO_2 nanoparticle aqueous solution and positively charged octa(3-ammoniumpropyl) octasilsesquioxane octachloride (POSS-$NH3^+$, Hybrid Plastics) solution. This LBL deposition was repeated 5 times and dipping time for each solution was 30 minutes. The nanoparticle coated fibers were characterized by SEM, TEM and XPS (Figure AI-2 a-d). The photo-catalytic activity of the TiO_2 coated electrospun fibers was tested using allyl alcohol as a model toxic chemical. The mass flux of allyl alcohol as permeation time with and without UV light is shown in Figure AI-2 (e). It clearly shows that a large mass flux peak is detected in the dark environment, while under UV light only a small and narrow peak appears and then completely disappears after about 125 seconds. This indicates the effective degradation of the chemical under UV light. To demonstrate the generality of this coating process to make photo-catalytic fiber mats, electrospun fibers made from other polymers were also used as the substrate for the LBL nanoparticle coating.

Representative TEM images are shown in Figure AI-2 (f)-(i).

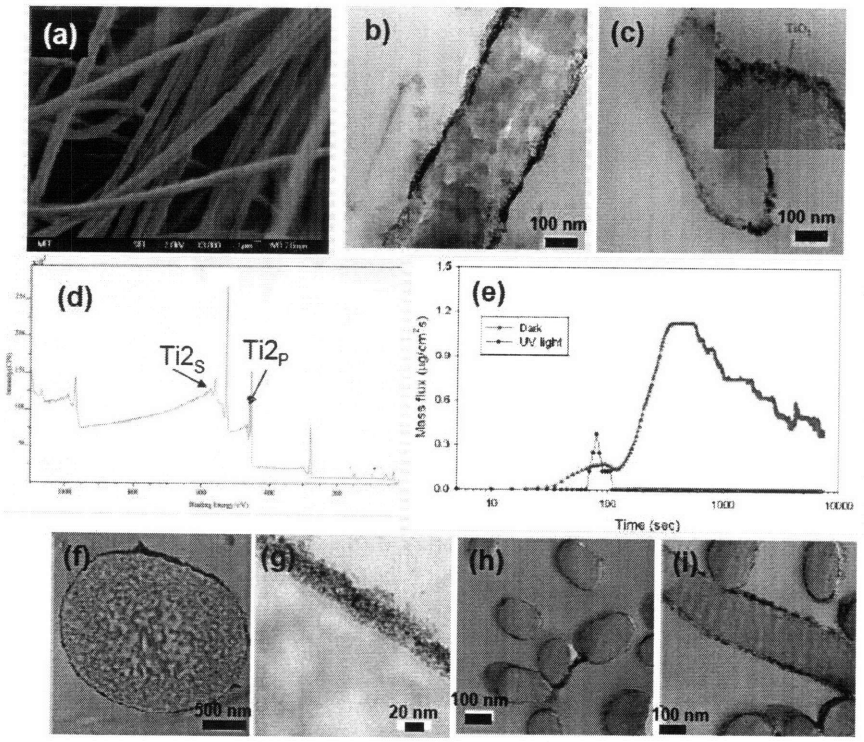

Figure AI-2 Photo-catalytic property of TiO_2 nanoparticle coated electrospun fibers. (a), SEM image of electrospun PSEI fibers. (b) and (c), TEM images (longitudinal and axial views) of the TiO_2 nanoparticle coated fibers. The inset is a magnified image of a part on the fiber surface. The dark dots on the fiber surface are TiO_2 nanoparticles. (d), XPS spectrum of the coated fibers, confirming the presence of TiO_2. (e), Mass flux of allyl alcohol that diffuses through a TiO_2 coated fiber mat with and without UV illumination for 2 hours. (f) and (g), TEM images of TiO_2 coated PS fibers. (h) and (i), TEM images of TiO_2 coated PAN fibers.

Appendix II Multifunctional Superhydrophobic Surfaces

Superhydrophobic surfaces found in nature are often associated with other properties. For example, the superhydrophobic behavior of rice leaves *(Oryza sativa)* is anisotropic and water droplets roll off much more readily in one direction than another. [138] Anisotropic surfaces similar to the rice leaf can be made by simply aligning electrospun fibers, as will be described below. Superhydrophobic membranes in the form of an electrospun fiber mat may have many advantages over conventional thin film coatings on a solid surface. For example, fiber membranes are free-standing, flexible and breathable. Gu *et al.*[139] have demonstrated that light shielding can be realized in electrospun fiber mats. They found that a 200 μm thick PS mat could attenuate light transmission by 75-80% in the range from the visible to NIR region. Other functionalities such as conductivity [140] and structural color can also be incorporated into a superhydrophobic membrane composed of electrospun fibers; these multifunctional capabilities may permit application of superhydrophobic membranes based on fibers over a much wider range than conventional superhydrophobic surfaces.[141]

AII.1 Superhydrophobic Surface with Anisotropic Property

Anisotropic surfaces consisting of aligned electrospun fibers can be made using

parallel electrodes as the collecting substrate. [142] Such surfaces can, in principle, exhibit anisotropic wetting behavior. As a proof of principle, we have electrospun fibers of polyacrylonitrile (PAN) between parallel electrodes; the fibers were then transferred to a glass slide and coated with PPFEMA using iCVD. An optical microscopy image of the surface is shown in Figure AII-1 (a). The contact angles were measured in directions both parallel and transverse to the fiber axes on the surface, before and after PPFEMA coating. Before coating, the surface was wetted completely by the water droplet, and contact angles in both directions were zero. However, the wetted area is elliptical, i.e. anisotropic, with the major axis of the ellipse being parallel to the fibers, as evident from the different cross sections of wetted area shown in Figure AII-1 (b) when viewed from different directions. After coating, the surface exhibited superhydrophobic behavior with a water contact angle of 153° and a threshold sliding angle of 8° in the direction parallel to fiber axis, and a non-superhydrophobic behavior (θ^* = 119°) in the perpendicular direction; the anisotropy in contact angle is shown in Figure AII-1 (c). The anisotropy is probably due to differences in contact lines formed parallel and perpendicular to the fibers, the latter being more composite-like in nature. The sliding angle also varies with direction, due to the fact that the droplet has to overcome an energy barrier to spread from fiber to fiber in the direction perpendicular to the fibers, while there is no such barrier to spreading along the fibers. Additionally, as the density of fibers increased or the space between fibers decreased, the contact angles after coating in both directions increased and the difference between them became much smaller.

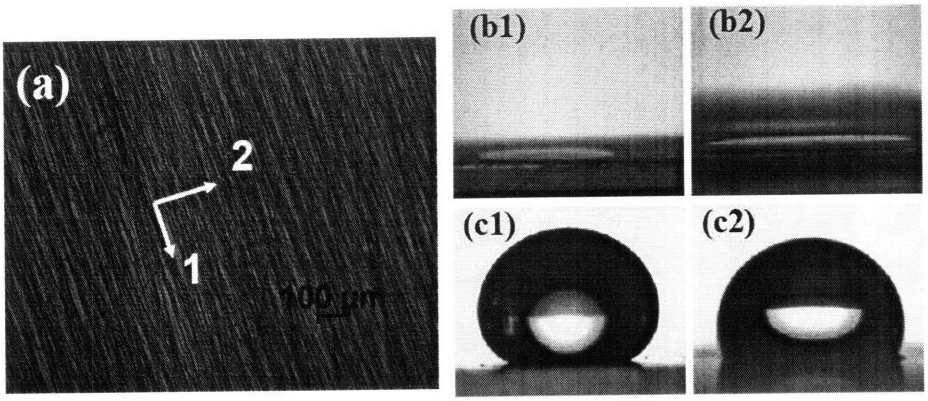

Figure AII-1 Anisotropic surface based on electrospun fibers. (a) Optical micrograph of a glass slide covered by a low density of aligned PAN electrospun fibers. (b) Photos of water droplet on the uncoated surface taken from direction 1 and 2 as indicated in (a). The bright regions are the wetted areas. (c) Photos of the droplet on the surface coated with PPFEMA taken from direction 1 and 2.

AII.2 Superhydrophobic Surface with Structural Color

Another example of a multifunctional surface in nature is the butterfly wing. It is superhydrophobic and water repellent due to microstructures on the surface. [143] These structures also give rise to beautiful colors. These so-called structural colors are produced by light interference, diffraction and scattering rather than by selective absorption or emission of light. [144] Gu *et al.* [145] mimicked the butterfly wing by making inverse opal films with both structural color and superhydrophobic properties based on colloidal self-assembly. Here, we demonstrate the same effect using electrospun fibers. Figure AII-2 (a) shows a photograph of two water droplets on PPFEMA-coated electrospun fibers on a glass slide, where the reddish color resulted from the light scattering by fibers is also reflected in the droplets. The fibers were made by electrospinning a phenylsiloxane resin/PMMA copolymer in DMF. The

fibers were then transferred to a glass slide and coated with PPFEMA (nominally ~30 nm thick coating). The average fiber diameter before PPFEMA coating was 1.24 μm with a standard deviation of 0.08 μm. The fibrous surface after coating exhibits superhydrophobicity with contact angle of 163° and hysteresis of 7°. The color observed for these fibers is believed to be due to the effect of Mie scattering. [146] To understand this structural color exhibited by electrospun fibers, preliminary theoretical calculations based on light scattering by infinitely long cylinder were performed. In general, when the light wavelength is similar to the particle size, light interacts with the particle over a cross-sectional area C_{sca} larger than the geometric cross section of the particle, G. The ratio of the two areas is a dimensionless scattering efficiency parameter, Q_{sca}. The scattering efficiency for a long fiber, assuming the incident light perpendicular to the fiber axis, can be calculated as following:

$$b_n = \frac{J_n(mx)J_n'(x) - mJ_n'(mx)J_n(x)}{J_n(mx)H_n^{(1)'}(x) - mJ_n'(mx)H_n^{(1)}(x)}$$

$$Q_{sca//} = \frac{2}{x}(|b_0|^2 + 2\sum_{n=1}^{\infty}|b_n|^2)$$

$$a_n = \frac{mJ_n(mx)J_n'(x) - J_n'(mx)J_n(x)}{mJ_n(mx)H_n^{(1)'}(x) - J_n'(mx)H_n^{(1)}(x)}$$

$$Q_{sca\perp} = \frac{2}{x}(|a_0|^2 + 2\sum_{n=1}^{\infty}|a_n|^2)$$

$$Q_{sca} = \frac{1}{2}(Q_{sca\parallel} + Q_{sca\perp})$$

where, $x = kb$ with b as the radius of the fiber and $k = 2\pi/\lambda$ as the wave number; m is the refractive index of the fiber material; a_n and b_n are scattering coefficients; J_n is Bessel functions of 1st kind; $H_n^{(1)} = J_n + iY_n$ with Y_n as the Bessel functions of 2nd

kind.

Figure AII-2 (b) is the calculation result for m = 1.5 and b = 0.6 μm which indeed shows different scattering efficiency at different wavelength in the visible range. It is difficult to compare this spectrum directly to the color observed, since the model is based on a single fiber, while the color observed is a collective result of fibers with different orientation and sizes. That is also why a thick electrospun fiber mat has the white appearance, a result of multi-wavelength scattering.

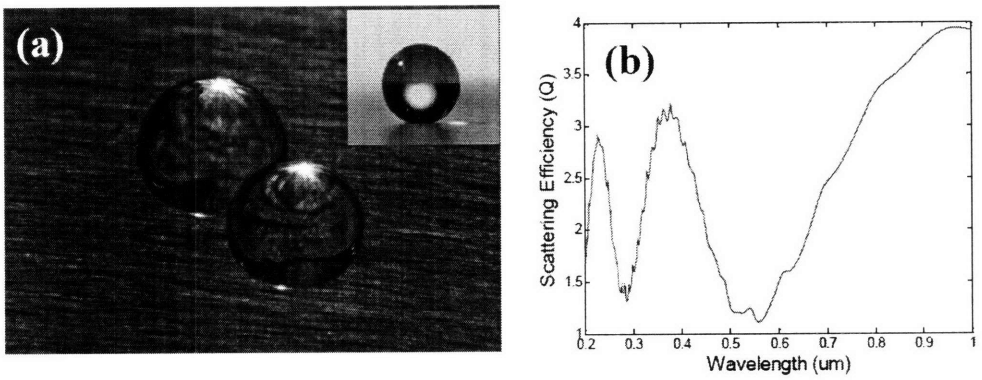

Figure AII-2 Superhydrophobic surface exhibiting structural color. (a), A digital image of water droplets on a colorful superhydrophobic surface composed of electrospun fibers on a piece of glass slide. The picture was taken from a nearly normal direction with a white light source beneath the slide. The inset is a contact angle measurement. (b), Calculated scattering spectrum based on normal illumination on an infinitely long cylinder with a diameter of 1.2 μm.

The structural color exhibited by electrospun fibers can be easily adjusted by varying the refractive index of the fiber material or the fiber diameter within a limited range. Figure AII-3 shows three fiber samples with different fiber sizes, exhibiting different colors. However, not all fibers could have structural colors. Preliminary calculations based on the Mie scattering model described above show that fibers with too small (diameter < 600 nm) or too large (diameter > 10 μm) sizes do not have

unique scattering peaks or valleys within visible wavelength and therefore structural colors. (Figure AII-4) The structurally colored fibers may have a number of important applications. Examples include anti-counterfeiting and other document security applications, sensing technologies including passive sensors that exhibit a visible color change in response to an environmental change such as exposure to chemical toxins, light filtering, reducing IR signature of persons, systems and other objects and appearance shifting smart textiles.

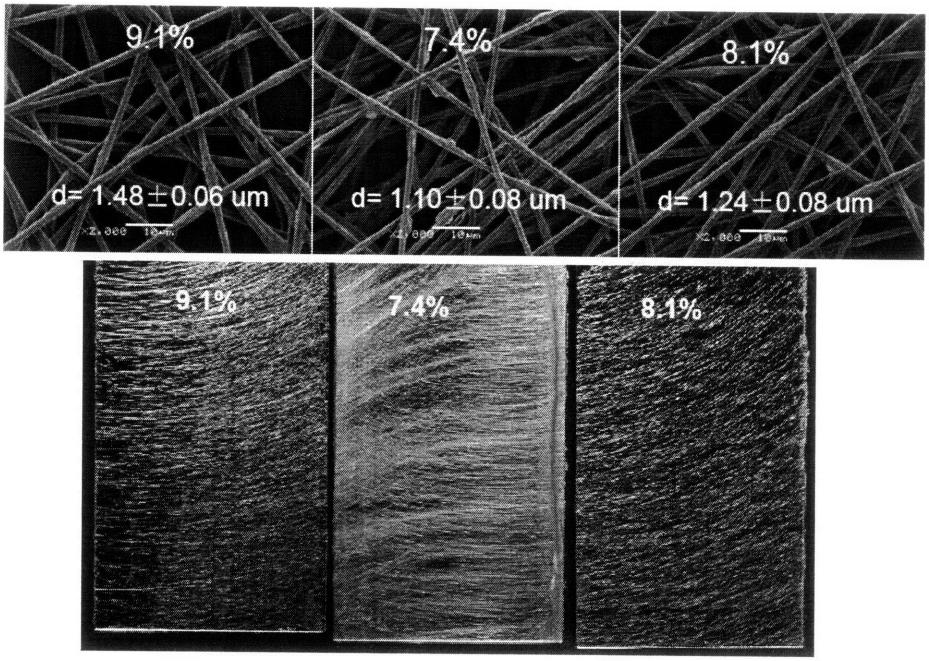

Figure AII-3 Electrospun fibers with different fiber sizes exhibiting different colors. The colors are observed from nearly normal direction. The concentration of the solutions from which the fibers were made and the corresponding fiber diameters are labeled.

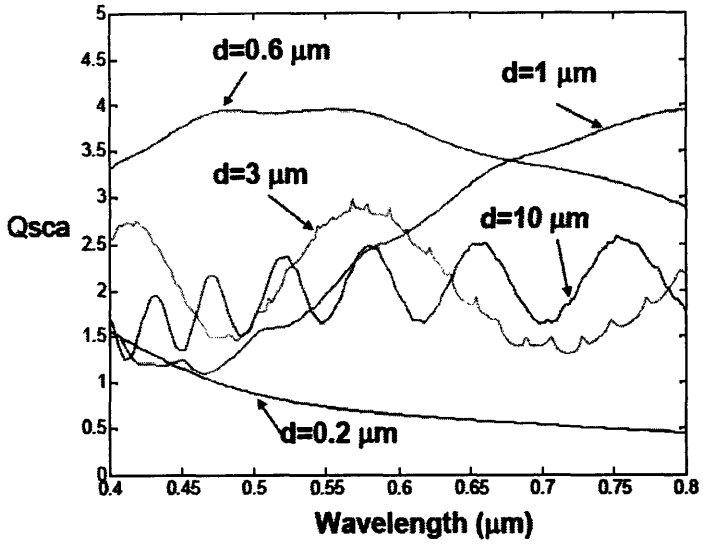

Figure AII-4 Calculated scattering spectra based on normal illumination on an infinitely long cylinder. The diameters for each cylinder are labeled. Note that cylinders with d =0.2 μm and d = 0.6 μm have no strong scattering peak while the one with d = 10 μm has too many peaks in the range of visible wavelength.

AII.3 Superhydrophobic Surfaces with Optical Functionalities

Incorporating optical functionalities into superhydrophobic surfaces considerably enlarges their applications. In this section, two functional superhydrophobic surfaces will be described briefly, one with transparency and the other with fluorescence. Both surfaces were made by electrospraying, a process to make micro/nano particles as introduced in Chapter 1. The transparent superhydrophobic surfaces were obtained by electrospraying a dilute (1 wt%) polyacrylonitrile (PAN)/DMF solution onto transparent glass substrates followed by a PPFEMA coating using iCVD. The electrosprayed PAN nanoparticle thin layer coatings have sufficient surface roughness for superhydrophobicity while maintaining the transparence of the glass substrates due to the relatively low light absorption and scattering. Figure AII-5 shows three

glass slides coated with different amounts of PAN nanoparticles. It is clear that as the amounts of nanoparticle increases, the surface roughness increases, evidenced by the higher contact angles, but the light scattering also becomes severer, indicated by the decreasing transparence.

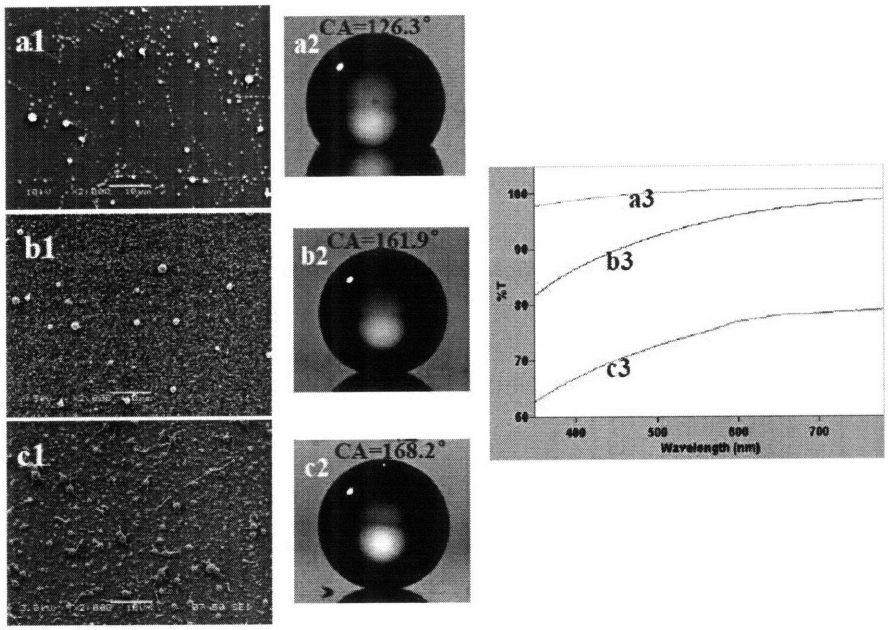

Figure AII-5 Superhydrophobicity and transparency are two competing material properties. SEM images, contact angles and transmittance for three glass slides (a, b and c) coated with different amount of nanoparticles.

Thus, in order to make a superhydrophobic and transparent surface, the surface roughness must be optimized. Figure AII-6 shows an example where the roughness was tuned such that both the transparence and hydrophobicity are high.

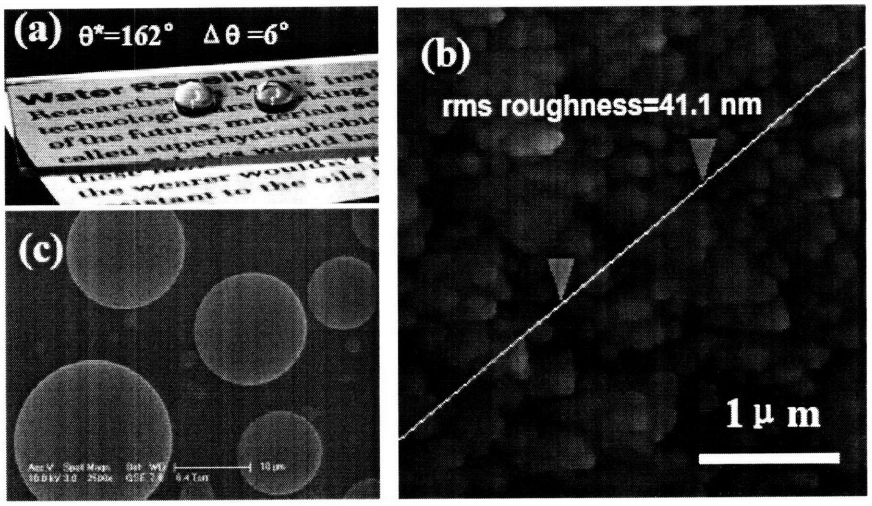

Figure AII-6 A transparent superhydrophobic surface made by electrospraying and iCVD. (a) A digital photo of the surface; (b) AFM height image of the surface; (c) ESEM image of water droplets condensed on the surface.

The superhydrophobic surface with fluorescent property was made in a single step by electrospraying a phenyleneethynylene[147] conjugated polymer (PPE) solution (1.2 wt%) in chloroform. SEM images in Figure AII-7 show that these particles do not have round shapes but irregular hat-like appearance. The mechanisms for the formation of these collapsed particles and the nanopore structure on the particle surface are similar to the case of fibers as discussed in Chapter 6.

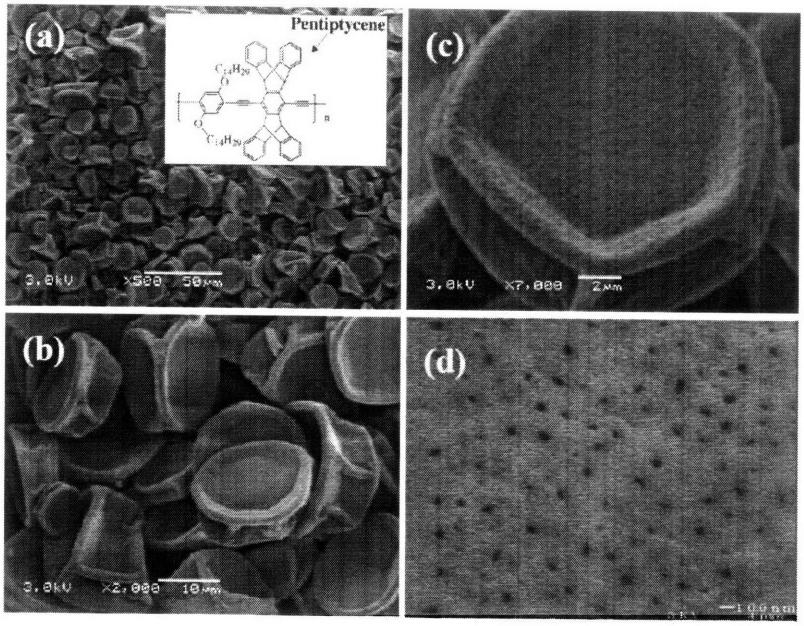

Figure AII-7 SEM images with different magnifications of PPE electrosprayed microparticles. The inset of (a) shows the molecular structure of PPE. (d) is a magnified part of the particle surface, showing the porous structure.

The fluorescent property of the electrosprayed PPE particles is shown by the fluorescence microscopy image in Figure AII-8 (a). Figure AII-8 (b) shows two water droplets on the surface composed of microparticles of this intrinsically fluorescent polymer under the radiation of UV light. The contact angle on the surface as shown in the inset of Figure AII-8 (b) is 164.5°. Water moves spontaneously on the surface with little tilted angle (less than 1°). The threshold sliding angle is as low as 3.4°. The superhydrophobicity of this PPE particle-composed surface is actually a surprising result, since the PPE itself is intrinsically hydrophilic. The contact angle for a smooth PPE film is about 70°. This result confirms again that superhydrophobic surface can be made from hydrophilic materials by designing proper surface structures such as those with "re-entrant" curvature[41], as discussed in Chapter 5.

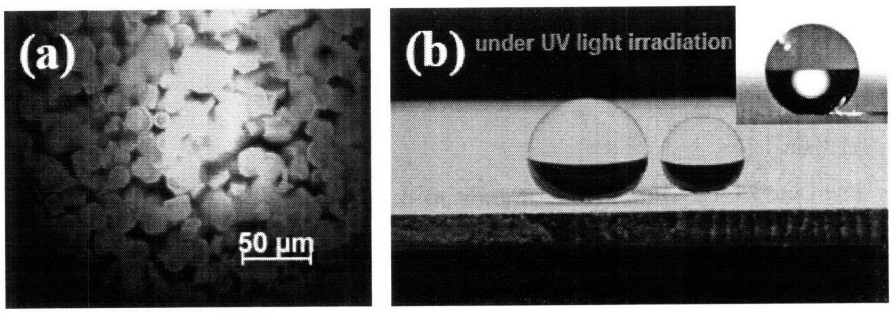

Figure AII-8 A fluorescent superhydrophobic surface made by electrospraying in one single step. (a), Fluorescent microscopy image of the PPE particles, showing the shining green color; (b), Two water droplets on the PPE particle coated surface under UV illumination. The inset is the contact angle measurement.

To improve the mechanical integrity of the particle-composed surface, thermal annealing was applied. Figure AII-9 shows SEM images of the surface after annealing at 150°C for 1 hour. The particles are partially fused without a significant change of particle morphology and surface roughness. The thermally annealed surface becomes more robust because the particles are welded together and bound to the substrate. The contact angle measurement indicates that the superhydrophobicity of the surface is maintained after thermal annealing, with a contact angle of 162.3° and a sliding angle of 3.9°.

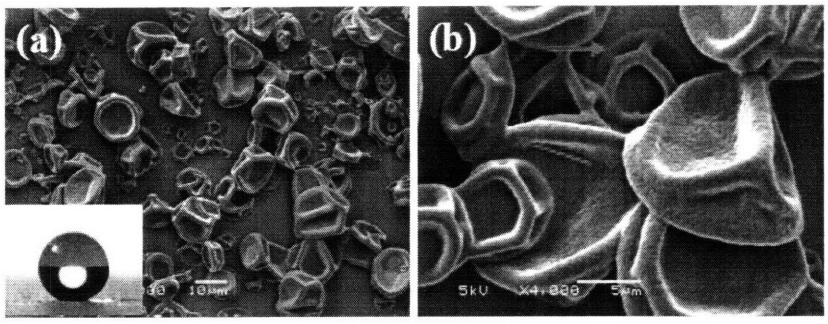

Figure AII-9 Enhancing mechanical integrity of the PPE particle surface by thermal annealing. (a) and (b), SEM images for the PPE particles after thermal annealing. The inset in (a) is the contact angle measurement; the arrows in (b) indicate the particles are welded together with each other and the substrate.

Notations and Abbreviations

Units

m (cm, mm, μm, nm)	meter (centimeter, millimeter, micrometer, nanometer)
μL	microliter
ml/min	milliliter per minute
mN/m	milli-Newton per meter
kDa	kilogram per mole
s (min, h)	second (minute, hour)
torr	pressure unit, 1/760 an atmosphere
M (mM)	mole per liter (milli-mole per liter)
sccm	standard cubic centimeters per minute
g/cm^2	gram per centimeter square
wt%	percentage by weight
kV	Kilovolt
S/cm	simen per centimeter

Chemicals

DMAB	borane dimethylamine complex
DMF	*N,N*-dimethylformamide
HFIP	1,1,1,3,3,3-hexafluoro-2-propanol
NDSA	1,5-naphthalenedisulfonic acid
PFEMA	perfluoroalkyl ethyl methacrylate
POSS	polyhedral oligomeric silsesquioxane
TBAC	tetrabutylammonium chloride
THF	Tetrahydrofuran
Nylon-6	poly(caprolactam)
PAH	poly(allylamine hydrochloride)
PAN	poly(acrylonitrile)
PC	poly(carbonate)
PCL	poly(caprolactone)
PDMS	poly(dimethyl siloxane)
PDAC	poly(diallyl dimethyl ammonium chloride)
PEDOT	poly(3,4-ethylenedioxythiophene)
PEG	poly(ethylene glycol)
PEO	poly(ethylene oxide)
PMAA	poly(methacrylic acid)
PMMA	poly(methyl methacrylate)
P(MMA-*r*-MAA)	poly(methyl methacrylate-*co*- methacrylic acid)
PNIPAM	poly(*N*-isopropylacrylamide)
PPE	poly(phenyleneethynylene)
PPFEMA	poly(perfluoroalkyl ethyl methacrylate)

PS	poly(styrene)
PSEI	poly(dimethylsiloxane-*co*-etherimide)
PS-PDMS	poly(styrene-*b*-dimethyl siloxane)
PS-PI	poly(styrene-*b*-isoprene)
PS-PI-PS	poly(styrene-*b*-isoprene-*b*-styrene)

Variables

Q	flow rate
V	Voltage
Z	electrode-to-electrode distance
S	spreading coefficient
γ_{LG}, γ_{SG}, γ_{LS}	interfacial tensions of liquid-gas, solid-gas and solid-liquid
γ_S	surface tension of a solid
θ (θ_Y)	intrinsic (Young's) contact angle
θ_a (θ_r)	advancing (receding) contact angle
$\Delta\theta$	contact angle hysteresis
θ^*	apparent contact angle
θ_c	critical contact angle at Wenzel-Cassie transition
r	roughness ratio
ϕ_s (ϕ_v)	solid-liquid (vapor-liquid) contact area fraction
d	fiber diameter
s	fiber-to-fiber distance
ρ	liquid density
l_{cap}	capillary length
g	gravity constant
h_1	distance from liquid-gas interface to the next level of fibers
h_2	sagging distance
H^*	robustness parameter
b	radius of fibers
Q_{sca}	scattering efficiency
L_0	block copolymer period
χ	flory interaction parameter
P	degree of polymerization
f	volume fraction in a block copolymer
a	statistical segmental length
t	thickness of block copolymer thin film
D	diameter of the block copolymer core
N	number of bilayers in lamella-forming block copolymer
c_i	interfacial chain density at the i^{th} interface
λ_0	volume chain density
d_n	domain width of n^{th} domain from the center
r_i	radius of the i^{th} interface

References

[1] W. J. Morton, Methods of dispersing fluids. US Patent, 705, 691 (1902).

[2] A. Formhals, Processing and apparatus for preparing artificial threads. US Patent, 2, 077, 373 (1934).

[3] J. Doshi, D. H. Reneker, Electrospinning process and applications of electrospun fibers. *J. Electrostat.* 35, 151 (1995).

[4] J. Zeleny, The electrical discharge from liquid points, and a hydrostatic method of measuring electric intensity at their surfaces. *Phys. Rev.* 3, 69 (1914).

[5] G. I. Taylor, Electrically driven jets. *Proc. R. Soc. Lond., Ser. A* 313, 453 (1969).

[6] L. Rayleigh, *Proc. R. Soc. Lon.*, 14, 184 (1882).

[7] M. M. Hohman, M. Shin, G. C. Rutledge, M. P. Brenner, Electrospinning and electrically forced jets. I. Stability theory. *Phys. Fluid* 13, 2201 (2001).

[8] D. H. Reneker, A. L. Yarin, H. Fong, S. Koombhongse, Bending instability of electrically charged liquid jets of polymer solutions in electrospinning. *J. Appl. Phys.* 87, 4531 (2000).

[9] S. V. Fridrikh, J. H. Yu, M. P. Brenner, G. C. Rutledge, Controlling the fiber diameter during electrospinning. *Phys. Rev. Lett.* 90, 144502 (2003).

[10] G. C. Rutledge and S. V. Fridrikh, Formation of fibers by electrospinning. *Adv. Drug Deliver Rev.* 59, 1384 (2007).

[11] M. Y. Shin, M. M. Hohman, M. P. Brenner, G. C. Rutledge, Experimental characterization of electrospinning: the electrically force jet and instabilities. *Polymer* 42, 9955 (2001).

[12] A. Greiner and J. H. Wendorff, Electrospinning: A Fascinating Method for Preparation of Ultrathin Fibers, *Angew. Chem. Int. Ed. 46*, 5670 (2007).

[13] M. Bognitzki, W. Czado, T. Frese, A. Schaper, M. Hellwig, M. Steinhart, A. Greiner, J. H. Wendorff, Nanostructured fibers via electrospinning. *Adv. Mater.* 13, 70 (2001).

[14] M. Wang, A. J. Hsieh, G. C. Rutledge, Electrospinning of poly(MMA-co-MAA) copolymers and their layered silicate nanocomposites for improved thermal properties. *Polymer 46*, 3407 (2005).

[15] F. Ko, Y. Gogotsi, A. Ali, N. Naguib, H. Ye, G. L. Yang, C. Li, P. Willis,

Electrospinning of continuous carbon nanotube-filled nanofiber yarns. *Adv. Mater. 15*, 1161 (2003).

[16] M. Wang, H. Singh, T. A. Hatton, G. C. Rutledge, Field-responsive superparamagnetic composite nanofibers by electrospinning. *Polymer 45*, 5505 (2004).

[17] A. Melaiye, Z. Sun, K. Hindi, A. Milsted, D. Ely, D. H. Reneker, C. A. Tessier, W. J. Youngs, Silver(I)-imidazole cyclophane *gem*-diol complexes encapsulated by electrospun tecophilic nanofibers: formation of nanosilver particles and antimicrobial activity. *J. Am. Chem. Soc. 127*, 2285 (2005).

[18] J. S. Stephens, D. B. Chase, J. F. Rabolt, Effect of the electrospinning process on polymer crystallization chain conformation in Nylon-6 and Nylon-12. *Macromolecules* 37, 877 (2004).

[19] M. Bognitzki, T. Frese, M. Steinhart, A. Greiner, J. H. Wendorff, Preparation of fibers with nanoscaled morphologies: electrospinning of polymer blends. *Polym. Eng. Sci.* 41, 982 (2001).

[20] C. Kim, Y. I. Jeong, B. T. N. Ngoc, K. S. Yang, M. Kojima, Y. A. Kim, M. Endo, J-W. Lee, Synthesis and characterization of porous carbon nanofibers with hollow cores through the thermal treatment of electrospun copolymeric nanofiber web. *Small* 3, 91 (2007).

[21] P. G. de Gennes, Wetting: statics and dynamics, *Reviews of Modern Physics* 57, 827 (1985).

[22] M. Ma, R. M. Hill, Superhydrophobic surfaces. *Curr. Opin. Colloid Interface Sci.* 11, 193 (2006).

[23] T. Nishino, M. Meguro, K. Nakamea, M. Matsushita, Y. Ueda, The lowest surface free energy based on $-CF_3$ alignment. *Langmuir 15*, 4321 (1999).

[24] N. K. Adam, *Physics and Chemistry of Surfaces*, Third Edition, Oxford (1941).

[25] R. N. Wenzel, Resistance of solid surfaces to wetting by water. *Ind. Eng. Chem.* 28, 988 (1936).

[26] R. N. Wenzel, The evaluation of textile waterproofing agents. *Am Dyest Rep.* 25, 505 (1936).

[27] A. B. D. Cassie, Contact angles. *Discuss. Faraday Soc.* No. 3, 11 (1948).

[28] S. Baxter, A. B. D. Cassie, The water repellency of fabrics and a new water-repellency test. *J Text I* 36, T67 (1945).

[29] A. B. D. Cassie and S. Baxter, Wettability of porous surfaces. *Trans. Faraday Soc.* 40, 546 (1944).

[30] R. E. Johnson Jr. and R. H. Dettre, Contact angle hysteresis. *Adv. Chem. Ser.* 43, 112 and 136 (1964).

[31] M. Nosonovsky, On the range of applicability of the Wenzel and Cassie Equations. *Langmuir* 23, 9919 (2007).

[32] M. V. Panchagnula, S. Vedantam, Comment on how Wenzel and Cassie were wrong by Gao and McCarthy. *Langmuir* 23, 13242 (2007).

[33] A. Lafuma, D. Quere, Superhydrophobic states. *Natuer Mater.* 2, 457 (2003).

[34] D. Quere, M. Reyssat, Non-adhesive lotus and other hydrophobic materials. *Phil. Trans. R. Soc. A* 366, 1539 (2008).

[35] Y-T. Cheng, D. E. Rodak, Is the lotus leaf superhydrophobic? *Appl. Phys. Lett.* 86, 144101 (2005).

[36] N. A. Patankar, On the modeling of hydrophobic contact angles on rough surfaces. *Langmuir* 19, 1249 (2003).

[37] A. Marmur, Wetting on hydrophobic rough surfaces: to be heterogeneous or not to be? *Langmuir* 19, 8343 (2003).

[38] M. Nosonovsky, B. Bhushan, Patterned nonadhesive surfaces: superhydrophobicity and wetting regime transition. *Langmuir* 24, 1525 (2008).

[39] J. Liu, X. Feng, G. Wang, S. Yu, Mechanisms of superhydrophobicity on hydrophilic substrates. *J. Phys.: Condens. Matter* 19, 356002 (2007).

[40] M. Nosonovsky, Multiscale rougness and stability of superhydrophobic biomimetic interfaces. *Langmuir* 23, 3157 (2007).

[41] A. Tuteja, W. Choi, M. Ma, J. M. Mabry, S. A. Mazzella, G. C. Rutledge, G. H. McKinley, R. E. Cohen, Designing superoleophobic surfaces. *Science* 318, 1618 (2007).

[42] D. C. Pease, The significance of the contact angle in relation to the solid surface. *J. Phys. Chem.* 49, 107 (1945).

[43] L. Gao, T. J. McCarthy, How Wenzel and Cassie were wrong. *Langmuir* 23, 3762 (2007).

[44] L. Gao, T. J. McCarthy, Contact angle hysteresis explained. *Langmuir* 22, 6234 (2006).

[45] C. W. Extrand, Contact angles and hysteresis on surfaces with chemically heterogeneous islands. *Langmuir* 19, 3793 (2003).

[46] L. Gao, T. J. Thomas, A perfectly hydrophobic surface (θ_a/θ_r=180°/180°). *J. Am. Chem. Soc.* 128, 9052 (2006).

[47] M. Ma, R. M. Hill, J. L. Lowery, S. V. Fridrikh, G. C. Rutledge, Electrospun poly(styrene-block-dimethylsiloxane) block copolymer fibers exhibiting superhydrophobicity. *Langmuir* 21, 5549 (2005).

[48] H. Lee, L. A. Archer, Functionalizing polymer surfaces by field-induced migration of copolymer additives. 1. Role of surface energy gradients. *Macromolecules* 2001, *34*, 4572.

[49] M. Ma, Y. Mao, M. Gupta, K. K. Gleason, G. C. Rutledge, Superhydrophobic fabrics produced by electrospinning and chemical vapor deposition. *Macromolecules* 38, 9742 (2005).

[50] Y. Mao, K. K. Gleason, Vapor-deposited fluorinated glycidyl copolymer thin films with low surface energy and improved mechanical properties. *Macromolecules* 39, 3895 (2006)

[51] K. J. Vahala, Optical microcavities. *Nature* 424, 839 (2003).

[52] H. Yabu, M. Takebayashi, M. Tanaka, M. Shimomura, Superhydrophobic and lipophobic properties and self-organized honeycomb and pincushion structures. *Langmuir* 2005, *21*, 3235.

[53] AATCC test method 118-1997 Technical Manual American Association of Textile Chemists and Colorists, Research Triangle Park, NC, 1996, (http://www.aatcc.org/Technical/Test_Methods/Alpha_List.htm).

[54] J. P. Youngblood, T. J. McCarthy, Ultrahydrophobic polymer surfaces prepared by simultaneous ablation of polypropylene and sputtering of poly(tetrafluoroethylene) using radio frequency plasma. *Macromolecules 32*, 6800 (1999).

[55] C. Neinhuis, W. Barthlott, Characterization and distribution of water-repellent, self-cleaning plant surfaces. *Ann. Botany* 79, 667 (1997).

[56] L. Zhai, F. C. Cebeci, R. E. Cohen, M. F. Rubner, Stable superhydrophobic coatings from polyelectrolyte multilayers. *Nano Lett.* 4, 1349 (2004).

[57] W. Ming, D. Wu, R. van Benthem, G. de With, Superhydrophobic films from Raspberry-like particles. *Nano Lett.* 5, 2298 (2005).

[58] L. Gao, T. J. McCarthy, The "Lotus effect" explained: two reasons why length scales of topography are important. *Langmuir* 22, 2966 (2006).

[59] P.-G. de Gennes, F. Brochard-Wyart, D. Quéré, in *Capillarity and Wetting Phenomena: Drops, Bubbles, Pearls, Waves*. Springer, New York 2004, Ch. 9.

[60] W. Chen, A. Y. Fadeev, M. C. Hsieh, D. Öner, J. Youngblood, T. J. McCarthy, Ultrahydrophobic and ultralyophobic surfaces: some comments and examples. *Langmuir* 15, 3395 (1999).

[61] M. Ma, Z. Li, M. Gupta, L. Zhai, K. K. Gleason, R. E. Cohen, M. F. Rubner, G. C. Rutledge, Decorating electrospun fibers for superhydrophobicity. *Adv. Mater.* 19, 255 (2007).

[62] S. Megelski, J. S. Stephens, D. B. Chase, J. F. Rabolt, Micro- and nanostructured surface morphology on electrospun polymer fibers. *Macromolecules* 2002, *35*, 8456.

[63] C. L. Casper, J. S. Stephens, N. G. Tassi, D. B. Chase, J. F. Rabolt, Controlling surface morphology of electrospun polystyrene fibers: effect of humidity and molecular weight in the electrospinning process. *Macromolecules* 2004, *37*, 573.

[64] S. Koombhongse, W. Liu, D. H. Reneker, Flat polymer ribbons and other shapes by electrospinning. *J. Polym. Sci: B. Polym. Phys.* 39, 2598 (2001).

[65] G. McHale, S. Aqil, N. J. Shirtcliffe, M. I. Newton, H. Y. Erbil, Analysis of droplet evaporation on a superhydrophobic surface. *Langmuir* 21, 11053 (2005).

[66] J. T. McCann, M. Marquez, Y. Xia, Highly porous fibers by electrospinning into a cryogenic liquid. *J. Am. Chem. Soc.* 128, 1436 (2006).

[67] D. Li, J. T. McCann, Y. Xia, Use of electrospinning to directly fabricate hollow nanofibers with functionalized inner and outer surfaces. *Small* 1, 83 (2005).

[68] G. Decher, Fuzzy nanoassemblies: toward layered polymeric multicomposites. *Science* 277, 1232 (1997).

[69] T. Soeno, K. Inokuchi, S. Shiratori, Ultra water-repellant surface resulting from complicated microstructure of SiO_2 nanoparticles. *Trans. Mater. Soc. Jpn.* 28, 1207 (2003).

[70] X. Wang, Y. G. Kim, C. Drew, B. C. Ku, J. Kumar, L. A. Samuelson, Electrostatic assembly of conjugated polymer thin layers on electrospun nanofibrous membranes for biosensors. *Nano Lett.* 4, 331 (2004).

[71] D. Quere, Rough ideas on wetting. *Physca A* 313, 32 (2002).

[72] L. Courbin, E. Denieul, E. Dressaire, M. Roper, A. Ajdari, H. A. Stone. Imbibition by polygonal spreading on microdecorated surfaces. *Nature Mater.* 6, 661 (2007).

[73] R. M. Hill, Superspreading. *Curr. Op. Colloid In.* 3, 247 (1998).

[74] T. Sun, G. Wang, L. Feng, B. Liu, Y. Ma, L. Jiang, D. Zhu, Reversible switching between superhydrophilicity and superhydrophobicity. *Angew. Chem. Int. Ed.* 43, 357 (2004).

[75] T. N. Krupenkin, J. A. Taylor, T. M. Schneider, S. Yang, From rolling ball to complete wetting: the dynamic tuning of liquids on nanostructured surfaces. *Langmuir* 20, 3824 (2004).

[76] L. Xu, W. Chen, A. Mulchandani, Y. Yan, Reversible conversion of conducting polymer films from superhydrophobic to superhydrophilic. *Angew. Chem. Int. Ed.* 44, 6009 (2005).

[77] W. Jiang, G. Wang, Y. He, X. Wang, Y. An, Y. Song, L. Jiang, Photo-switched wettability on an electrostatic self-assembly azobenzene monolayer. *Chem. Comm.* 3550 (2005).

[78] I. W. Hamley, '*The physics of block copolymers*', Oxford University Press, 1998.

[79] F. S. Bates, G. H. Fredrickson, Block copolymer thermodynamics: Theory and experiment. *Annu. Rev. Phys. Chem.* 41, 335 (1990).

[80] G. H. Fredrickson, F. S. Bates, Dynamics of block copolymers: Theory and experiments. *Annu. Rev. Mater. Sci.* 26, 501 (1996).

[81] C. Park, J. Yoon, E. L. Thomas, Enabling nanotechnology with self assembled block copolymer patterns. *Polymer* 44, 6725 (2003).

[82] S. Forster, T. Plantenberg, From self-organizing polymers to nanohybrid and biomaterials. *Angew. Chem. Int. Ed.* 41, 688 (2002).

[83] M. J. Fasolka, A. M. Mayes, Block copolymer thin films: physics and applications. *Annu. Rev. Mater. Res.* 31, 323 (2001).

[84] T. P. Russell, G. Coulon, V. R. Deline, D. C. Miller, Characteristics of the surface-induced orientation for symmetric diblock PS/PMMA copolymers. *Macromolecules* 22, 4600 (1989).

[85] P. Lambooy, T. P. Russell, G. J. Kellogg, A. M. Mayes, P. D. Gallagher, S. K. Satija, Observed frustration in confined block copolymers. *Phys. Rev. Lett.* 72, 2899 (1994).

[86] N. Koneripalli, N. Singh, R. Levicky, F. S. Bates, P. D. Gallagher, S. K. Satija, Confined block copolymer thin films. *Macromolecules* 28, 2897 (1995).

[87] D. G. Walton, G. J. Kellogg, A. M. Mayes, P. Lambooy, T. P. Russell, A free energy model for confined diblock copolymers. *Macromolecules* 27, 6225 (1994).

[88] Z. Chen, J. A. Kornfield, S. D. Smith, J. T. Grothaus, M. M. Satkowski, Pathways to macroscale order in nanostructured block copolymers. *Science* 277, 1248 (1997).

[89] T. Thurn-Albrecht, J. Schotter, G. A. Kästle, N. Emley, T. Shibauchi, L. Krusin-Elbaum, K. Guarini, C. T. Black, M. T. Tuominen, T. P. Russell, Ultrahigh-density nanowire arrays grown in self-assembled diblock copolymer templates. *Science* 290, 2126 (2000).

[90] S. O. Kim, H. H. Solak, M. P. Stoykovich, N. J. Ferrier, J. J. de Pablo, P. F. Nealey, Epitaxial self-assembly of block copolymers on lithographically defined nanopatterned substrates. *Nature* 424, 411 (2003).

[91] J. Y. Cheng, C. A. Ross, H. I. Smith, E. L. Thomas, Templated self-assembly of block copolymers: top-down helps bottom-up. *Adv. Mater. 18*, 2505 (2006).

[92] E. L. Thomas, J. R. Reffner, J. Bellare, A menagerie of interface structures in copolymer systems. *Colleque De Physique, Colleque* C7-363 (1990).

[93] A. C. Arsenault, D. A. Rider, N. Tétreault, J. I-L. Chen, N. Coombs, G. A. Ozin, I. Manners, Block copolymers under periodic, strong three-dimensional confinement. *J. Am. Chem. Soc.* 127, 9954 (2005).

[94] J. R. Reffner, The influence of surfaces on structure formation: I. Artificial epitaxy of metals on polymers. II. Phase separation of block copolymers and polymer blends under nonplanar surface constraints. PhD Thesis. University of Massachusetts, 1992.

[95] M. Okubo, N. Saito, R. Takekoh, H. Kobayashi. Morphology of polystyrene/polystyrene-block-polymer(methyl methacrylate)/poly(methyl methacrylate) composite particles. *Polymer* 46, 1151 (2005).

[96] H. Yabu, T. Higuchi, M. Shimomura, Unique phase-separation structures of block copolymer nanoparticles. *Adv. Mater.* 17, 2062 (2005).

[97] S-J. Jeon, G-R. Yi, C. M. Koo, S-M. Yang, Nanostructures inside colloidal particles of block copolymer/homopolymer blends. *Macromolecules* 40, 8430 (2007).

[98] D. A. Rider, J. I. L. Chen, J-C. Eloi, A. C. Arsenault, T. P. Russell, G. A. Ozin, I. Manners, Controlling the morphologies of organometallic block copolymers in the 3-dimentional spatial confinement of colloidal and inverse colloidal crystals. *Macromolecules* 41, 2250 (2008).

[99] X. He, M. Song, H. Liang, C. Pan, Self-assembly of the symmetric diblock copolymer in a confined state: Monte Carlo simuation. *J. Chem. Phys.* 114, 10510 (2001).

[100] J. G. E. M. Fraaije, G. J. A. Sevink, Model for pattern formation in polymer surfactant nanodroplets. *Macromolecules* 36, 7891 (2003).

[101] B. Yu, B. Li, Q. Jin, D. Ding, A-C. Shi, Self-assembly of symmetric diblock copolymers confined in spherical nanopores. *Macromolecules* 40, 9133 (2007).

[102] H. Xiang, K. Shin, T. Kim, S. I. Moon, T. J. McCarthy, T. P. Russell, Block copolymers under cylindrical confinement. *Macromolecules* 37, 5660 (2004).

[103] K. Shin, H. Xiang, S. I. Moon, T. Kim, T. J. McCarthy, T. P. Russell, Curving and Frustrating Flatland. *Science* 306, 76 (2004).

[104] Y. Wu, G. Cheng, K. Katsov, S. W. Sides, J. Wang, J. Tang, G. H. Fredrickson, M. Moskovits, G. D. Stucky, Composite mesostructures by nano-confinement. *Nat. Mater.* 3, 816 (2004).

[105] H. Xiang, K. Shin, T. Kim, S. Moon, T. J. McCarthy, T. P. Russell, The influence of confinement and curvature on the morphology of block copolymers. *J. Polym. Sci: Part B Polym. Phys.* 43, 3377 (2005).

[106] Y. Sun, M. Steinhart, D. Zschech, R. Adhikari, G. H. Michler, U. Gösele, Diameter-dependence of the morphology of PS-b-PMMA nanorods confined within ordered porous alumina templates. *Macromol. Rapid Commun.* 26, 369 (2005).

[107] G. J. A. Sevink, A. V. Zvelindovsky, J. G. E. M. Fraaije, H. P. Huinink, Morphology of symmetric block copolymer in a cylindrical pore. *J. Chem. Phys.* 115, 8226 (2001).

[108] W. Li, R. A. Wickham, R. A. Garbary, Phase diagram for a diblock copolymer melt under cylindrical confinement. *Macromolecules* 39, 806 (2006).

[109] B. Yu, P. Sun, T. Chen, Q. Jin, D. Ding, B. Li, A. Shi, Confinement-induced novel morphologies of block copolymers. *Phys. Rev. Lett.* 96, 138306 (2006).

[110] B. Yu, P. Sun, T. Chen, Q. Jin, D. Ding, B. Li, A. Shi, Self-assembly of diblock copolymers confined in cylindrical nanopores. *J. Chem. Phys.* 127, 114906 (2007).

[111] Q. Wang, Symmetric diblock copolymers in nanopore: Monte Carlo simulations and strong stretching theory. *J. Chem. Phys.* 126, 24903 (2007).

[112] G. J. A. Sevink, A. V. Zvelindovsky, Block copolymers confined in a nanopore: pathfinding in a curving and frustrating flatland. *J. Chem. Phys.* 128, 084901 (2008).

[113] W. Li, R. A. Wickham, Self-assembled morphologies of a diblock copolymer melt confined in a cylindrical nanopore. *Macromolecules* 39, 8492 (2006).

[114] P. Chen, H. Liang, A-C, Shi, Origin of microstructures from confined asymmetric diblock copolymers. *Macromolecules* 40, 7329 (2007).

[115] S. D. Hart, G. R. Maskaly, B. Temelkuran, P. H. Prideaux, J. D. Joannopoulos, Y. Fink, External reflection from omnidirectional dielectric mirror fibers. *Science* 296, 510 (2002).

[116] M. Ma, V. Krikorian, J. H. Yu, E. L. Thomas, G. C. Rutledge, Electrospun polymer nanofibers with internal periodic structure obtained by microphase separation of cylindrically confined block copolymers. *Nano Lett.* 6, 2969 (2006).

[117] J. H. Yu, S. V. Fridrikh, G. C. Rutledge, Production of submicrometer diameter fibers by two-fluid electrospinning. *Adv. Mater.* 16, 1562 (2004).

[118] M. Gordon, J. S. Taylor, *J. Appl. Chem.* 2, 493 (1952).

[119] Z. Sun, E. Zussman, A. L. Yarin, J. H. Wendorff, A. Greiner, Compound core-shell polymer nanofibers by co-electrospinning. *Adv. Mater.* 15, 1929 (2003).

[120] I. A. Ansari, I. W. Hamley, Templating the patterning of gold nanoparticles using a stained triblock copolymer film surface. *J. Mater. Chem.* 13, 2412 (2003).

[121] 'Polymer Handbook' (Eds J. Brandrup, E. H. Immergut and E. A. Grulke). 4th Edn, Wiley, New York, 1999, P. VII/675 (Solubility parameters); P. VI/193 (Glass transition temperatures); P. V/91 (Compressibility).

[122] Y. A. Fakhreddine, P. Zoller, The equation of state of a polydimethylsiloxane fluid. *J. Appl. Polym. Sci.* 41, 1087 (1990).

[123] E. Helfand, Z. R. Wasserman, Block copolymer theory. 4. Narrow interphase approximation. *Macromolecules* 9, 879 (1976)

[124] Z. Wang, S. A. Safran, Curvature elasticity of diblock copolymer monolayers. *J. Chem. Phys.* 94, 679 (1991).

[125] S. P. Gido, E. L. Thomas, Lamellar diblock copolymer grain boundary morphology. 2. Scherk twist boundary energy calculations. *Macromolecules* 27, 849 (1994).

[126] C. E. Williams, M. Kleman, Dislocations, grain boundaries and focal conics in smectics A. J. *De Physique, Colleque* C1-315 (1975).

[127] V. Kalra, S. Mendez, J. H. Lee, H. Nguyen, M. Marquez, Y. L. Joo, Confined assembly in coaxially electrospun block copolymer fibers. *Adv. Mater.* 18, 3299 (2006).

[128] A. K. Khandpur, S. Forster, F. S. Bates, I. W. Hamley, A. J. Ryan, W. Bras, K.

Almdal, K. Mortensen, Polyisoprene-polystyrene diblock copolymer phase diagram near the order-disorder transition. *Macromolecules* 28, 8796 (1995).

[129] J. Y. Cheng, A. M. Mayes, C. A. Ross, Nanostructure engineering by templated self-assembly of block copolymers. *Nature Mater.* 3, 823 (2004).

[130] H. Yokoyama, T. E. Mates, E. J. Kramer, Structure of asymmetric diblock copolymers in thin films. *Macromolecules* 33, 1888 (2000).

[131] C. C. Honeker, E. L. Thomas, Perpendicular deformation of a near-single-crystal triblock copolymer with a cylindrical morphology. 2. TEM. *Macromolecules* 33, 9407 (2000).

[132] E. L. Thomas, D. M. Anderson, C. S. Henkee, D. Hoffman, Periodic area-minimizing surfaces in block copolymers. *Nature* 334, 598 (1988).

[133] V. Z.-H. Chan, J. Hoffman, V. Y. Lee, H. Iatrou, A. Avgeropoulos, N. Hadjichristidis, R. D. Miller, E. L. Thomas, Ordered Bicontinuous Nanoporous and Nanorelief Ceramic Films from Self Assembling Polymer Precursors. *Science* 286, 1716 (1999).

[134] D. A. Hajduk, H. Takenouchi, M. A. Hillmyer, F. S. Bates, M. E. Vigild, K. Almdal, Stability of the perforated layer (PL) phase in diblock copolymer melts. *Macromolecules* 30, 3788 (1997).

[135] M. W. Matsen, Cylinder→Gyroid Epitaxial Transitions in Complex Polymeric Liquids. *Phys. Rev. Lett.* 80, 4470 (1998).

[136] S. Zhu, Y. Liu, M. H. Rafailovich, J. Sokolov, D. Gersappe, D. A. Winesett, H. Ade, Confinement-induced miscibility in polymer blends. *Nature* 400, 49 (1999).

[137] A. A. Argun, J. N. Ashcraft, P. T. Hammond, Highly conductive, methanol resistant polyelectrlyte multilayers. *Adv. Mater.* 20, 1539 (2008).

[138] L. Feng, S. Li, Y. Li, H. Li, L. Zhang, J. Zhai, Y. Song, B. Liu, L. Jiang and D. Zhu, Super-hydrophobic surfaces: from natual to artificial. *Adv. Mater.* 14, 1857 (2002).

[139] Z. Gu, H. Wei, R. Zhang, G. Han, C. Pan, H. Zhang, X. Tian and Z. Chen, Artificial silver ragwort surface. *Appl. Phys. Lett.* 86, 201915 (2005).

[140] Y. Zhu, J. Zhang, J. Zhai, Y. Zheng, L. Feng and L. Jiang, Multifunctional carbon nanofibers with conductive, magnetic and superhydrophobic properties. *ChemPhysChem* 7, 336 (2006).

[141] M. Ma, R. M. Hill, G. C. Rutledge, A review of recent results on superhydrophobic materials based on micro- and nanofibers. *Journal of Adhesion Science and Technology,* in press.

[142] D. Li, Y. Wang and Y. Xia, Electrospinning of polymeric and ceramic nanofibers as uniaxially aligned arrays. *Nano Lett.* 3, 1167 (2003).

[143] Q. Cong, G. Chen, Y. Fang and L. Ren, Super-hydrophobic characteristics of butterfly wing surface. *J. Bionics Eng.* 1, 249 (2004).

[144] M. Srinivasarao, Nano-optics in the biological world: beetles, butterflies, birds, and moths. *Chem. Rev.* 99, 1935 (1999).

[145] Zh-Z. Gu, H. Uetsuka, K. Takahashi, R. Nakajima, H. Onishi, A. Fujishima and O. Sata, Structural color and lotus effect. *Angew. Chem. Int. Ed.* 42, 894 (2003).

[146] C. F. Bohren and D. R. Huffman, *Absorption and Scattering of Light by Small Particles,* Ch. 3, Ch.4 and Ch. 8. Wiley-VCH (2004).

[147] J. S. Yang, T. M. Swager, Fluorescent porous polymer films as TNT chemosensors: electronic and structual effects. *J. Am. Chem. Soc.* 1998, 120, 11864.